DOT/FAA/TC-15/49

Federal Aviation Administration
William J. Hughes Technical Center
Aviation Research Division
Atlantic City International Airport
New Jersey 08405

Wireless Sensors Activated by Structural Damage

February 2016

Final Report

U.S. Department of Transportation
Federal Aviation Administration

NOTICE

This report is available at the Federal Aviation Administration William J. Hughes Technical Center's Full-Text Technical Reports page: actlibrary.tc.faa.gov in Adobe Acrobat portable document format (PDF).

Technical Report Documentation Page

1. Report No.	2. Government Accession No.	3. Recipient's Catalog No.
DOT/FAA/TC-15/49		

4. TITLE AND SUBTITLE	5. Report Date
WIRELESS SENSORS ACTIVATED BY STRUCTURAL DAMAGE	February 2016
	6. Performing Organization Code

7. Author(s)	8. Performing Organization Report No.
Robert Kauffman	

9. Performing Organization Name and Address	10. Work Unit No. (TRAIS)
University of Dayton Research Institute 300 College Park Dr. Dayton, OH 45469-0161	
	11. Contract or Grant No. DTFACT-12-C-00009

12. Sponsoring Agency Name and Address	13. Type of Report and Period Covered
U.S. Department of Transportation Federal Aviation Administration FAA Northwest Mountain Regional Office 1601 Lind Ave., SW Renton, WA 98057	Final Report July 2012–October 2015
	14. Sponsoring Agency Code ANM-111

15. Supplementary Notes

The Federal Aviation Administration William J. Hughes Technical Center Aviation Research Division COR was Michael Walz.

16. Abstract

This report presents the research performed during a 3-year research program designed to develop, then evaluate, wireless sensors capable of detecting structural damaging impacts; composite structural damage due to impact and fatigue; and the presence of corrosive chemicals and organic fluids. The research focused on the evaluation of g-force sensors; silver epoxy adhesive and other conductive lines capable of detecting composite surface cracks, metallic wires, and silicone rubber cords altered by their chemical environment; and modified radio frequency identification (RFID) tags capable of being read through different types of composite structures and composite hybrids containing wire mesh for lightning strike protection. The ASTM's impact, ultimate strength/failure load, and fatigue tests, as well as non-ASTM impact and fatigue tests, were used to evaluate the structural damage detection potentials of conductive lines to epoxy-coated and tape-covered surfaces. The surface damage detected by the conductive lines and resulting loss of structural strength were then correlated with the internal composite specimen damage that was fully characterized by magnified cross-sections, ultrasonic C-scan amplitude, time of flight analyses, and x-ray computer-assisted tomography analyses. The final products of the research were Peel-N-Stick sensors, based on a 125 KHz RFID tag designed to identify the presence of internal composite structural damage from outside the aircraft as long as the RFID antenna is positioned on the composite skin or stringer tapered region.

17. Key Words	18. Distribution Statement
Radio frequency identification tag, Wireless sensors, Composites, Structural health monitoring, Impact damage, Fatigue, Bond failure, Corrosion, Silver epoxy adhesive, PeelN-Stick sensors, ASTM tests	This document is available to the U.S. public through the National Technical Information Service (NTIS), Springfield, Virginia 22161. This document is also available from the Federal Aviation Administration William J. Hughes Technical Center at actlibrary.tc.faa.gov.

19. Security Classif. (of this report)	20. Security Classif. (of this page)	21. No. of Pages	22. Price
Unclassified	Unclassified	121	

TABLE OF CONTENTS

LIST OF FIGURES

LIST OF TABLES

LIST OF SYMBOLS AND ACRONYMS

MΩ	Megaohms
μm	Micrometers/Microns
Ω	Ohms
BAP	Battery assisted passive
BVD	Barely visible damage
CAI	Compression-After-Impact
CAT	Computer-assisted tomography
CNF	Carbon nanofiber
CNT	Carbon nanotube
HF	High frequency
IC	Integrated circuit
Kip	Kilopound-force
KHz	Kilohertz
KM	Kilometers
Ksi	Kilopound per square inch
LF	Low frequency
msec	Millisecond
NASA	National Aeronautics and Space Administration
RFID	Radio frequency identification
SMART	Status and Motion-Activated Radiofrequency Tag
SPMS	Sensory Prognostics and Management Systems
TOF	Time of flight
UDRI	University of Dayton Research Institute
UHF	Ultrahigh frequency

EXECUTIVE SUMMARY

To optimize aircraft reliability and flight safety, scheduled inspections and maintenance procedures are performed to identify, then replace, components that are damaged/malfunctioning/worn-out prior to eventual failure. To minimize unscheduled downtime, the time intervals of the inspections and procedures are based on the design lifetimes of the selected components. The time intervals are conservative in nature to ensure they are shorter than the component lifetime under normal—and abnormal—operating conditions and range from hundreds of flight hours at the airport gate to years of service in a maintenance center. To improve aircraft reliability and flight safety while reducing unscheduled maintenance time and costs, Sensory Prognostics and Management Systems (SPMS) programs are being designed to coordinate the actions and data generated by the different levels of inspections and maintenance procedures.

To further improve both the predictive capabilities and the cost effectiveness of an aircraft SPMS program, there is a need for inexpensive, lightweight sensor systems suitable for incorporation into aircraft structures. In addition to their health monitoring capabilities, the outputs of the sensors need to be wireless and compatible with the communication protocols and interfaces used by the different levels of maintenance personnel, safety management systems, and aviation safety databases. Therefore, the University of Dayton Research Institute has completed a 36-month period-of-performance research project consisting of ten main tasks to design, construct, and then evaluate different candidate wireless sensors for incorporation into current and future aircraft structures.

The following final report presents the research performed to develop, then evaluate, the wireless sensors capable of detecting composite surface cracks and bond failures resulting from structural impacts and fatigue. This research focused on the identification and evaluation of different inks and epoxies for producing conductive lines capable of detecting composite surface cracks; g-force sensors capable of detecting structural impacts; and modified radio frequency identification (RFID) tags capable of being read through composite structures. In addition to the structural damage sensors, RFID-based sensors capable of detecting the presence of corrosive chemicals and organic fluids by incorporating metallic wires and silicone rubber cords were also developed. The results of laboratory and ASTM impact tests used to evaluate the potential of the different conductive lines to detect composite surface cracks and g-force sensors to detect structural impacts are described. The analytical tests used to correlate the composite surface cracks detected by the conductive lines with internal damage and resulting loss of structural strength are also described in detail. ASTM impact, ultimate strength/failure load and fatigue tests, and non-ASTM impact and fatigue tests were used to evaluate the structural damage detection potentials of conductive lines applied to epoxy-coated and tape-covered surfaces. The surface damage detected by the conductive lines and resulting loss of structural strength were then correlated with the internal composite specimen damage that was fully characterized by magnified cross-sections, ultrasonic C-scan amplitude, time of flight analyses, and x-ray computer-assisted tomography analyses. The final products of the research were Peel-N-Stick RFID-based sensors designed to identify the presence of internal composite structural damage from outside the aircraft as long as the RFID antenna is positioned on the composite skin or stringer tapered region.

1. INTRODUCTION

During previous University of Dayton Research Institute (UDRI) research funded by the Federal Aviation Administration (FAA) [1 and 2], passive radio frequency identification (RFID) tags were modified to produce wireless status and motion-activated radiofrequency tag (SMART) sensors to improve the performance and intelligence of aircraft electrical wire and interconnect systems. The RFID tag modifications (bypass and pad connections) required to produce a SMART sensor are shown in figure 1.

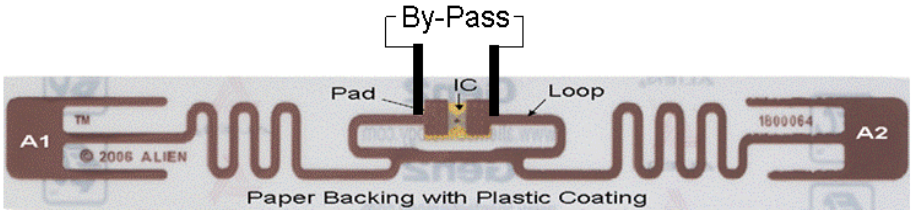

Figure 1. RFID tag modifications required to produce a generic SMART sensor

By positioning an electrical bypass parallel to the integrated circuit (IC), the IC is unable to communicate as long as the bypass remains intact. Once the bypass is broken or opened, the IC can be powered and can communicate with a proximate reader (reading distance dependent on the tag frequency, environment, presence of an on-tag battery, etc.). Consequently, the condition-based SMART sensor concept is in direct contrast to most wireless condition monitoring sensors, which require constant power, continuous monitoring, and an extensive communications system to handle the large amount of data constantly being transmitted. Regardless of the number of sensors, the communication requirements of a SMART sensor system are minimal and are suitable for use with the different levels of protocols and interfaces of an aircraft SPMS program.

Of the wide range of aircraft equipment and structures that could potentially be monitored for normal wear and tear and specific failure modes using SMART sensors with customized bypasses, structures are the focus of the research reported herein. Two basic sensors were designed for monitoring structural health: SMART Crack sensors based on conductive traces and SMART Impact sensors based on g-switches. For the SMART Crack sensors, a metal trace or conductive line applied to the surface of a nonconductive polymer was used to complete the IC bypass, as shown in figure 2.

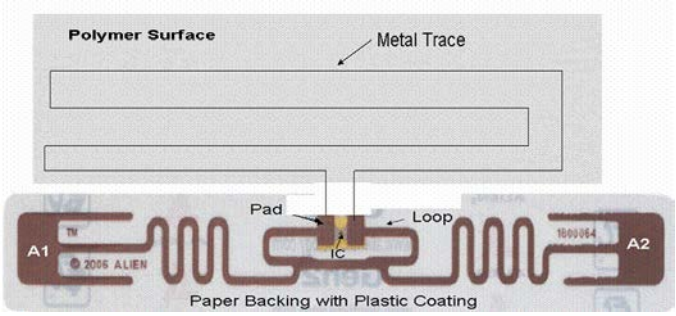

Figure 2. SMART Crack sensor illustration

As long as the metal trace/conductive line is intact, the RFID tag is unreadable. When a crack forms in the polymer surface, the crack causes a break in the trace/line and the RFID tag again becomes readable. In addition to cracks, the SMART Crack sensor can be used to detect corrosive environments by matching the composition of the metal trace with the potential corrosive agents—for example, tin trace for hydrofluoric acid evolving from wiring insulation, copper trace for runway deicers, etc.

In the case of the SMART Impact sensor, a ball/spring/ball combination was used to complete the integrated circuit (IC) bypass, as shown in figure 3.

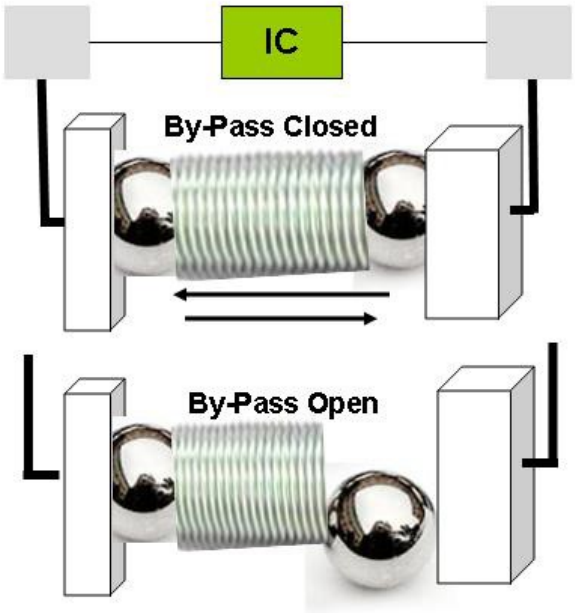

Figure 3. Ball/spring/ball combination

As long as the ball/spring/ball system remains intact, the RFID tag is unreadable. When the sensor experiences an acceleration that exceeds the stiffness constant of the spring (i.e., the spring compresses), the balls drop out of their depressions, therefore breaking the electrical circuit on which the RFID tag becomes readable. Commercial impact sensors based on the

ball/spring/ball combination shown in figure 3 are available in a wide range of g-forces, ranging from 2–100 g.

The research and initial impact testing performed to develop, then evaluate, SMART Crack and Impact sensors capable of providing the proactive maintenance and performance data needed for an aircraft SPMS program are described herein. The various topics covered during the three research projects include:

- Conductive line composition and dimensions.
- Resettable, no power shock sensors.
- Frequency of RFID tags (ultrahigh frequency [UHF] tags for long-range transmission vs. high- and low-frequency tags for short-range transmission through conductive materials).
- ASTM and non-ASTM tests to damage composite panels and determine composite test specimen strengths before and after damage tests.
- Different SMART sensor designs to detect impact, fatigue, bond failure, and chemicals.
- Analytical tests to correlate SMART sensor damage detection with internal damage.
- Peel-N-Stick SMART sensors.
- Effects of metallic mesh for lightning strikes on SMART sensor performance.
- Proper SMART sensor installation location: inside surface, joint/patch, and outside surface (under coating/paint).

2. TASK 2: CONDUCTIVE LINES

2.1 NANOINK STRIPS

Based on previous research with composite engine blade containment systems [3–5], the initial conductive traces/lines investigated for incorporation into a SMART crack sensor were based on nanoink strips formulated with different epoxies and carbon materials. In practice, the epoxy in each nanoink would be selected based on the epoxy used to produce the composite laminate surface being monitored. The effects of strip length, width, and thickness on strip resistance were determined for nanoinks containing different concentrations of carbon nanofibers (CNF), carbon nanotubes (CNTs), and chopped carbon fibers (a lower cost alternative to CNF and CNT). The goal of this study was to produce nanoink strips with resistances below 2000 ohms to achieve IC deactivation of the modified RFID tag used in the SMART Crack sensor [1 and 2].

The initial epoxy-based nanoink (9% CNF) tests were performed on the front and back surfaces of nonconductive epoxy fiberglass sheets, as shown in figure 4.

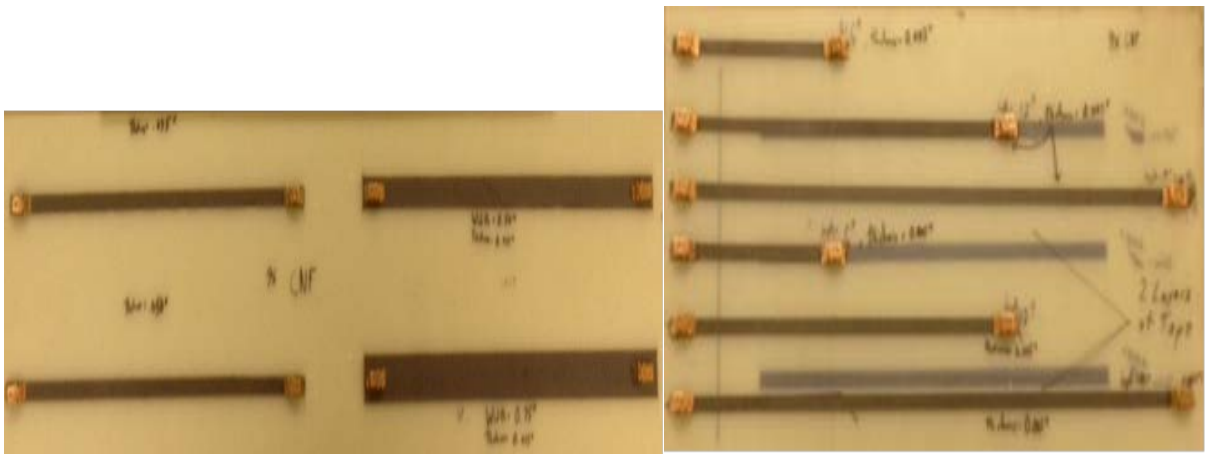

Figure 4. CNF (9%) nanoink strips produced on epoxy fiberglass sheets

The nonconductive epoxy fiberglass sheets were used for the initial tests instead of conductive composite laminates, which required an insulating layer to protect the applied nanoink strip and associated SMART sensor from the conductive fibers protruding from the laminate surface. Copper posts were incorporated into the ends of each strip to provide reproducible test points for making the resistance measurements.

The measured resistances of the 9% CNF nanoink strips (front and back strips on right sheet in figure 4), with the corresponding length, thickness, and width of each measured nanoink strip, are listed in table 1.

Table 1. Summary of 9% CNF nanoink strip data

Strip Length (in.)	Resistance (ohms)	Thickness (in.)	Width (in.)
6	8,250	0.003	0.25
12	17,000	0.003	0.25
18	25,300	0.003	0.25
6	2,800	0.005	0.25
12	6,800	0.005	0.25
18	11,200	0.005	0.25
12	4,420	0.011	0.25
12	2,580	0.015	0.25
12	1,690	0.018	0.25
12	1,100	0.015	0.50
12	710	0.015	0.75
12	1,100	0.035	0.25
12	1,010	0.050	0.25

As expected, the data show that the strip resistance increases with length and decreases with width and thickness. The resistance measurements have linear and nearly linear (which may be a power function) relationships with the selected strip dimension when they are plotted vs. length (figure 5) and width (figure 6 for 12-inch lengths), respectively.

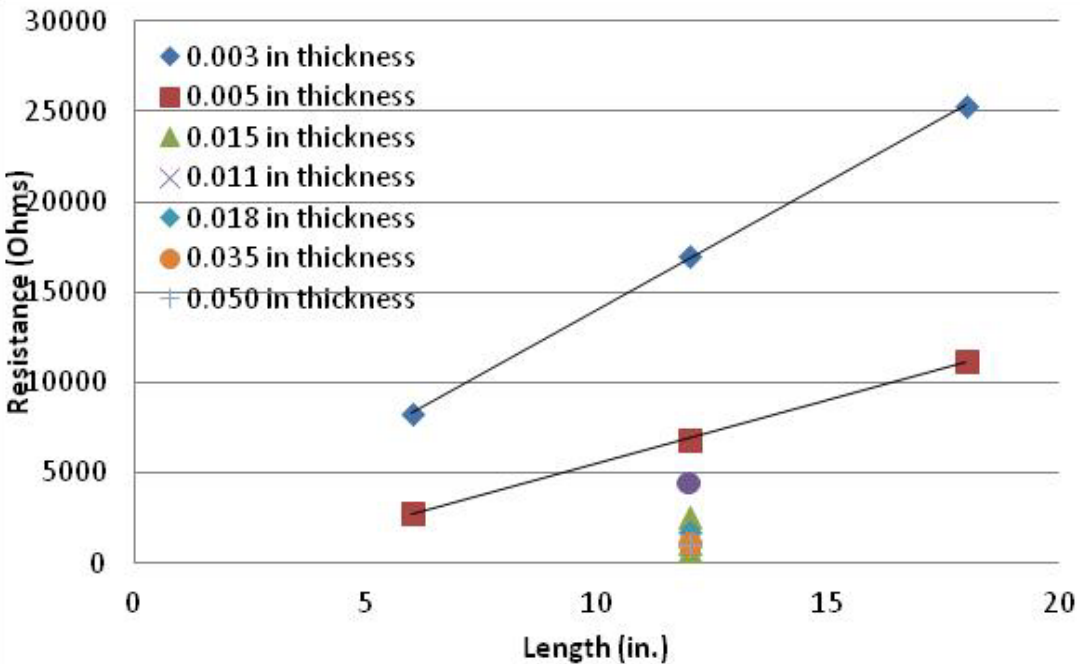

Figure 5. Plot of resistance vs. length for 9% CNF nanoink strips

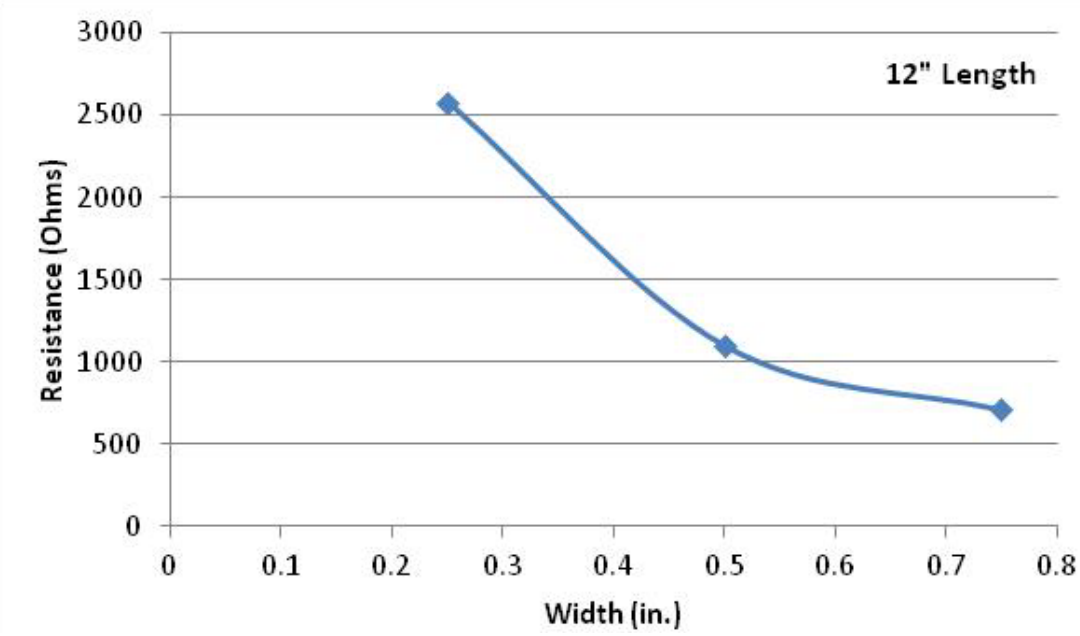

Figure 6. Plot of resistance vs. width for 9% CNF nanoink strips

However, when plotted vs. strip thickness, the resistance measurements followed a power regression relationship (i.e., at thicknesses up to 0.007″, the resistance decreases rapidly with increasing thickness; at thicknesses above 0.015″, the resistance decreases slowly with increasing thickness [figure 7 for 12″ lengths]).

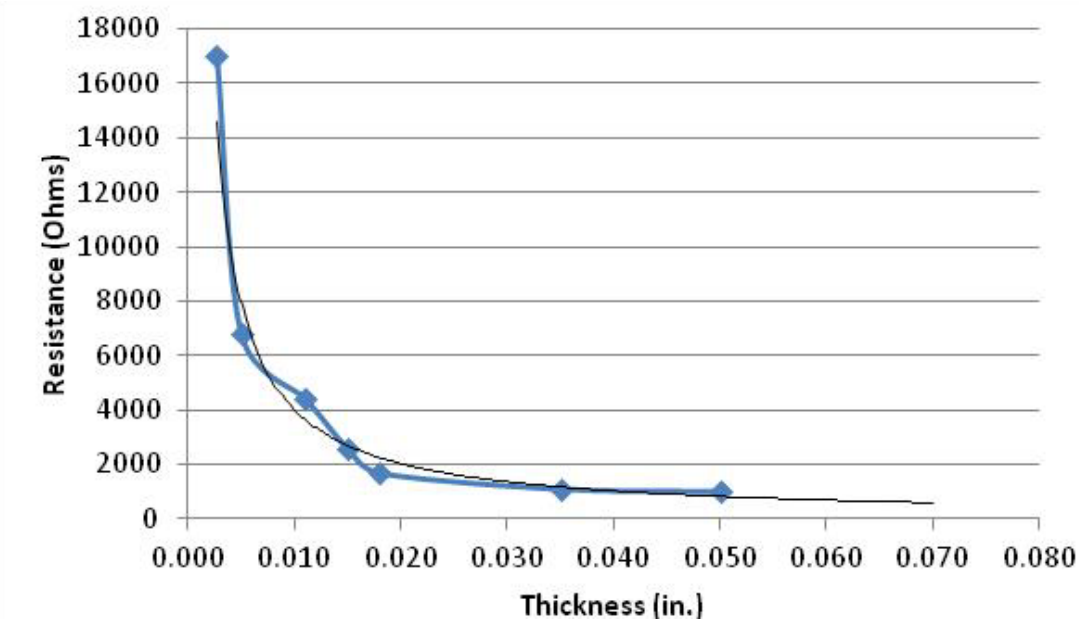

Figure 7. Plot of resistance vs. thickness for 9% CNF nanoink strips

The next epoxy-based nanoink tested contained CNT. The nanoink contained 7% CNT (by weight), which is the highest percentage of CNT that can be added to epoxy and still produce a functional nanoink. The 7% CNT nanoink was used to produce 12″ long, 0.25″ wide conductive strips with varying thicknesses, as shown in figure 8.

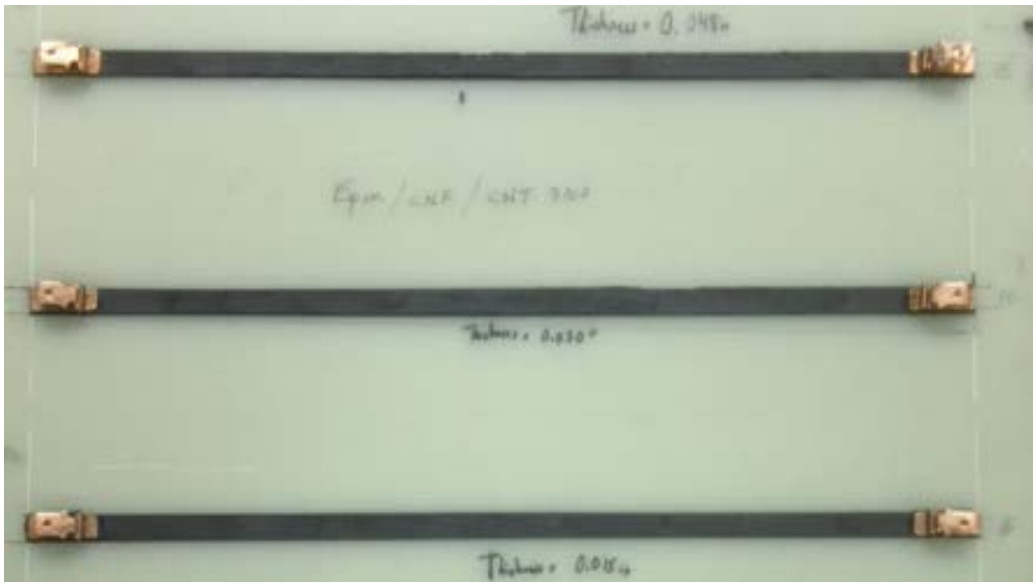

Figure 8. CNT (7%) nanoink strips produced on epoxy fiberglass sheet

As opposed to the resistance vs. thickness plot for the 9% CNF strips in figure 7, the resistance vs. thickness plot in figure 9 for the 7% CNT strips is nearly linear.

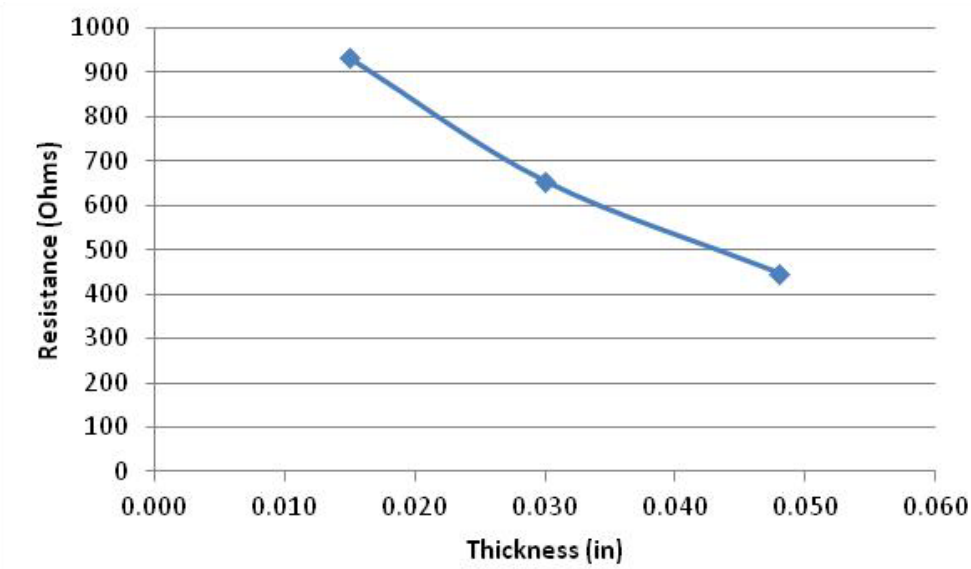

Figure 9. Resistance vs. thickness for 7% CNT nanoink strips

To compare the resistances of the nanoink strips produced with similar amounts of carbon materials, the resistances for 12″ length nanoink strips produced with 9% CNF and 7% CNT are listed in table 2.

Table 2. 7% CNT and 9% CNF nanoink strip resistances

Nanoink Composition	Resistance (ohms)	Thickness (in.)	Width (in.)
7% CNT	932	0.015	0.25
7% CNT	654	0.030	0.25
7% CNT	446	0.048	0.25
9% CNF	2580	0.015	0.25
9% CNF	1100	0.035	0.25
9% CNF	1010	0.050	0.25

The above data show that the 7% CNT strips have lower (~3 times) resistances when compared with the 9% CNF strips. The lower resistances/higher conductivities of the CNT strips compared to those of the CNF strips help explain why the relationship between thickness and resistance is linear for the CNT strips in figure 9 compared to a power regression relationship for the CNF strips in figure 7.

Because of the higher cost of the CNT nanoinks when compared to the CNF inks, a third epoxy-based nanoink was formulated with 8% chopped fibers and 7.2% CNF (by weight). The chopped fiber/CNF nanoink was used to produce 12″ long, 0.25″ wide conductive strips with varying thicknesses, as shown in figure 10.

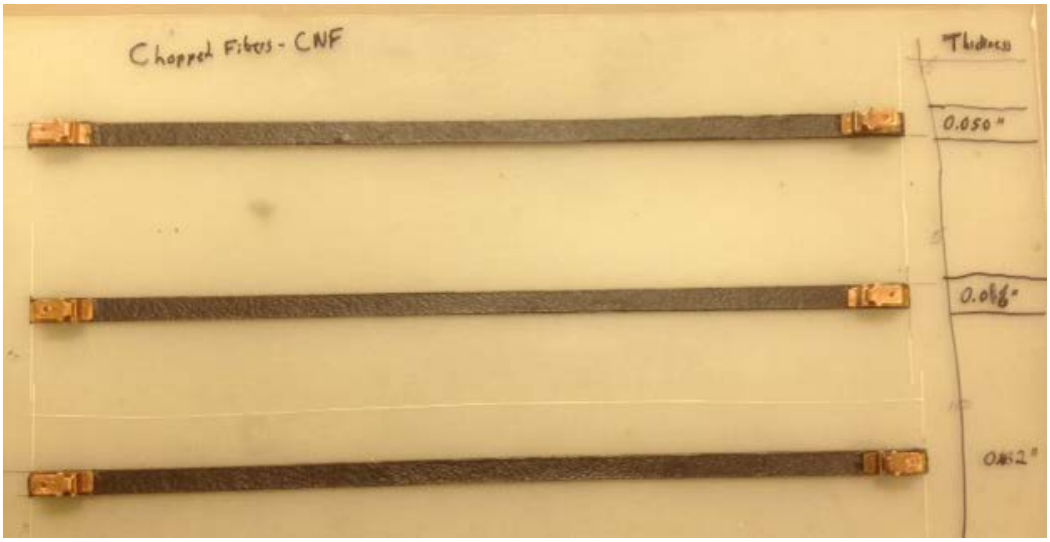

Figure 10. Chopped fiber (8%)/CNF (7.2%) nanoink strips on epoxy fiberglass sheet

As opposed to the resistance vs. thickness plot for the 9% CNF strips in figure 7, the resistance vs. thickness plot for the 8% chopped fiber/7.2% CNF strips is nearly linear in figure 11 (similar in linearity to the 7% CNT plot in figure 9).

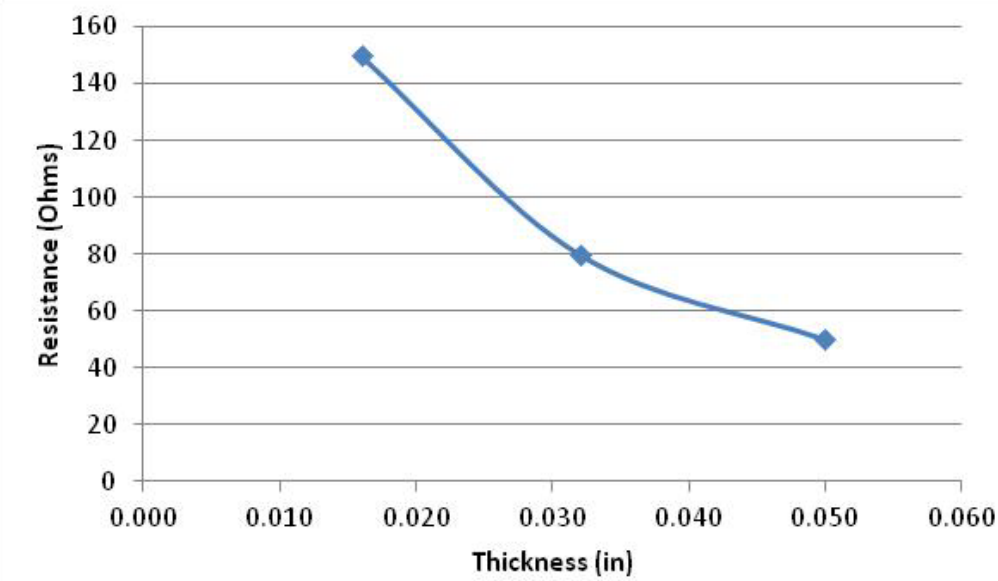

Figure 11. Resistance vs. thickness for 8% chopped fiber/7% CNF nanoink strips

The resistances of the nanoink strips produced with/without chopped fibers are listed in table 3, which shows that adding chopped fibers decreased the strip resistances 15–20 times.

Table 3. CNF, CNT, and chopped-fiber combination nanoink strip resistances

Nanoink Composition	Resistance (ohms)	Thickness (in.)	Width (in.)
9% CNF	2580	0.015	0.25
9% CNF	1100	0.035	0.25
9% CNF	1010	0.050	0.25
8.15% CNF + 5% CNT	206	0.015	0.25
8.15% CNF + 5% CNT	127	0.030	0.25
8.15% CNF + 5% CNT	97	0.048	0.25
7.2% CNF + 8% Chopped Fiber	150	0.016	0.25
7.2% CNF + 8% Chopped Fiber	80	0.032	0.25
7.2% CNF + 8% Chopped Fiber	50	0.050	0.25

For comparison, an epoxy-based nanoink test was formulated with CNF and the much higher-priced CNT. The 8.15 CNF/5% CNT (by weight) nanoink was used to produce 12″ long, 0.25″ wide conductive strips with varying thicknesses, as in previous tests. Similar to the chopped fiber addition, the resistance vs. thickness plot for the CNT containing strips was nearly linear (higher strip conductivity helps explain the linear relationship with thickness), but the strip resistance reductions achieved with the CNT additions were approximately two times lower than those with the inexpensive chopped fibers.

2.2 ALTERNATIVE CONDUCTIVE INKS AND ADHESIVES

In addition to the nanoink strips, conductive lines were applied/drawn with alternative inks and adhesives for evaluation. Conductive lines were applied to the epoxy fiberglass sheet in figure 8 using laboratory-mixed compositions (50% graphite flakes in room temperature setting epoxy and cyanoacrylate glue [super glue]) and commercial products (silver epoxy [MG Chemicals], Parmod silver ink [Parelec], Circuit Writer silver ink pen [CAIG Laboratories], and conductive wire glue [carbon/silicate-based ink from Radio Shack]). Though the Parmod silver ink was used successfully to draw conductive lines, Parelec has gone out of business (purchased on [1]). In addition, the silver epoxy requires heating (60° C) to reach its minimum resistance, thereby restricting its use on existing aircraft surfaces. Therefore, an additional commercial silver ink and a silver epoxy ink (room temperature cure), manufactured by Creative Materials, were identified. Also, a fast drying version of the Circuit Writer silver ink pen was purchased directly from CAIG Laboratories.

2.3 INITIAL EVALUATIONS OF CONDUCTIVE STRIPS AND LINES

To initially evaluate the potential of the nanoink strips and alternative conductive lines to detect surface cracks, the strips and lines were applied to an epoxy fiberglass panel that was flexed until the panel and strips/lines became damaged. Though not a realistic failure mechanism of composite panels, the panel flexing was used as a screening tool for selecting the conductive strips and lines with the most potential for use with the SMART Crack sensor.

The various laboratory and commercial conductive inks/adhesives were applied in short lines to the epoxy fiberglass panel with the 7% CNT nanoink strips (figure 8). The resistances of the laboratory and commercial conductive lines ranged from 200Ω for the 50% graphite flakes in epoxy down to 2Ω for the thin (width less than 0.05″) conductive lines containing silver. For comparison, the resistances of the 12″ nanoink strips (0.25″ width) ranged from 400–900Ω (0.01″–0.05″ thickness, respectively).

To control the flex point of the epoxy fiberglass panel, the back side of the epoxy fiberglass was cut widthwise prior to the application of the laboratory and commercial conductive products. The cut panel was then repeatedly flexed by hand, causing the panel to first craze and then break. Because the flexing also caused the copper connectors to separate from the nanoink strips, the resistance measurements were made using needle probes in direct contact with the nanoink line surfaces. The epoxy fiberglass panel (cut in back) with the 7% CNT nanoink strips (see figure 12(a)) and the panel after application of the laboratory and commercial conductive lines then flexed multiple times to produce crazing, then cracking (see figure 12(b)).

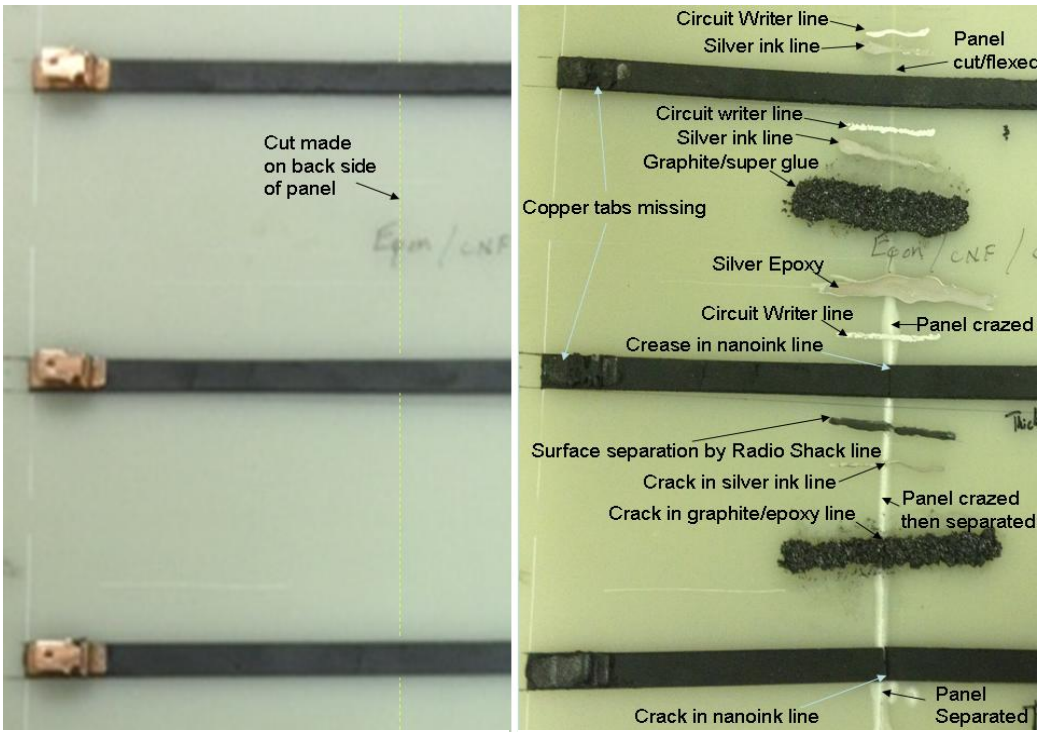

(a) (b)

Figure 12. CNT (7%) nanoink strips and alternative conductive lines on epoxy fiberglass sheet before (a) and after flexing (b)

During the initial flexing, the resistances of the nanoink strips decreased as the lines were compressed (with the panel bent upward), then increased as the lines were stretched (with the panel bent downward). When the flexing was stopped, the resistances of the strips returned to their initial resistances and no visible damage was observed in the surfaces of the panel or strips. The angle at which the panel was flexed was continuously increased until visible crazing of the panel surface (the middle of the right panel) was observed along the cut line. Even though the nanoink strips creased/cracked directly above the cut line when crazing was observed, the resistances of the re-straightened lines increased only slightly (<10%). After extensive flexing, the lowest nanoink strip in figure 12 broke as the panel beneath it separated. However, when the panel was re-straightened, the resistance of the separated line decreased from >6MΩ (the upper limit of the voltmeter) to below 2KΩ as the separated ends of the line remade contact.

Except for the conductive wire glue (carbon in aqueous sodium silicate solution), all the alternative conductive lines adhered well to the epoxy panel surface during the flexing process. Regardless of the amount of flexing, the resistances of the alternative lines remained unchanged in the panel areas away from the cut line. In contrast to the nanoink strips, the alternative lines became nonconductive (>6MΩ) for the cut panel areas that exhibited crazing and separation, regardless of the final panel position (flexed or straightened).

Next, a flexible scrap piece of composite laminate (1-mm thick x 4-cm wide) was used to evaluate the surface adherence and crack sensitivity of the nanoink strips and commercial silver inks/adhesives. The strips and lines were strongly adherent to the composite surface. However,

resistance measurements made from one line to an adjacent line/strip were below 10KΩ (should be >6MΩ if isolated), indicating that fibers protruding from the composite surface were incorporated by the lines providing additional conductive pathways. If a crack occurred in a conductive strip or line, the measured resistance would decrease only slightly because of the alternate pathways. To isolate the nanoink strip and silver conductive lines from the conductive fibers protruding from the composite surface, a thin layer of epoxy was applied to the surface of the epoxy laminate prior to the application of the strip and lines shown in figure 13.

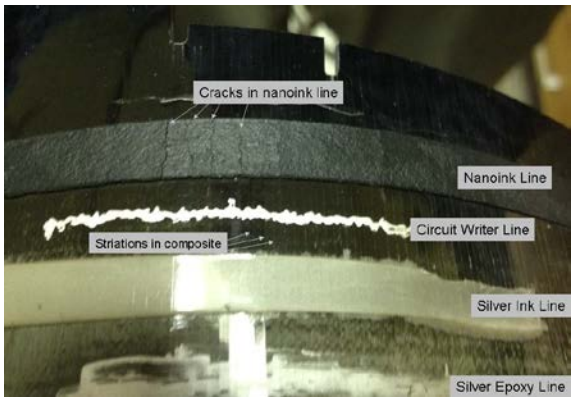

Figure 13. CNF/chopped fiber nanoink strips and silver conductive lines on epoxy-coated composite panel (flexing downward)

For this study, a 7.2% CNF + 8% chopped fiber nanoink (lowest resistance and cost nanoink) and several commercial silver adhesives/inks were used to apply conductive strips and lines to the epoxy-coated composite laminate. The laminate was notched twice in an attempt to focus the stress (similar to that shown in figure 12) as the composite panel was flexed back and forth by hand. Because of the flexibility of the composite laminate, the laminate formed an arc that could be pressed to form a U-shape. As the curve of the laminate was increased, cracking sounds (composite matrix of laminate cracking) were heard and the composite laminate had horizontal striations the entire length of the bent laminate (see figure 13). Visible cracks/striations also formed in the conductive nanoink strip and silver ink lines that were aligned with the striations in the laminate surface. Even though the nanoink strip contained visible cracks, its resistance remained below 2KΩ during the entire bending/straightening process. In contrast to the nanoink strip, the resistances of the different silver-containing lines increased rapidly during the bending process and became nonconductive (>6MΩ laminate bent or straightened), further indicating their sensitivity to surface cracks.

The bypass resistances of the deactivated RFID tags must increase to more than 5KΩ for the RFID tags to reliably activate/become readable [1]. Consequently, if the nanoink strips in figures 12 or 13 were used in a SMART Crack sensor, the sensor would not indicate that surface cracks/separation had occurred in the flexed/broken panel. To be useful for surface crack detection applications, the nanoink strips would have to be connected to a different type of passive RFID tag that outputs resistance measurements whenever powered by a proximate reader (recently developed by Phase IV Engineering).

2.4 SUMMARY

Because of their commercial availability, strong surface adherence, and low resistance, the silver ink (Creative Materials, which requires 90°C for 30 minutes), room temperature silver epoxy (Creative Materials), and Circuit Writer inks (CAIG Laboratories) were selected for further evaluation in the SMART Crack sensor.

3. TASK 3: RFID TAGS

3.1 INTRODUCTION

There are generally two types of RFID tags: active RFID tags, which contain a battery and can transmit signals continuously without exterior prompting, and passive RFID tags, which have no battery and require an external source (an interrogator/reader) to activate the tag and read the stored information. The main advantage of the active RFID tags compared to passive tags is their longer read range. However, the requirement of a battery (printed batteries, energy-scavenging systems, etc.) with a finite lifetime increases the weight, cost, and complexity of the tag modified for use in the SMART sensors. Consequently, passive RFID tags were the primary focus for developing SMART sensors. Several types of passive RFID tags suitable for development into a SMART sensor are commercially available. As summarized in table 4, there are three main frequency ranges used by commercial RFID tags.

Table 4. Comparison of different RFID tag technologies

RFID Tag	Frequency	Range	Antenna	Reprogrammable
Low Frequency (LF)	125–134 KHz	<1 foot	Coil	Varies
High Frequency (HF)	13.56 MHz	<1 foot	Trace	Yes
Ultrahigh Frequency (UHF)	850–950 MHz	20+ feet	Trace	Yes

Because conversations with FAA personnel indicated that the SMART sensors are to be read through composite structures (UHF tags cannot be read through composite laminates), only the modified HF (13.56 MHz) RFID tags produced during the previous FAA grant [1] and commercial low frequency (LF) (125 and 134 KHz) RFID tags shown in figure 14 were evaluated with the conductive nanoink strips and silver lines.

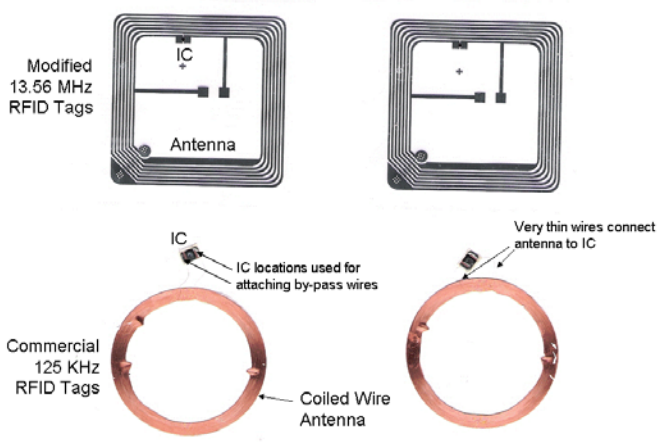

Figure 14. Modified HF and commercial LF RFID tags

To determine the resistance thresholds required to deactivate/activate the modified HF and commercial LF RFID tags (as shown in figure 14) for use in SMART Crack sensors, the modified HF RFID tags were connected to the different nanoink strips on the epoxy fiberglass panels (see figures 4, 8, and 10). To reliably connect the HF RFID tag to the copper pads of the nanoink strips, 22-gauge wires were attached with silver epoxy to the IC bypass pads and small alligator clips were added to the opposite ends of the wires, as shown in figure 15.

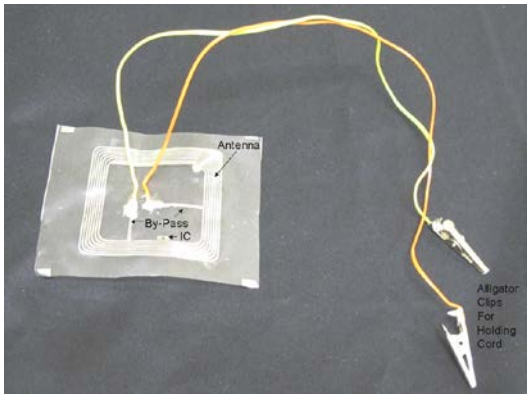

Figure 15. Modified HF RFID tag with wires attached to the IC bypass

3.2 MODIFIED HIGH FREQUENCY RFID TAG EVALUATION

The initial RFID tag/nanoink strip tests were performed with the modified HF tag and a handheld reader to determine if the resistances of the nanoink strips were suitable for use in a SMART Crack sensor. If the reader detected the tag, the strip resistance was too high and the IC bypass was acting as a broken circuit. If the reader could not detect the tag, then the resistance of the nanoink strip was suitable for use in a SMART Crack sensor. The reader responses in table 5 are listed in order of increasing nanoink strip resistance.

Table 5. 13.56 MHz reader responses for modified HF RFID tag

Composite type	Thickness inch	Resistance ohms	Reader on tag < 0.1 inch	Reader on plastic slab 0.5 inch	Reader on plastic slab +composite sheets +paper stack – 1 inch
Chopped CNF fibers	0.05	48	No read	No read	No read
Chopped CNF fibers	0.032	82	No read	No read	No read
EPON/CNF/CNT	0.05	94	No read	No read	No read
EPON/CNF/CNT	0.03	124	No read	No read	No read
Chopped CNF fibers	0.016	158	Read	No read	No read
EPON/CNF/CNT	0.015	201	No read	No read	No read
CNF/CNT	0.048	443	Read	Read	No read
CNF/CNT	0.03	649	Read	Read	No read
9% CNF	0.015	650	Read	Read	No read
9% CNF	0.05	890	Read	Read	No read
CNF/CNT	0.015	940	Read	Read	No read
9% CNF	0.015	1000	Read	Read	No read
9% CNF	0.035	1000	Read	Read	No read
9% CNF	0.003	1464	Read	Read	No read
9% CNF	0.003	2200	Read	Read	No read/Read
9% CNF	0.005	2490	Read	Read	No read/Read
9% CNF	0.005	5870	Read	Read	Read
9% CNF	0.003	7950	Read	Read	Read
9% CNF	0.005	9660	Read	Read	Read

When the reader was laid directly on the HF tag, the reader detected (i.e., read) the tag as long as the resistance of the nanoink strip was above 400Ω (strips above 400Ω were acting like an open circuit—that is, the RFID was readable, even though the IC bypass circuit was electrically closed by the nanoink strip). These results were interpreted as meaning that the IC was receiving enough power to transmit over the very short distance (less than 0.1″) between the reader and RFID tag. Placing a 0.5″ thick sheet of polyethylene between the reader and RFID tag had little effect on the readability of the tag (i.e., the tag was still able to transmit over 0.6″).

However, increasing the distance between the reader and modified HF RFID tag to 1″ by adding sheets of conductive composite laminates (ACP composites, CL2-37, Uni CF, 0.014″ thickness) and a stack of printer paper to the polyethylene sheet allowed nanoink strips with resistances up to 1,500Ω to function as a SMART Crack sensor—that is, nanoink strip intact: (<1500Ω) sensor unreadable, strip broken (>6000Ω): SMART sensor readable. Because the readability of the HF RFID was primarily dependent on the resistance of the nanoink strip, the results in table 5 indicate that resistance, not nanoink composition, controls the performance of the HF RFID tag.

3.3 LF RFID TAG EVALUATION

Next, wires/alligator clips (similar to those in figure 15) were attached to the IC solder posts of a commercial LF 125 KHz RFID tag and the copper pads of the nanoink strips were placed on the epoxy fiberglass panels. A handheld reader was used to determine the readability of the modified LF tag attached to the different nanoink strips at varying distances. The reader responses in table 6 are listed in order of increasing nanoink strip resistance.

Table 6. 125 KHz reader responses for modified LF RFID tag

Composite type	Thickness inch	Resistance ohms	Reader on plastic slab 0.5 inch	Reader on plastic slab +composite stack 0.75 inch	Reader on plastic slab + composite stack + paper stack 1 inch	Reader on plastic slab 0.5 in*
Chopped CNF fibers	0.05	48	No read	No read	No read	No read
Chopped CNF fibers	0.032	82	No read	No read	No read	No read
EPON/CNF/CNT	0.05	94	No read	No read	No read	No read
EPON/CNF/CNT	0.03	124	No read	No read	No read	No read
Chopped CNF fibers	0.016	158	No read	No read	No read	No read
EPON/CNF/CNT	0.015	201	No read	No read	No read	No read
CNF/CNT	0.048	443	No read	No read	No read	Read
CNF/CNT	0.03	649	No read	No read	No read	Read
9% CNF	0.015	650	No read	No read	No read	Read
9% CNF	0.05	890	No read	No read	No read	Read
CNF/CNT	0.015	940	No read	No read	No read	Read
9% CNF	0.015	1000	No read	No read	No read	Read
9% CNF	0.035	1000	No read	No read	No read	Read
9% CNF	0.003	1464	Read	Read	No read	Read
9% CNF	0.003	2200	Read	Read	No read	Read
9% CNF	0.005	2490	Read	Read	No read	Read
9% CNF	0.005	5870	Read	Read	No read/Read	Read
9% CNF	0.003	7950	Read	Read	No read/Read	Read
9% CNF	0.005	9660	Read	Read	No read/Read	Read

* RFID coil in key fob so add 0.25″ to get actual distance.

The first tests with the modified LF tag were performed by placing the 0.5″ thick sheet of polyethylene between the reader and the RFID tag. The data indicate that the nanoink strips with resistances up to 1000Ω were acting like a closed circuit (i.e., the RFID tag was not readable and acted closed below 400Ω). Increasing the distance between the reader and the modified LF RFID tag to 0.75″—by adding sheets of conductive composite laminates (ACP composites, CL2-37, Uni CF, 0.014″ thickness) to the polyethylene sheet—had little effect on the readability of the LF tag. However, increasing the distance between the reader and tag to 1″ with nonconductive printer paper allowed nanoink strips with resistances up to 5000Ω (HF tag acted open at ~2000Ω) to reliably function as a SMART Crack sensor (i.e., nanoink strip intact: SMART

sensor unreadable, nanoink strip broken: SMART sensor readable). The results between 5870Ω and 9660Ω were affected by the position of the reader with reference to the coil of the RFID tag: Reader directly centered above the coil—tag readable. Reader slightly off center—tag unreadable. The results in table 6 indicate that resistance, not nanoink composition, controls the performance of the HF RFID tag.

For both the HF (13.56 MHz) and LF (125 KHz) tags, readability was similar whether the reader was placed directly above the tag or on the opposite side of the epoxy fiberglass sheet/nanoink strip (reading through sheet/conductive nanoink strip).

However, when the modified, unconnected HF tag was epoxied directly to a composite panel surface, the tag could not be read with the reader held directly above the tag or on the opposite side of the composite panel (reading through the panel). It is believed that the high conductivity of the inner matrix of the panel (carbon cloth and nanofibers) was reflecting/absorbing the 13.56 MHz waves of the reader so that the IC of the tag was not powered and the tag was not "readable." If the13.56 MHz tag was separated from the composite surface by a nonconductive film, the tag's read range was unaffected by the composite with the reader held above the tag. However, if the13.56 MHz tag was held under the composite panel, it was not read until a portion of the antenna extended past the edge of the composite and was visible to the reader. Consequently, the 13.56 RFID tag will be useful only for SMART Crack sensor applications in which the tag is accessible (e.g., on back of access panel, located along walkways, etc.).

In contrast to the 13.56 RFID tag, the readability of the 125 KHz tags is not affected by the composite panel. The 125 KHz tags adhered to composite surfaces ranging in thickness from 1–5 mm were readable when the reader was held directly above the tag or on the opposite side of the composite panel (simulating the reading tag through the side of the plane).

In addition to the 125 KHz tags, another type of LF RFID tag that operates at 134 KHz and is ruggedized for use in animal tracking tags was investigated for use in the SMART Crack sensor. The 134 KHz tag has the advantages of a smaller diameter coil antenna and an IC potted onto the surface of the coil for improved ruggedness when compared to the 125 KHz RFID tag, as shown in figure 16.

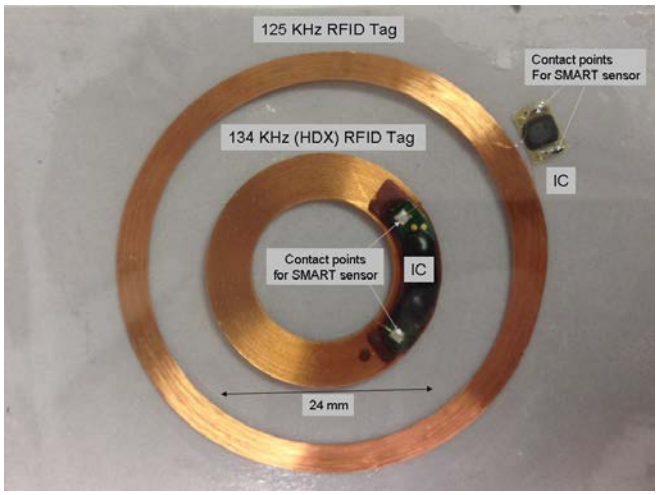

Figure 16. 125 and 134 KHz RFID tags

There are two types of 134 KHz RFID tags: full duplex (FDX) and half duplex (the former of which is shown in figure 16 and patented by Texas Instruments). The FDX tag is similar in design and size to the 125 KHz tag in figure 16 and does not have the size/ruggedized design advantages of the HDX tag. An FDX 134 KHz tag was epoxied to the surface of a 5-mm thick composite panel and was read with the reader placed directly above the tag or on the opposite side of the composite panel. In contrast to the FDX tag, HDX tags (reader made by Texas Instruments and designed specifically for the HDX formatted tags) adhered directly to or resting on a composite surface could not be read with the reader placed above the tag or on the opposite side of the panel.

3.4 SUMMARY

Based on these preliminary results, the SMART Crack sensor for composites will be based on either a 125 KHz or FDX 134 KHz RFID tag. The IC of the selected RFID tag will be connected to the silver adhesive/ink lines on the composite surface either directly (line drawn onto IC posts) or indirectly (line drawn onto thin wires soldered to the IC posts), based on the design/performance requirements. The ruggedness of the IC design, read range through composite panels, antenna coil diameter/thickness, and other features will be the deciding factors in selecting the exact tag design for each sensor application.

In addition to the commercial 125 KHZ or FDX 134 KHz tags, battery assisted passive (BAP) RFID tags that output resistance measurements whenever powered by a proximate reader (developed by Phase IV Engineering) are available for incorporation in the wireless sensors for surface crack detection. The BAP tags would be combined with the conductive nanoink strips to detect the temporary (strain) and permanent (cracks) resistance changes of the conductive strips during flexing (see figure 13) or other high-load applications. Each battery provides the BAP RFID tags with resistance logging capability for up to 5 years.

4. TASK 4: DEVELOPMENT OF SMART IMPACT SENSORS

4.1 INTRODUCTION

The initial research for this project focused on the development of direct (incorporates g-force sensor) and indirect (detects impact-induced surface cracks) SMART Impact sensors. Impact tests were performed on 0.15″ thick rigid aerospace composite (eight plies of AGP370-5HS with 8552 epoxy resin) panels. Laboratory impact tests simulating an aircraft structure impacted by a forklift, a tail strike, and other forces were performed on the panels to evaluate the capabilities of the SMART Impact sensors. The impact tests were performed with a projectile with a flat end (simulate fork lift) driven at a known speed or dropped from a known height. The impacts were designed to cause internal damage (delaminations) without causing visible damage on the impacted surface of the test panel (i.e., less than barely visible damage [BVD], which is defined as damage that is visible from 5 feet away in ambient light without special magnification tools). Impacts to composite aircraft structures that cause BVD or greater damage to the exterior impacted surface do not require wireless sensors for detection by maintenance personnel.

After each impact testing period, traditional ultrasonic C-scans (amplitude and time of flight [TOF]) were then performed to correlate the conductive line resistance changes and visible surface cracks with the degree of internal damage of the composite laminate. Additional analytical tests using high magnification photographs of cross-sectioned panels and 3-D x-ray computer-assisted tomography (CAT) images were used to further quantitate the internal damage in one of the panels.

4.2 LINEAR MOTOR IMPACT TEST: VERIFICATION OF SHOCK WAVE

The first impact test used a linear motor to drive a 0.75″ wide, 133.6 gram projectile into the surface of a rigid 6″ x 4″ composite panel held in place by two aluminum bars bolted to an aluminum platform. The composite panel was placed above the 5″ x 3″ cut-out of the aluminum platform so any damage from the impact would be centered in the panel. The linear motor input/projectile position output was controlled/recorded by a laptop computer. The linear motor impact test with the projectile pulled back from the composite surface is shown in figure 17.

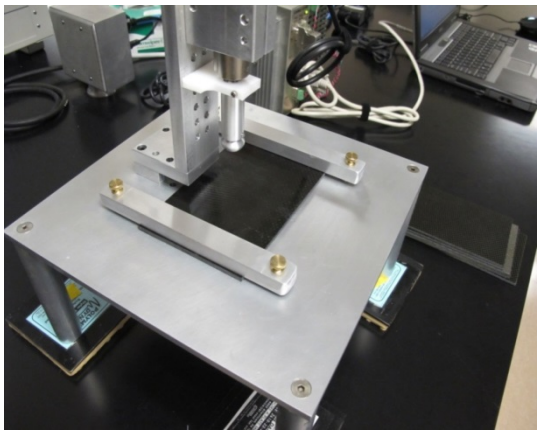

Figure 17. Linear motor impact test with composite panel in place

The g-force of the shock wave traveling through the composite panel created by each impact was partially quantified by attaching commercial shipping sensors (manufactured by IOG), with double-stick tape, to the composite panel side opposite the impact. The shipping sensors are based on two sets of steel ball/spring/ball combinations that activate at a preset g-force (g-force required to compress the springs, allowing the balls to drop). The shipping sensor (clear, protective cover removed) shown in figure 18 is activated by a preset g-force along all three axes.

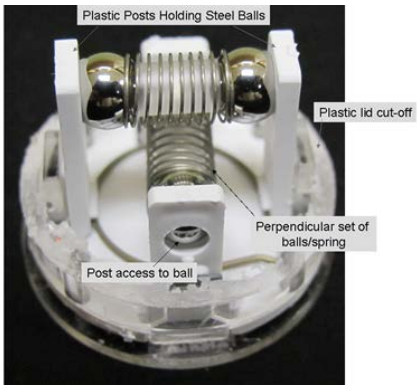

Figure 18. One-time use shipping sensor based on spring/ball concept

Prior to the first impact by the projectile, a 20 g shipping impact sensor (see figure 17) was adhered to the underside of the composite panel using industrial grade double-sided acrylic tape (3M 9500PC applied to the base of the sensor) and the impact test was performed twice. Even though no impact damage was visible (less than BVD), the 20 g impact sensor was activated (both ball/spring/ball systems fell apart). When the test was repeated with a 100 g shipping impact sensor adhered to the underside of the composite, the sensor was again activated by the impact test. Because the composite is rigid and supported on all four sides by the platform minimizing its movement, the activation of the impact sensor was attributed to the shock wave of the impact traveling through the composite panel.

To determine the g experienced by the composite surface during the impact event, the position of the projectile (millimeter [mm] from starting position) was plotted vs. time (milliseconds [msec]), as shown in figure 19.

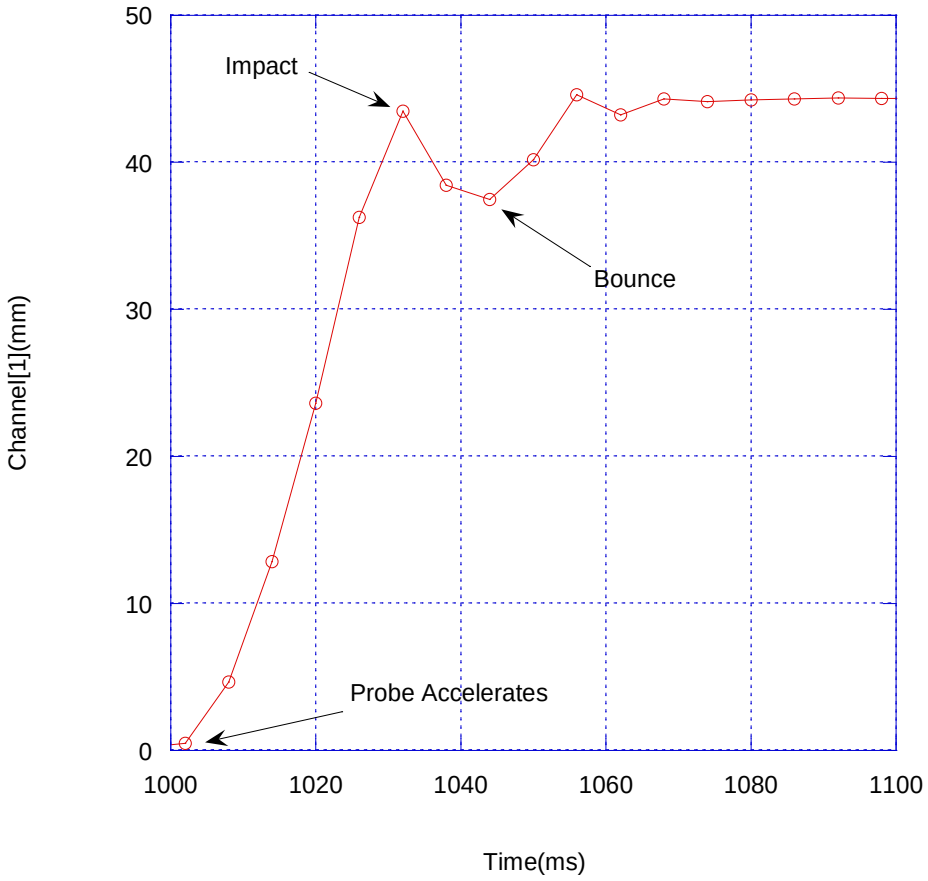

Figure 19. Plot of projectile position (mm) vs. time (msec) for projectile during linear motor impact test

The projectile position plot shows that the projectile changes direction (bounces back) within milliseconds of impacting the composite surface. Using the position plot vs. time, the velocity (mm/msec) of the projectile was calculated and then plotted vs. time, as shown in figure 20, with the determination that the speed at impact was ~2.1 mm/msec.

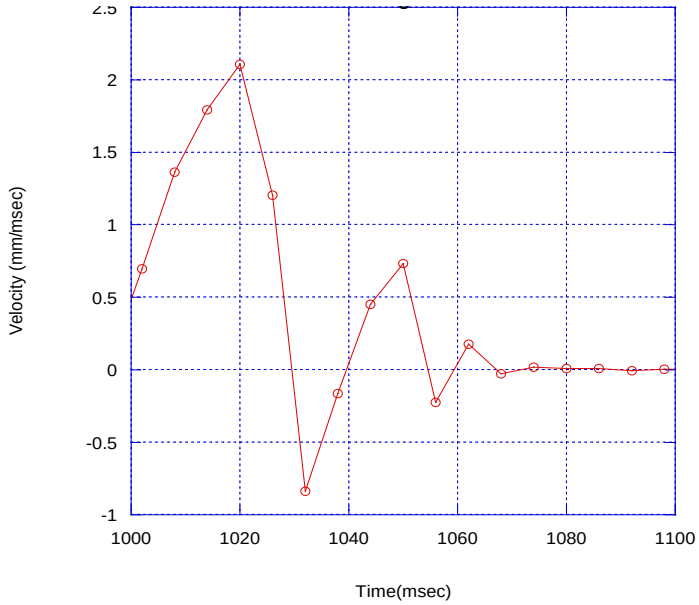

Figure 20. Plot of projectile speed (mm/msec) vs. time (msec) for projectile during linear motor impact test

The speed of 2 mm/msec (2 m/sec) translates to 7.2 kilometers (KM) per hour (hr) (4.5 miles [mi] per hour), similar to the speed of a forklift/tow motor operating around an aircraft. The velocity plot also shows that the deceleration of the projectile occurs in 1–5 msec, so the deceleration is greater than 2000–400 m/sec^2, which translates to 200–40 g (acceleration by gravity: 9.8 m/sec^2), verifying the shock wave was of a magnitude to activate the 100 g impact sensor.

4.3 DROPPED-WEIGHT IMPACT TEST: WIRED G-SENSOR

As opposed to the one-time-use shipping impact sensor in figure 17, the shipping sensors used in the direct SMART Impact sensors were reusable (plastic lid removable, forceps used to reset ball/spring/ball system, and consequently, impact sensor). The re-usable impact sensor on the left side of figure 21 is commercially available (OMNI-G from IOG Products) and activates at 100 g.

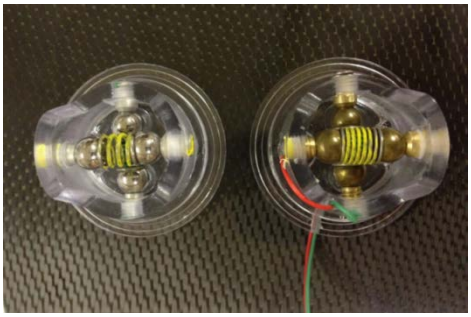

Figure 21. Reusable impact sensors with bases adhered to composite

Though the steel springs and steel balls form a conductive path, the resistance was too high (> 50KΩ) for use in a SMART Impact sensor. Consequently, IOG Products agreed to modify an OMNI-G impact sensor to make it suitable for use in a SMART Impact sensor. As shown on the right side of figure 21, the steel anvils (which hold the balls in place) were replaced with brass anvils, the steel balls were replaced with brass balls, and wires attached to the brass anvils were fed through the outer plastic holder to be attached to the IC bypass pads of a modified RFID tag. With these modifications, the brass/steel spring system resistance varied from 60Ω for the 5 g sensor to below 5Ω for the systems set to activate above 20 g (stiffer spring produced better contact between the anvil, ball, and spring). Using the linear motor impact tester in figure 17 to produce different impact speeds, no difference in detecting impact g-force levels was observed between the commercial (steel balls/springs) and modified (brass balls/springs/connecting wires) impact sensors.

To better simulate standard dropped-weight tests, such as ASTM D7136, a laboratory impact test was performed to evaluate the wired g-force sensor by dropping a 10 lb weight (the impacting surface was flat and had a 2.25″ diameter) by hand from approximately 6″ onto the composite panel (weight was caught after it bounced back up 3–4 inches). The velocity at impact was calculated to be 1.7 m/sec (6.1 KM/hr [3.9 Mi/hr]), which translates to a tow motor, forklift, etc. The high g-force of the shock wave traveling through the rigid composite was indicated by the fact that all the <100 g impact sensors were activated (stiffness of spring exceeded) by each impact of the 10 lb weight causing the resistance of the <100 G sensors to change from below 5Ω (balls in place [SMART Impact sensor unreadable]) to >6MΩ (circuit broken by falling balls [SMART impact sensor readable]) with each impact.

4.4 DROPPED-WEIGHT IMPACT TESTING OF CONDUCTIVE LINES

4.4.1 Introduction

The conductive surfaces of the rigid composite samples (0.15″ thick, eight plies of AGP370-5HS with 8552 epoxy resin) opposite the sides to be impacted had to be modified prior to applying the conductive lines. The modified composite surfaces were made nonconductive either by substituting a glass fiber cloth for one of the outer plies of carbon cloth when manufacturing the composite laminate or by applying a thin layer of epoxy to the composite surface (coat the conductive fibers protruding from the surface of the composite). Several conductive lines of silver epoxy/ink and silver acrylate ink (water- and solvent-based) were then applied to the nonconductive surface of each test composite panel to evaluate the capabilities of the different lines to detect surface cracks produced by different impact tests. The wired, modified OMNI-G sensor set to activate at 50 g (see figure 21) was adhered to each panel in an area without conductive lines prior to each impact test.

The first impact tests were performed with 4″ x 6″ samples (same size as ASTM D7136) using the highly instrumented linear motor impact setup in figure 17. As expected from the setup runs, the 50 g sensor was activated by each impact. However, even after several impacts were performed with the linear motor projectile, no damage was visible on either the impacted surface or the opposite surface with the epoxy coating/silver lines. The upper surface of the composite test specimen situated in the linear motor impact test setup in figure 17 was visible after three impact tests.

4.4.2 Composite Laminate With Glass Cloth Surface: Impact Test

Because the 4″ x 6″ inch composite sample was supported along all four edges by the rectangular cutout in the metal platform of the linear motor impact tester, the initial dropped-weight impact test was performed with a 12″ x 12″ laminate supported by a 12″ diameter circular metal ring (three or four sides supported; corners unsupported to increase the stress on the impacted composite). The crack detection capabilities of the silver acrylate line (Original Circuit Writer: water-based) drawn on one area of the nonconductive undersurface of the composite laminate produced with the glass cloth insulation layer (opposite side from impacts) were tested with the initial dropped-weight impact tests.

After five impacts with the 10 lb weight, a crack was visible in the surface of the impacted side of the composite laminate (see figure 22). On inspection of the underside with the glass layer/silver acrylate line, it could be seen that the crack on the impacted side went all the way through the laminate and was several inches in length, as shown in figure 22.

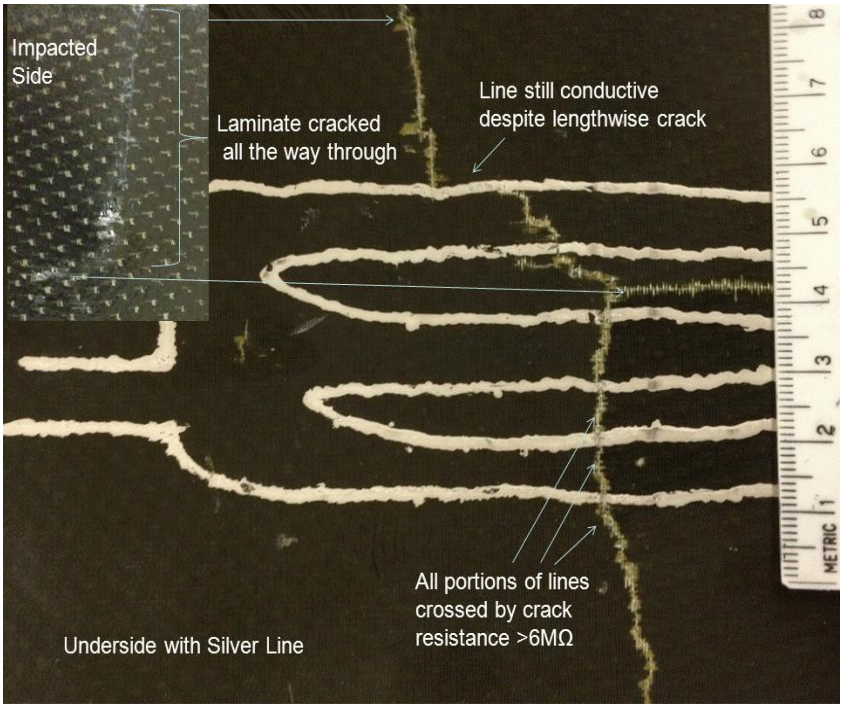

Figure 22. Impacted (upper left) and undersides of composite panel with extensive surface cracking from a dropped-weight impact test

The entire silver line shown in figure 22 had a resistance of 80Ω (cured overnight at room temperature) prior to the impact testing and a resistance of >6MΩ after the impacted surface crack was observed. It was determined by multiple resistance measurements that the areas of the line where the crack was not present or the crack ran lengthwise through the line were still highly conductive (<50Ω). The silver line became highly sensitive (>6M Ω) wherever the crack crossed it. These results indicate that the glass fiber successfully isolated the silver acrylate line from the conductive fibers protruding from the carbon matrix (fibers would have kept lines highly conductive despite crack) and that the silver lines were rugged (did not

flake off during impacts; remained conductive when crack was lengthwise).

The 12″ x 12″ glass cloth laminate was then shifted on the circular holder so that the crack-detection capabilities of the silver epoxy adhesive and ink lines (Creative Materials), drawn on a different area of the nonconductive surface (glass cloth layer) of the composite laminate, could be tested with the dropped-weight impact tests. As opposed to the initial test in figure 22, the underside surface was observed and the resistances of the conductive lines were determined after each weight drop. After the first weight drop, no changes were observed in the resistances of the conductive lines or underside surface appearance. After the second weight drop, even though the impacted surface had no apparent surface damage (<BVD), the resistance of one silver ink line on the underside increased dramatically to >6MΩ, and two short surface cracks had crossed the ink line, causing it to flake off (see figure 23).

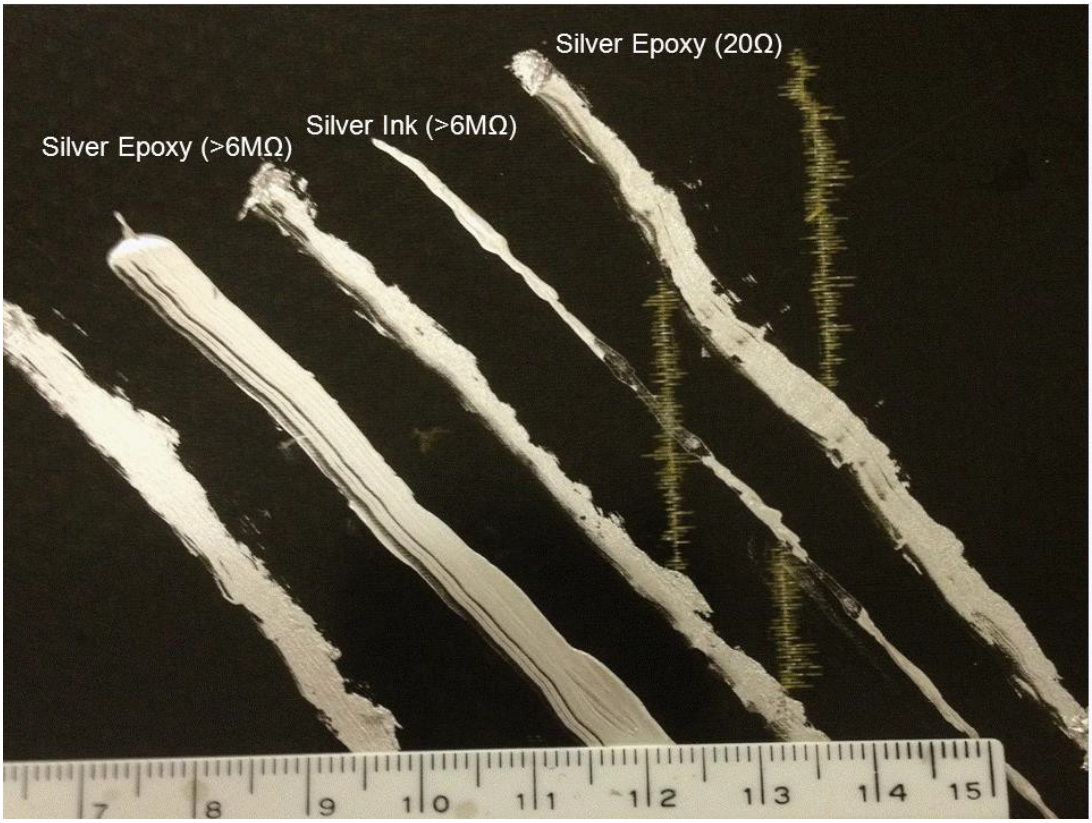

Figure 23. Underside surface of composite panel with surface cracks and silver epoxy, and ink lines from a dropped-weight impact test

The resistance of the silver epoxy line on the right side of figure 23 remained at 20Ω, even though the surface cracks came into contact with the edges of the line. In contrast, the middle silver epoxy line had a crack extending across the entire line and the resistance was >6MΩ. As with the silver acrylate lines, the crack had to extend across the silver epoxy line before the resistance of the line increased dramatically. In contrast, the silver ink lines flaked off of the composite surface in areas proximate to the surface cracks. Consequently, the silver epoxy adhesive and ink lines have different sensitivities to the presence of surface cracks for the nonconductive surface of the glass fiber composite panel. The silver epoxy adhesive and ink

lines remained completely intact (resistance <20Ω) in areas without cracks, confirming the ruggedness of the lines.

4.4.3 Composite Laminate With Glass Cloth Surface: Underside C-Scan Ultrasonic Analyses

In an attempt to correlate the cracks in the underside surface with the degree of internal damage to the composite laminate, the nonconductive underside surface of the 12″ x 12″ panel was analyzed using traditional ultrasonic techniques, such as C-scan amplitude and TOF. The C-scan amplitude image of the sound propagating through the entire laminate (amplitude scale: green, indicating the sound propagating through the area had minimal scatter [minimal damage], to dark blue/black, indicating that the sound underwent significant scatter/attenuation [delamination/void/conductive lines]), is shown in figure 24.

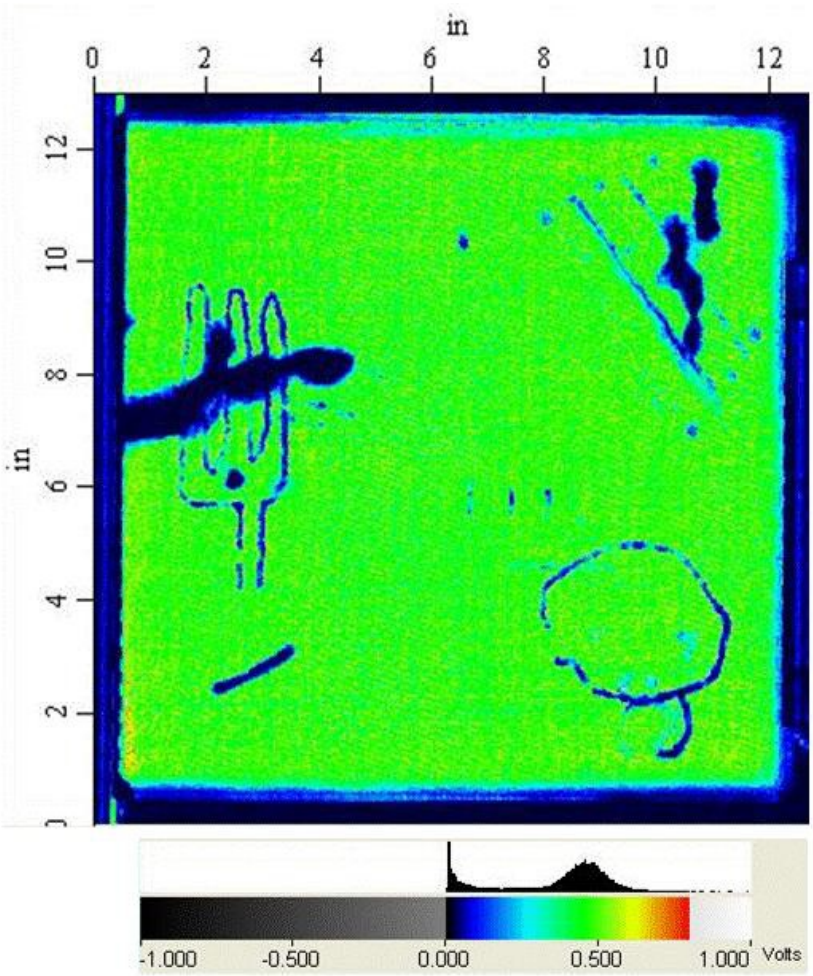

Figure 24. Ultrasonic C-scan amplitude image of underside of 12″ x 12″ composite panel after a dropped-weight impact test

The C-scan in figure 24 detected significant 1/2″ wide damage (delamination) in the same areas in which hairline surface cracks were observed/detected by the silver conductive lines in

figure 22 (delamination and long silver line on left side of C-scan) and figure 23 (delaminations and several silver lines in upper-right corner of C-scan).

The ultrasonic C-scan TOF image for the sound reflecting back from the underside (time scale in microseconds [µsec], in which green represents sound returning in the shortest period of time [upper surface] and dark blue/black represents the sound returning in the longest period of time [delaminations/voids/holes]) is shown in figure 25.

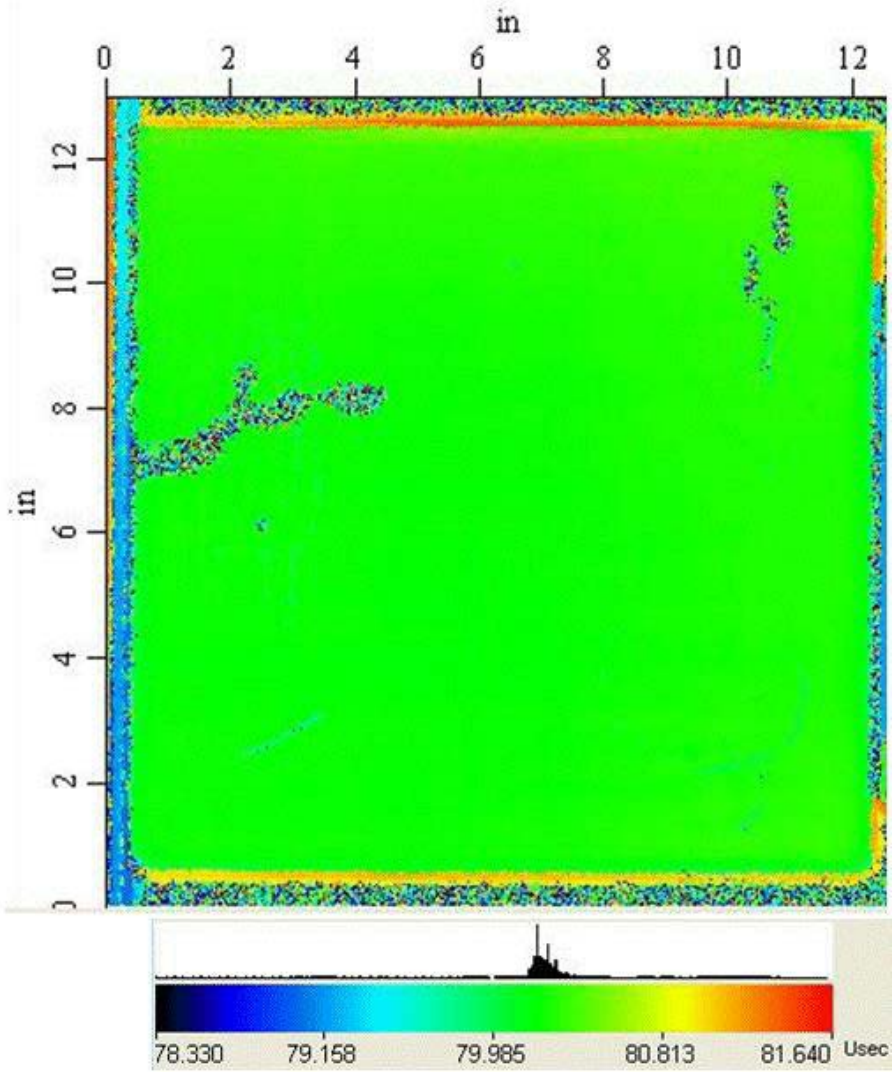

Figure 25. Ultrasonic C-scan TOF image of underside of 12″ x 12″composite after a dropped-weight impact test

Though the C-scan TOF analysis detected the same areas of damage as the amplitude image in figure 24, the image in figure 25 is unable to differentiate between the deep crack that went through the panel (left side) and the two internal delaminations (upper-right corner). These results indicate that the delaminations are widest at the underside surface (i.e., damage caused by impact shock wave expands as the wave passes from the impacted surface through the internal

ply/epoxy matrix and through the underside surface. Sound bounces back from the bottom of the delamination instead of penetrating into deeper sections, so all damage looks similar in depth).

4.4.4 Composite Laminate With Glass Cloth Surface: Cross-Section Analysis

The upper-right corner of the 12″ x 12″ composite panel in figure 23 was then cross-sectioned, polished, and viewed under magnification to determine the extent of the ply/epoxy matrix damage that occurred in the interior of the panel under one of the three detected surface cracks in figure 24. Figures 26(a) and 26(b) are the photographs taken under high magnification of the cross-sectioned areas without and with a surface crack, respectively. As opposed to the cross-section shown in figure 26(a), the majority of the plies under the surface crack underwent significant delamination/matrix cracking as evidenced by the damage (the network of white cracks) shown in figure 26(b).

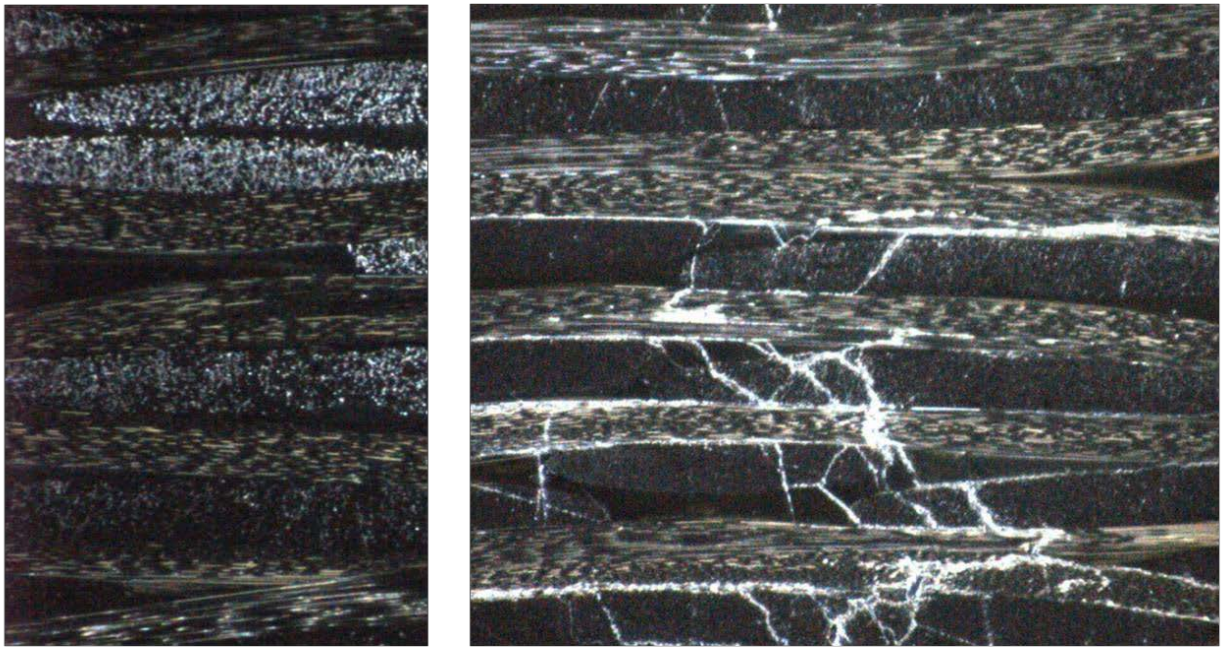

(a) (b)

Figure 26. Cross-sectioned composite (a) without and (b) with crack in the underside surface (bottom of pictures) from a dropped-weight impact test

4.4.5 Composite Laminate With Glass Cloth Surface: 3-Dimensional X-Ray CAT Analysis

To obtain a 3-D view of the delaminations under the surface crack, the cross-sectioned panel was then analyzed by x-ray CAT. The 3-D image provided by the x-ray CAT is actually a reconstruction of thousands of 2-D images (tomography literally means “the picture of a slice”) obtained as the sample was slowly rotated during successive x-ray analyses. For display in this report, the 3-D image (with associated cross-hairs used to locate the plane of damage being displayed) is broken down into three views: top (red/blue cross-hairs), end (green/blue), and side (green/red), as shown in figure 27.

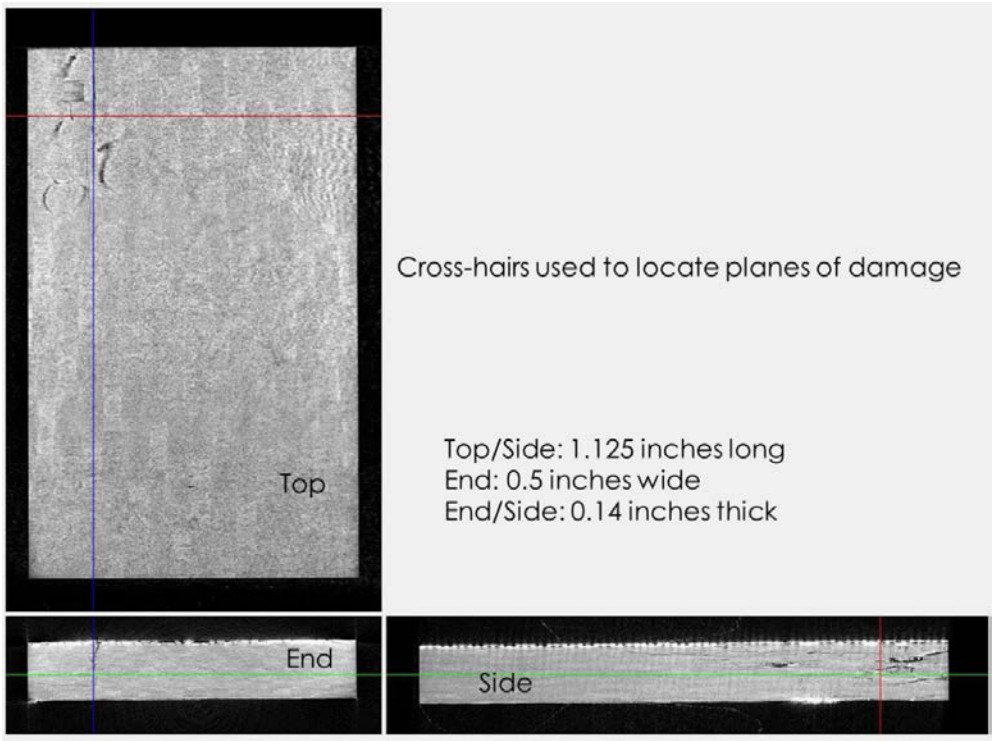

Figure 27. Three views and associated cross-hairs produced by x-ray CAT analysis of composite sample from a dropped-weight impact test

As opposed to the single view of internal damage revealed by the polished surface of the cross- sectioned sample in figure 26, all planes of internal damage in the impacted sample can be sequentially imaged on a computer screen by selecting a view (top, end, or side) and then slowly passed through the sample using the appropriate cross-hairs. Because of the size of the computer file and specialized software required to allow scanning through the thousands of images per view, representative x-ray CAT images of the sample under one crack in figure 23 are shown in the following images. For reference, figures 28(a) and 28(b) are the end and side view images of undamaged planes of the sample, respectively.

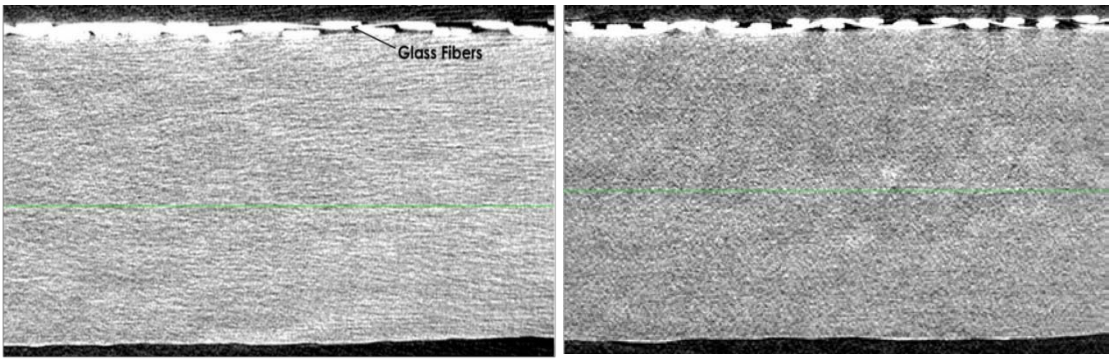

(a) (b)

Figure 28. The (a) end view and (b) side view x-ray CAT images of undamaged planes of composite sample from a dropped-weight impact test

Though the x-ray images in figure 28 do not differentiate between the alternating plies observed by the physical cross-section in figure 26, the x-ray image does differentiate the glass fiber layer (underside) from the woven carbon plies. The x-ray image is affected by density differences and the cross-section image highlights differences in light reflection; consequently, the x-ray image is very sensitive to the large difference in density between the composite matrix and the air inside the internal cracks and delaminations, as shown in figure 29.

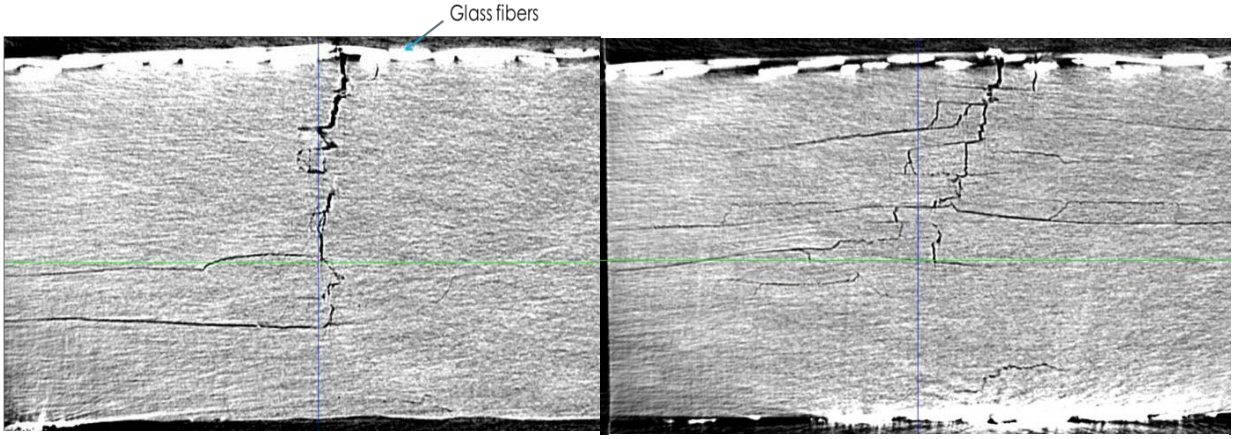

(a) (b)

Figure 29. The (a) end view and (b) side view x-ray CAT images of damaged planes of composite sample from a dropped-weight impact test

The images in figure 29 show that the underside surface cracks observed in figure 23 originate from the internal cracks and delaminations caused by the dropped-weight impacts. The cross-section (see figure 26) and x-ray CAT (see figure 29) images both indicate that the internal damage is concentrated near the underside of the sample, helping to explain the lack of damage observed in the impacted surface.

4.4.6 Composite Panel With Epoxy Coating: Silver Epoxy and Ink Lines

Though incorporating a glass fiber cloth into the surface of a composite laminate provided a surface that cracked during the impact testing and was nonconductive for application of the silver lines, incorporating a glass fiber cloth into the surface of an existing aircraft composite surface would be impractical. Therefore, the surface of a second composite laminate (eight plies of AGP370-5HS with 8552 epoxy resin) was coated with 8552 epoxy to provide a nonconductive surface for the application of silver epoxy adhesive/ink and silver acrylate conductive lines. Because it did not contain any carbon plies; the epoxy layer was expected to be more brittle to impact (i.e., form surface cracks) than the epoxy matrix of the laminate. The epoxy-coated composite laminate was cut into 4″ x 6″ panels prior to the impact tests to duplicate the test samples used in ASTM D7136 "Standard Test Method for Measuring the Damage Resistance of a Fiber Reinforced Polymer Matrix Composite to a Drop-Weight Event." To concentrate/direct the cracks produced by the dropped-weight impact, only the ends of the panels were supported. After three impacts with the 10-lb weight dropped from approximately 1 foot, the impacted surface of the panel had no visible damage, as shown in figure 30.

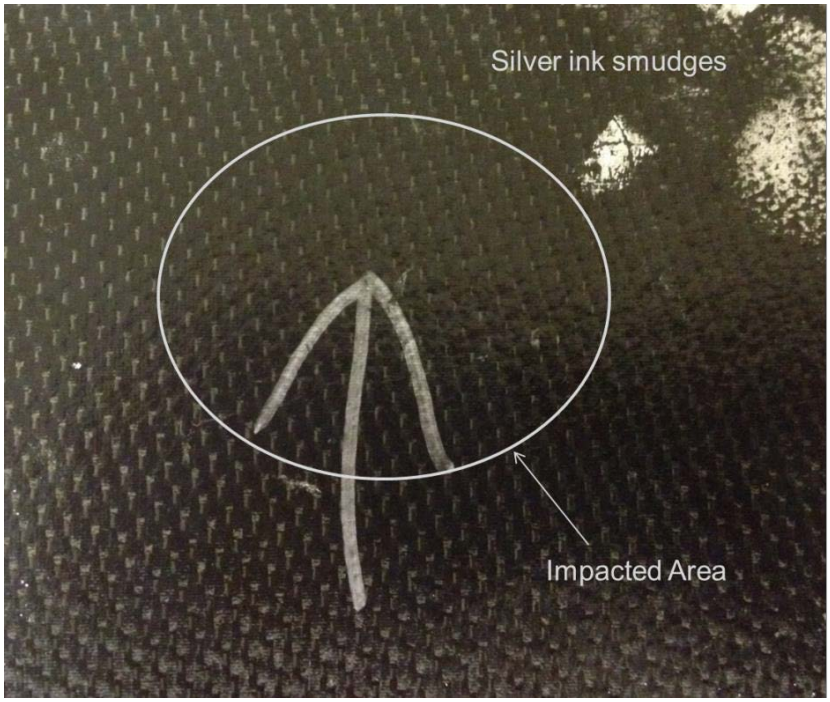

Figure 30. Impacted surface of composite panel with no visible damage from a dropped-weight impact test

Though the impacted surface had no visible damage from the three impacts, the underside surface of the panel with silver epoxy adhesive and ink lines contained three hairline cracks, as shown in figure 31.

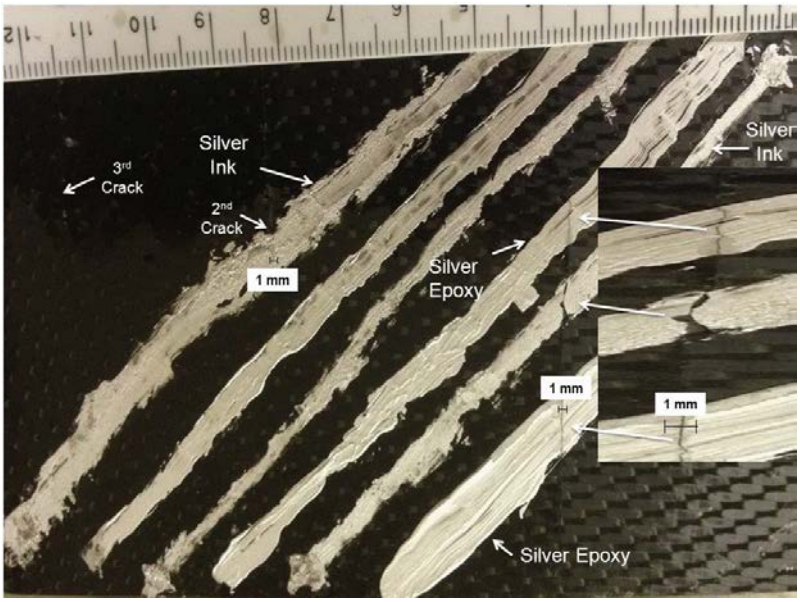

Figure 31. Underside surface of epoxy-coated panel with surface cracks and silver epoxy adhesive/ink lines from a dropped-weight impact test

As shown in figure 31, the surface cracks in the epoxy-coated composite are much narrower in width than the surface cracks in the glass fiber layer composite in figures 22 and 23 and are much more apparent in the surface of the white silver epoxy adhesive/ink conductive lines than the black composite surface. In areas without cracks, the resistances of the silver epoxy adhesive and ink lines remained below 10Ω after the multiple impacts with the 10-lb weight. Even though the hairline cracks are less than 0.1 mm in width, the resistances of the cracked silver epoxy conductive lines magnified in figure 31 were >6MΩ. The much-less-apparent second crack in figure 31 (left side) increased the resistance of the silver ink line to more than 100KΩ, sufficient to activate the SMART Crack sensor. These results indicate that the epoxy coating successfully isolated the rugged silver epoxy adhesive and the ink lines from the conductive fibers protruding from the carbon matrix (the fibers would have kept lines highly conductive despite cracking).

To confirm the surface cracks correlated with the internal damage of the composite laminate, the epoxy-coated underside surface of the 4″ x 6″ panel was analyzed using C-scan amplitude and TOF ultrasonic techniques (reflector plate signal). The C-scan amplitude image of the sound propagating through the entire laminate (amplitude scale: green [minimal damage], dark blue/black [delamination/epoxy lines]) is shown in figure 32.

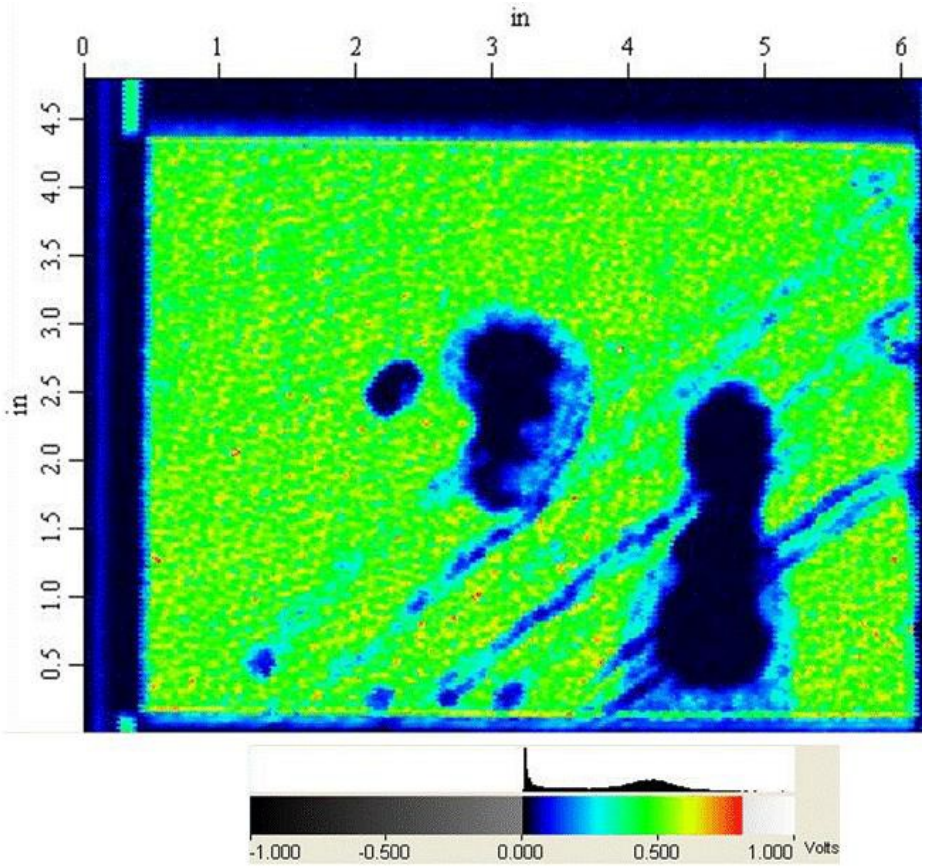

Figure 32. Ultrasonic C-scan amplitude image of epoxy-coated underside from a dropped-weight impact test

Though only hairline cracks formed in the epoxy coated surface during the dropped-weight impact test, the C-scan amplitude image in figure 32 detected significant, much wider (1″–2″) internal damage (delaminations/cracks) in the same areas in which the surface cracks were observed/detected by the silver conductive lines in figure 31.

The ultrasonic C-scan TOF image for the sound reflecting back from the underside (time scale in microseconds [µsec] in which green represents sound returning in the shortest period of time [surface] to dark blue/black for the sound returning in the longest period of time [delaminations/voids/holes]) is shown in figure 33.

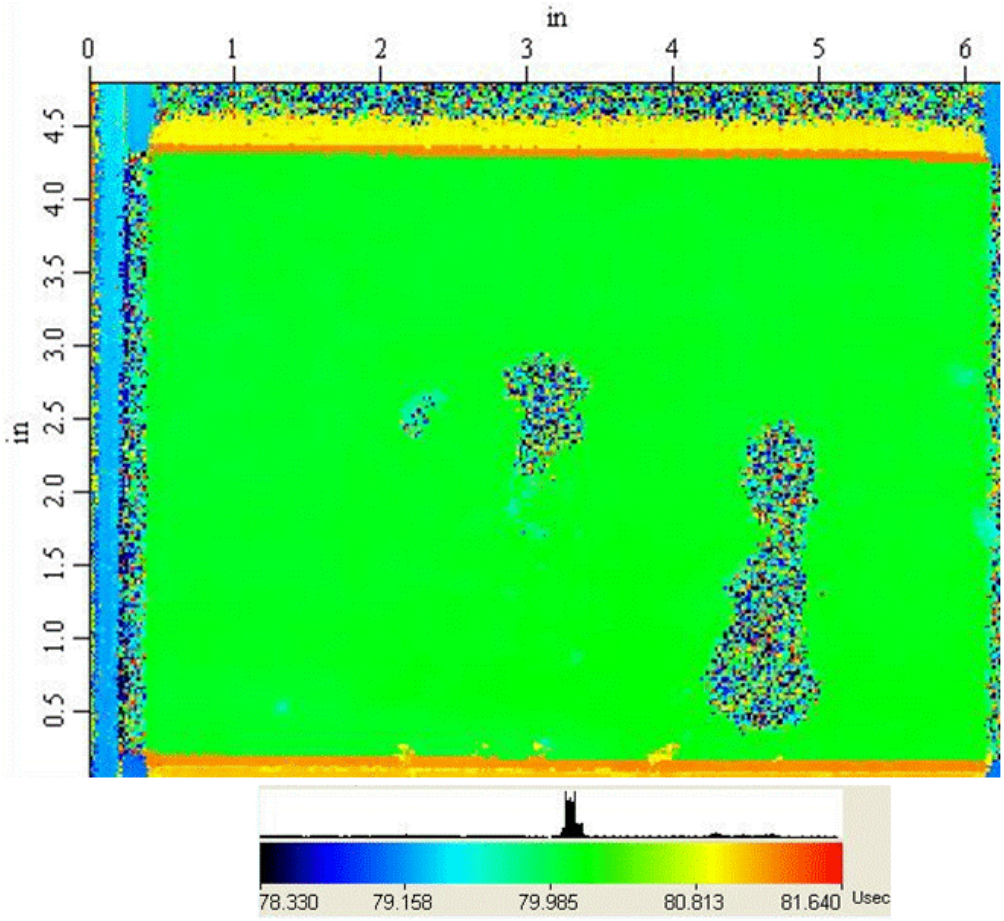

Figure 33. Ultrasonic C-scan TOF image of underside from a dropped-weight impact test

As seen with the 12″ x 12″ panel, the TOF ultrasonic image for the sound reflecting back from the entire laminate in figure 33 detected the same damage as the C-scan amplitude image in figure 32, but the TOF analysis again was unable to differentiate between the depths of the different areas of damage (i.e., the damage caused by impact shock wave expands as the wave passes from the impacted surface through the internal ply/epoxy matrix and out the underside; the majority of sound bounces back from the bottom of the delamination instead of penetrating into deeper sections, so all damage looks similar in depth). Therefore, the impacted side of the panel from the dropped-weight impact test was analyzed by ultrasonic C-scan TOF. The produced image (flipped horizontally to align the detected damage with the damage in figure 33) with the time scale is shown in figure 34.

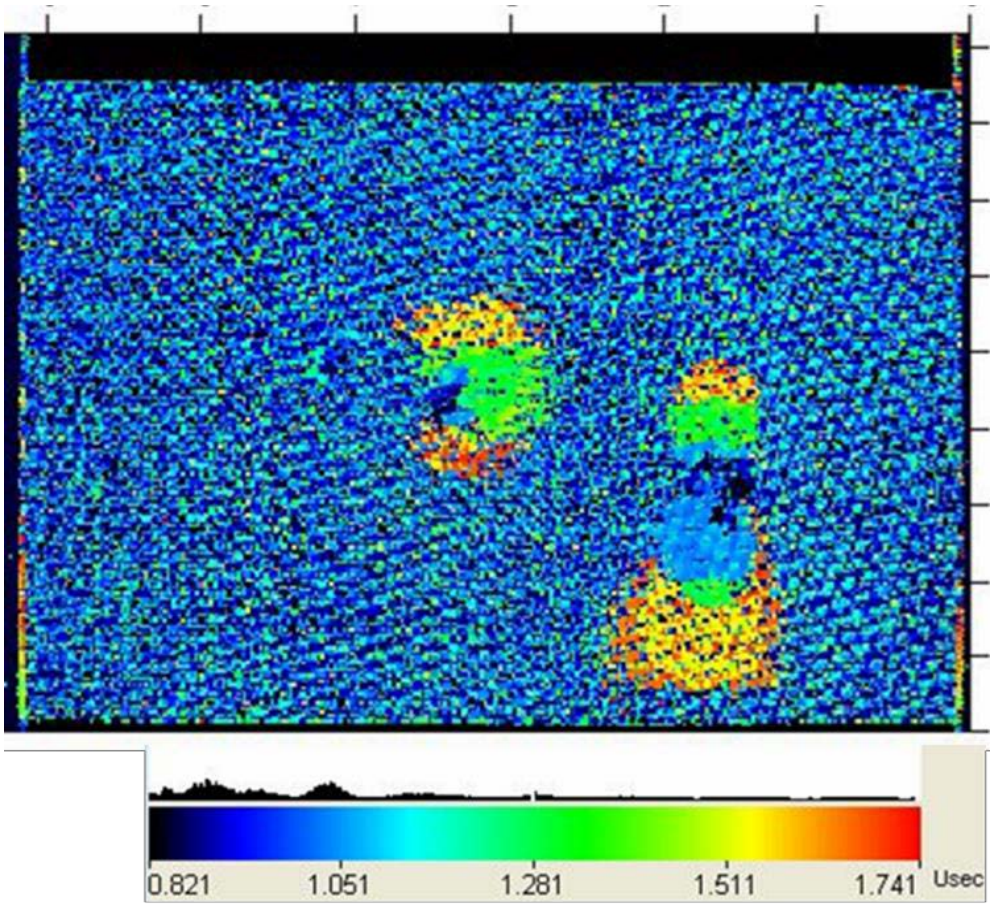

Figure 34. Ultrasonic C-scan TOF image of impacted side from a dropped-weight impact test

As opposed to the small (2.3 µsec) sporadic variations in the flight times for the damaged areas in figure 33, the flight times in figure 34 vary up to 9.2 µsec and are well defined with the longer flight times (deeper damage) detected at the ends of the delaminations (the damage widens as sound approaches the underside, in agreement with earlier ultrasonic, x-ray, and cross-section analyses). Therefore, to obtain the most damage characterization information of impacted composite panels, ultrasonic analyses will be performed at both the underside (C-scan amplitude: size of damage) and impacted side (TOF: depth of damage) surfaces.

4.4.7 Composite Panel With Epoxy Coating: Silver Acrylate Ink Lines

To test a non-epoxy based ink on the epoxy-coated panels (mismatch line and surface compositions), two different silver acrylate ink pens (original [water-based] and fast dry [solvent-based]) were used to draw lines on a second epoxy-coated panel. Again, the epoxy-coated composite laminate was a 4″ x 6″ inch panel to duplicate the test samples used in ASTM D7136. To concentrate/direct the cracks produced by the dropped-weight impact, only the ends of the panels were supported. After two impacts with the 10-lb weight dropped from approximately one foot, the impacted surface of the panel had no visible damage, similar to the surface shown in figure 30.

Though the impacted surface had no visible damage from the two impacts, the underside surface of the panel with the silver acrylate ink lines contained a hairline crack, as shown in figure 35.

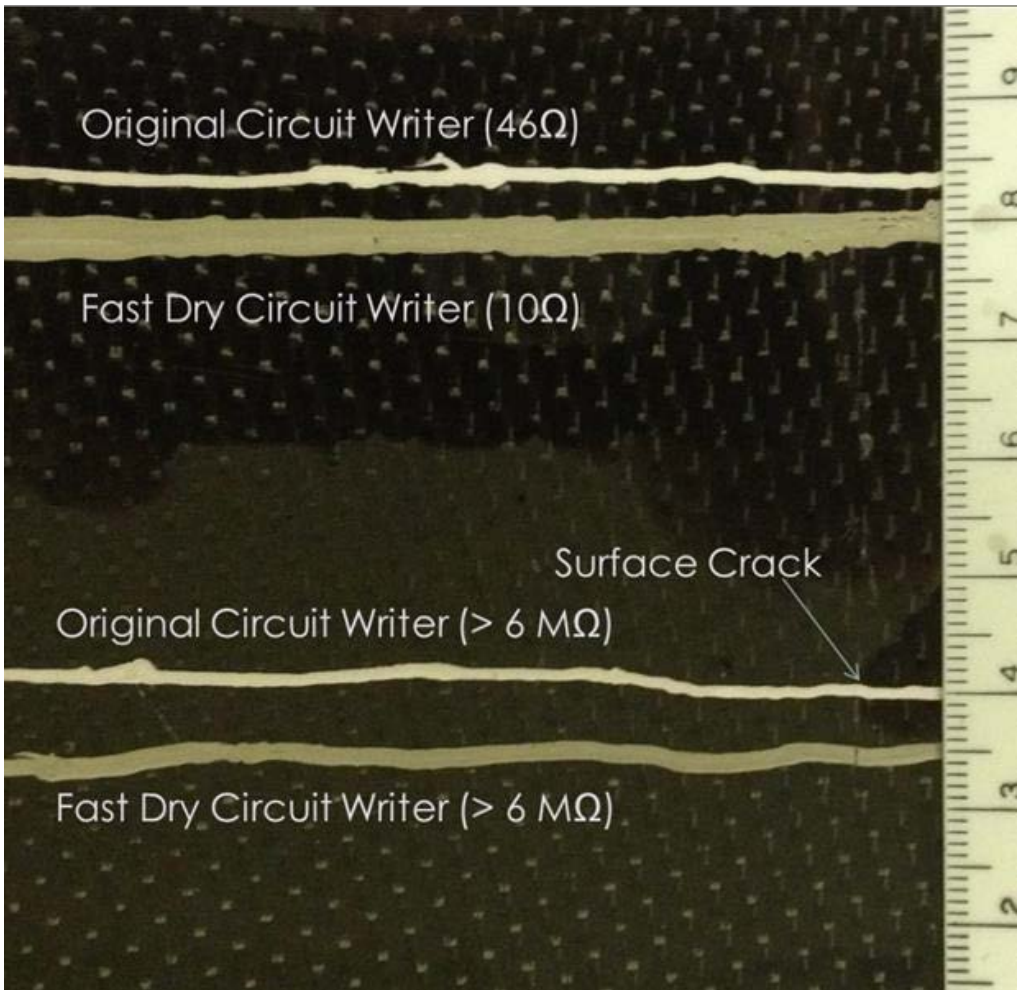

Figure 35. Underside surface of epoxy-coated panel with surface cracks and silver acrylate ink lines from a dropped-weight impact test

As shown in figure 35, the surface crack in the epoxy-coated composite is much narrower in width than the surface cracks in the glass fiber layer composite in figures 22 and 23 and is much more apparent in the surfaces of the white (water-based) and gray (solvent-based) conductive lines than the black composite surface. In areas without cracks, the resistances of the upper pair of silver acrylate lines remained below 50Ω after two impacts with the 10-lb weight. Even though the hairline crack identified in figure 35 is less than 0.1 mm in width, the resistances of the lower pair of cracked silver acrylate lines were >6MΩ. These results indicate that the epoxy coating successfully isolated the silver acrylate lines from the conductive fibers protruding from the carbon matrix (the fibers would have kept lines highly conductive, despite the crack).

In addition to the crack designated in figure 35, the upper conductive line drawn with the

solvent-based silver acrylate ink (fast-dry formula) had a small area with resistance >6MΩ, indicating the presence of a second, unobserved surface crack. To determine if both the observed and unobserved surface cracks correlated with internal damage of the composite laminate, the 4″ x 6″ panel was analyzed using C-scan amplitude (underside) and TOF (impacted side) ultrasonic techniques. The C-scan amplitude image of the entire panel with the amplitude scale for the sound propagating through the laminate (green [minimal damage], light blue lines [solvent based acrylate lines], and dark blue [delamination]) is shown in figure 36.

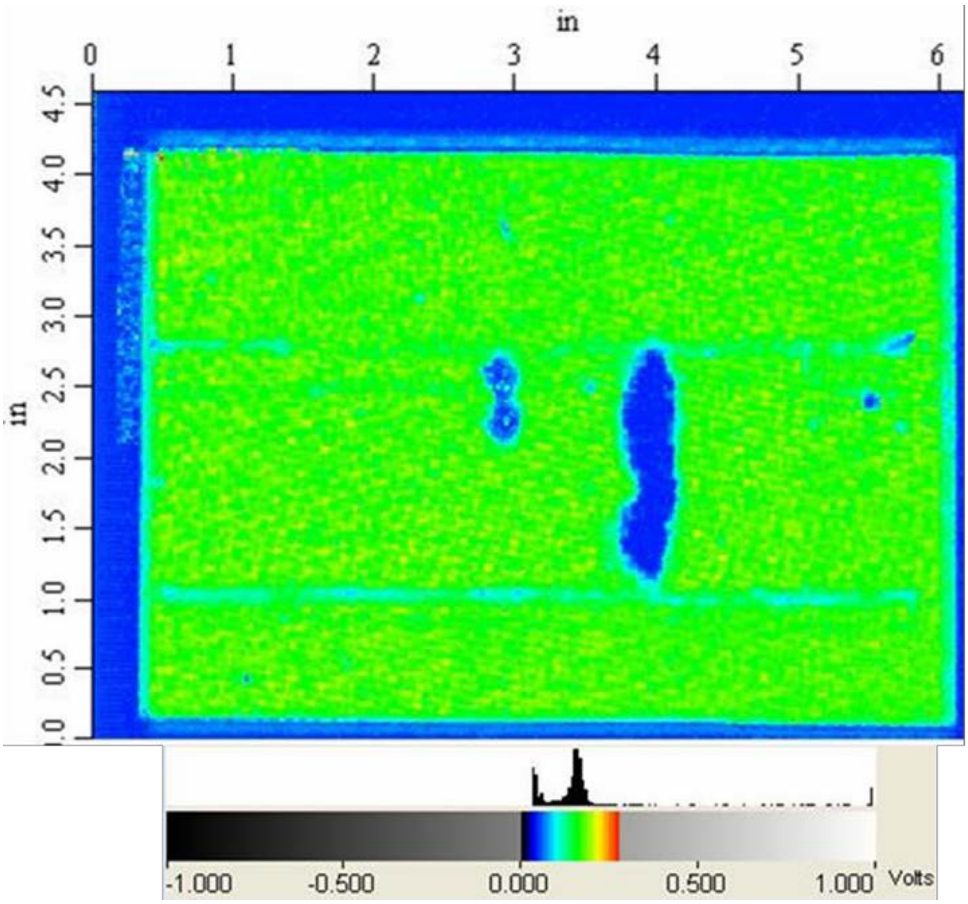

Figure 36. Ultrasonic C-scan amplitude image of epoxy-coated underside from a dropped-weight impact test

Though the observable crack that formed in the epoxy-coated surface during the dropped-weight impact test was less than 0.1 mm in width in figure 35, the C-scan amplitude image in figure 36 detected a significant, much wider (1″–2″) area of damage (delaminations/cracks) in the same area. The C-scan image also detected a second, much smaller area of damage, which correlated with the second area of the solvent-based silver acrylate line with increased resistance.

The impacted side of the panel from the dropped-weight impact test was then analyzed by ultrasonic C-scan TOF to characterize the severity/depth of the detected damage and produced image with the time scale, as shown in figure 37.

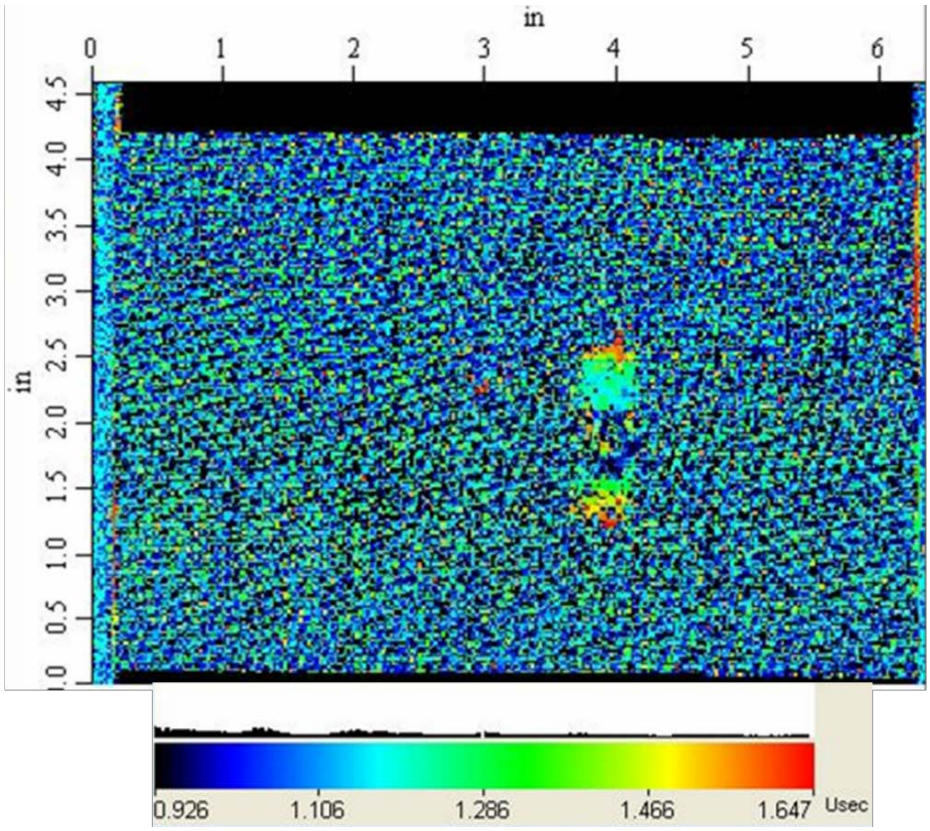

Figure 37. Ultrasonic C-scan TOF image of impacted side of epoxy-coated composite from a dropped-weight impact test

Though the flight times for the larger area of damage in figure 37 vary by 7.1 µsec, the areas with deeper damage (flight times up to 1.647 µsec) detected at the ends of the delaminations are much smaller and less defined than those in figure 34. The C-scan amplitude images in figure 32 (with dark blue/black centers) and figure 36 (with blue centers) also indicate that the level of internal damage is less for the impacted panel in figure 35 with the acrylate lines (two impacts) than for the impacted panel in figure 31 with the epoxy lines (three impacts).

The second, smaller area of damage identified in figure 34 is barely detectable (very shallow) in figure 37, appearing as red dots. Consequently, the second area of high resistance for the solvent-based silver acrylate line may be due to an unobserved crack that results from the small, shallow damage barely detected in figure 37. It might also be due to a line malfunction (poor adherence, unstable conductive particles, etc.).

4.4.7 RFID Tag Ruggedness

To ensure the overall ruggedness of the SMART sensors for impact detection, commercial 125 KHz RFID tags planned for use in the initial sensors were adhered to uncoated and epoxy-coated composite panels and subjected to multiple dropped-weight tests with the 10-lb weight. In every case, whether or not surface cracks formed, the adhered RFID tags remained readable, indicating their suitability for use on composite surfaces subjected to normal

physical forces and abnormal damaging impacts.

4.5 SUMMARY

The laboratory dropped-weight impact tests performed in Task 4 demonstrated that aerospace composite test specimens (eight plies of AGP370-5HS with 8552 epoxy resin) suffered significant internal damage without visible surface impact damage when a 10-lb projectile with a flat end was dropped from approximately 12″ (this simulates a forklift running into the side of an aircraft). As opposed to the impacted surface, the underside surface contained several cracks that originated from the internal damage. The internal damage and corresponding underside surface cracks were fully characterized by ultrasonic C-scans (amplitude and TOF), high magnification photography of sample cross-sections, and x-ray CAT scans. Even though the test specimens were held stationary during the impact tests, 100 g ball-spring accelerometers attached to the specimen underside surfaces by double-stick tape were activated by the shockwaves produced by the dropped-weight impacts.

The underside surfaces of the composite samples were made nonconductive either by substituting a glass fiber cloth for one of the outer plies of carbon cloth when manufacturing the composite laminate or by applying a thin layer of epoxy to the composite surface (to coat the conductive fibers protruding from the surface of the composite). The dropped-weight impact tests demonstrated that conductive lines of silver epoxy adhesive, silver epoxy ink, and silver acrylate inks (water-based and solvent-based) applied to the nonconductive underside surfaces were able to successfully detect (resistances increased from below 100Ω to more than 100KΩ) underlying surface cracks. Additional tests demonstrated that the RFID tag portion of the SMART Crack sensor would function properly after experiencing numerous impacts capable of producing underside surface cracks.

Therefore, the research performed in Tasks 3 and 4 demonstrated that a silver conductive line connected to an LF RFID tag has potential as a SMART Crack sensor to be used by maintenance personnel to identify composite components with internal damage, even though the exterior surface has no visible damage. Impact sensors connected to LF RFID tags have potential as SMART impact sensors to be used by maintenance personnel to record unreported impacts exceeding specified g-levels, but any resulting damage would have to be determined by other means (e.g., surface crack sensor, current maintenance procedures, etc.).

5. TASK 5: EVALUATION OF SMART SENSORS: SURFACE IMPACT TESTING

5.1 INTRODUCTION

Though the dropped-weight impact tests used in Task 4 demonstrated that composite panels could undergo internal damage without visible damage to the impacted surface, the impact tests were not performed under strict, instrumented conditions, and the significance of the internal damage with respect to the compression strengths of the impacted test panels was not determined. Therefore, the Compression-After-Impact (CAI) test method was performed in Task 5 to determine the significance of the internal damage produced under strict, instrumented impact conditions. The CAI test method is based on two ASTM test methods:

- ASTM D7136 "Standard Test Method for Measuring the Damage Resistance of a Fiber Reinforced Polymer Matrix Composite to a Drop-Weight Event"
- ASTM D7137 "Standard Test Method for Compressive Residual Strength Properties of Damaged Polymer Matrix Composite Plates"

As required by the CAI method, 4″ x 6″ test specimens were cut from rigid composite panels (0.15″ thick) produced from eight plies of AGP370-5HS with 8552 epoxy resin. The underside surface (opposite of impacted surface) of each composite test specimen was made nonconductive by applying a thin layer of 8552 epoxy to the composite surface (i.e., coating the conductive fibers protruding from the surface of the composite). Conductive lines of silver epoxy adhesive or silver acrylate ink were then applied to the nonconductive surfaces of selected test composite specimens to evaluate the capabilities of the different lines to detect underside surface cracks produced by the ASTM D7136 test method. The OMNI-G shipping shock sensors (see figure 21) preset to activate at 50 g were adhered to some of the initial test specimens with double stick tape (3M 9500PC) prior to preselected impact tests.

After each ASTM D7136 test was completed, the impacted surface was inspected for damage and the resistances of the conductive lines on the underside surface of the impacted composite specimen were measured to determine if a surface crack was detected (resistance increased from below 100Ω to more than 100KΩ). The internal damages of the impacted composite specimens were characterized by ultrasonic C-scan analyses (amplitude and TOF). Finally, the ultimate compressive strength of each impacted composite specimen was determined using the ASTM D7137 test method so that the effects of the produced internal damage on the specimen's structural strength could be quantified.

5.2 ASTM D7136 TEST METHOD: INITIAL SETUP

Based on the 10-lb flat weight used in the laboratory dropped-weight impact tests, a 5.6-lb projectile with a 1.75″ flat end was used in the ASTM D7136 test method in an attempt to produce significant internal damage without causing visible damage to the impacted surface. Initial tests determined that a 24.25″ drop height would produce visible surface cracks in the specimen underside—indicating internal damage—without producing visible damage to the impacted side. The drop-weight impactor used to perform the ASTM D7136 test method is shown in figure 38.

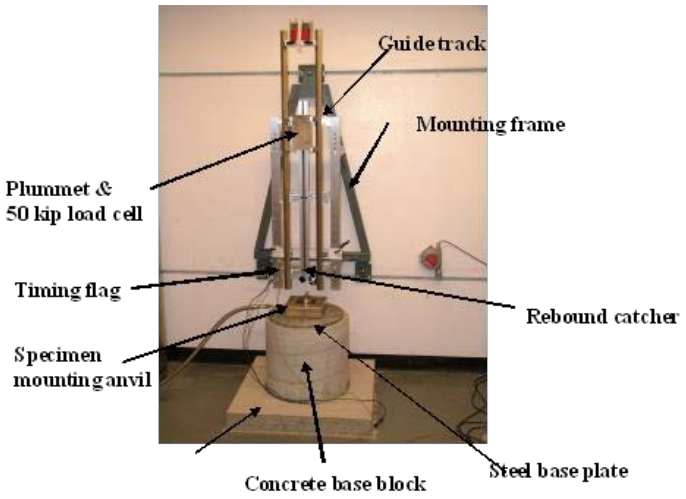

Figure 38. ASTM D7136 test method drop-weight impactor

5.3 ASTM D7136 TEST METHOD: IMPACTED TEST SPECIMENS

In contrast to the impacted test specimens from the laboratory dropped-weight impact tests, the impacted side surface of every ASTM D7136 impacted test specimen, regardless of drop height (21″–27″), had a pair of very thin semicircular marks (approximately 0.5″ in length) spaced 1.75″ apart (diameter of projectile), as shown in figure 39.

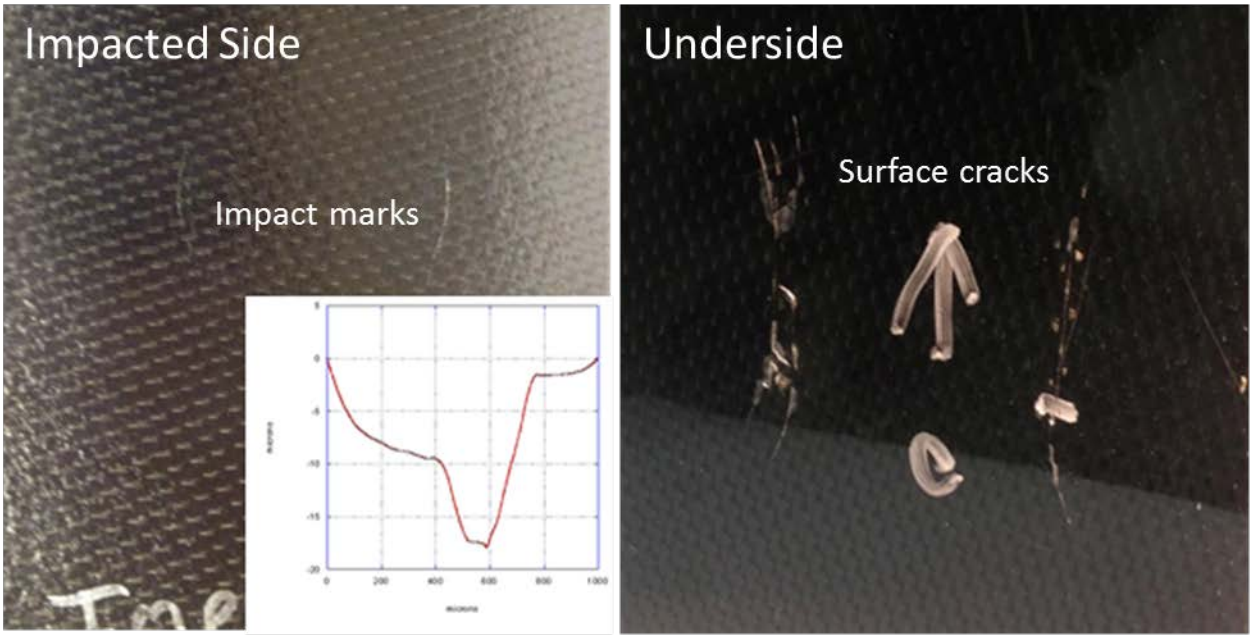

Figure 39. Photograph/surface profile of impacted surface marks and photograph of underside surface cracks for ASTM D7136 test specimen

The semicircular marks were not obvious and could only be seen close-up with special lighting, (i.e., the impacted side damage is much less than BVD [BVD seen from 5 feet away with

normal lighting]). A surface profilometer determined that the marks were less than 800 microns wide and had a dent depth of less than 20 microns (≈1 mil) (normal surface variations 10–15 microns), and therefore are much more shallow than the 20 mil (500 micron) acceptable skin dent depth associated with BVD.

The epoxy-coated underside surfaces of the ASTM D7136 test specimens had 1–2 semicircular cracks whose locations corresponded with the semicircular marks on the opposite impacted side. However, the semicircular cracks on the underside surface were much longer in length (reached up to 2″), were convex in shape (impact dents concave), and were quite visible, as shown in figure 39 (normal lighting).

To confirm the cracks in the underside surface were indicative of internal damage, the crack on the left side of the picture in figure 39 was cross-sectioned, polished, and photographed under high magnification. As seen with the laboratory dropped-weight impact test (glass fiber cloth underside surface shown in figure 26), the crack in the epoxy-coated underside of the ASTM D7136 test specimen originated from internal damage, as shown in figure 40.

Figure 40. Cross-sectioned composite with crack in the epoxy-coated underside surface (top) from ASTM D7136 impact test

Similar internal damage was also confirmed by an x-ray CAT scan.

5.4 ASTM D7136 TEST METHOD: TEST RESULTS

Once the initial test conditions for producing underside surface cracks without causing impacted surface damage were determined, two sets of composite specimens were impacted using the ASTM D7136 test method with a constant (24.25″) drop height. The resulting impact summary sheet with the recorded and calculated test data is shown in figure 41.

IMPACT Summary Sheet

Company:	Bob Kaufman
Job No.:	CNG
IFAS No.:	KM9051
Material:	AGP370+8552/Epon862/D230
Date:	8/27/2013
Micrometer I.D.:	F073D
Caliper I.D.:	F104D
Diameter of	1.75″ flat
Tested By:	John Stalter

Potential Energy = ASTM D7136, Equation 3

Impact Velocity = ASTM D7136, Equation 4

Measured Impact Energy = ASTM D7136, Equation 5

Specimen ID	Avg. Width (in.)	Avg. Length (in.)	Avg. Thick (in.)	Drop Mass (lbs.)	Drop Height (in.)	Potential Impact Energy (in. * lbf)	Impact Velocity (in./sec.)	Max Load Recorded (lbf)	Measured Impact Energy (J)	Measured Impact Energy (in* lbf)
CAI-1-1	4.0005	5.9878	0.1412	5.6	24.25	135.8	102.8	1703	8.69	76.9
CAI-1-2	4.0007	5.9923	0.1404	5.6	24.25	135.8	104.9	1684	9.03	79.9
CAI-1-3	3.9997	5.9865	0.1423	5.6	24.25	135.8	98.7	1557	8.01	70.9
CAI-1-4	4.0007	5.9868	0.1400	5.6	24.25	135.8	98.4	1611	7.96	70.4
CAI-1-5	3.9998	5.9895	0.1437	5.6	24.25	135.8	99.7	1914	8.16	72.2
Average:							**100.9**	**1694**	**8.37**	**74.08**
Standard Dev.							**2.83**	**136.19**	**0.47**	**4.15**
C.o.V.%							**2.81%**	**8.04%**	**5.60%**	**5.60%**
CAI-2-1	3.9998	5.9865	0.1415	5.6	24.25	135.8	99.4	1523	8.11	71.8
CAI-2-2	3.9993	5.986	0.1408	5.6	24.25	135.8	98.4	1459	7.96	70.4
CAI-2-3	3.9992	5.9855	0.1396	5.6	24.25	135.8	99.4	1591	8.11	71.8
CAI-2-4	3.9987	5.9880	0.1413	5.6	24.25	135.8	100.3	1576	8.26	73.1
CAI-2-5	3.9983	5.9790	0.1436	5.6	24.25	135.8	98.4	1606	7.96	70.4
Average:							**99.18**	**1551**	**8.08**	**71.51**
Standard Dev.							**0.80**	**60.19**	**0.13**	**1.11**
C.o.V.%							**0.81%**	**3.88%**	**1.55%**	**1.55%**

Figure 41. ASTM D7136 test data summary for 24.25″ drop-height impacts

The impacted specimens, CAI-1-1 through CAI-1-5, were submitted for C-scan analysis, then compressive strength testing, by ASTM D7137. In contrast, specimens CAI-2-1 through CAI-2-5 were impacted a second time using varied drop heights (21″, 24.25″, or 27″). The

resulting impact summary sheet with the recorded and calculated test data for the varied drop-height impacts for the twice-impacted specimens, CAI-2-1–CAI-2-5, and the set of once-impacted specimens, BK092013-4-4 through BK092013-4-6, are listed in figure 42.

DROP IMPACT Summary Sheet

Company: Bob Kauffman

Job No.: CNG

IFAS No.: KM9051

Material: 8-ply AGP370+8552/Epon862/D230

Date: 11/26/2013

Micrometer ID: F073D

Caliper ID: F104D

Diameter of Impactor: 1.75" flat

Tested by: John Stalter Testing Date: December 2013

Potential Energy= ASTM D7136, Equation 3

Impact Velocity = ASTM D7136, Equation 4

Measured Impact Energy = ASTM D7136, Equation 5

Specimen ID	Avg. Width (in.)	Avg. Length (in.)	Avg. Thick. (in.)	Drop Mass (lbs.)	Drop Height (in.)	Potential Impact Energy (in. * lbf)	Impact Velocity (in/sec.)	Max Load Recorded (lbf)	Measured Impact Energy (J)	Measured Impact Energy (in * lbf)
BK092013-4-4	4.003	6.003	0.1209	5.6	21	117 6	100.3	1564	8.26	73.1
2-CAI-2	3.998	5.9865	0.1415	5.6	21	117 6	98.3	1520	7.93	70.2
BK32	4.054	6.151	0.1335	5.6	21	117 6	99.2	1520	8.07	71.4
Average:							**99.3**	**1535**	**8.09**	**71.6**
Standard Dev.							1.00	25.40	0.17	1.47
C.o.V. %							1.01%	166%	2.05%	2.05%
BK092013-4-6	4.003	6.033	0.1206	5.6	24.25	135 8	105 6	1510	9.16	81.1
2-CAI-4	3.9987	5.988	0.1413	5.6	24.25	135 8	108.5	1672	9.66	85.5
2-CAI-5	3.9983	5.979	0.1436	5.6	24.25	1358	110.7	1637	10.07	89.1
Average:							**108.3**	**1606**	**9.63**	**85.2**
Standard Dev.							2.56	85.24	0.46	4.03
C.o.V. %							2.36%	5.31%	4.73%	4.73%
BK092013-4-5	4.003	6.003	0.1215	5.6	27	151 2	116.8	1500	11.21	99.2
2-CAI-1	3.9998	5.9865	0.1415	5.6	27	151 2	115.6	1500	10.97	97.1
2-CAO-3	3.9992	5.9855	0.1396	5.6	27	151 2	116.4	1574	11.13	98.5
Average:							**116.3**	**1525**	**11.10**	**98.3**
Standard Dev.							0.61	42.72	0.12	1.08
C.o.V. %							0.53%	2.80%	1.10%	1.10%

Figure 42. ASTM D7136 test data summary for varied drop-height impacts

The twice-impacted specimens, CAI-2-1–CAI-2-5, and once impacted specimens, BK092013-4-4–BK092013-4-6, were submitted for C-scan analysis, then compressive strength testing, by ASTM D7137.

5.5 ASTM 7137 TEST METHOD: TEST SETUP

After the C-scans were completed, the ultimate compressive strengths of the two sets of impacted composite specimens were determined using the ASTM 7137 test method. The compression test fixture used to perform ASTM D7137 is shown in figure 43.

Figure 43. Specimen loaded into compression fixture prior to test

To provide a baseline ultimate compressive strength for comparison with the ultimate compressive strengths of the impacted composite specimens, the ultimate compressive strengths of the unimpacted composite specimens BK092013-4-1–BK092013-4-3 were determined. The resulting compression summary sheet for the baseline composite specimens is shown in table 7.

Table 7. ASTM D7137 test data summary for the baseline composite specimens

Specimen Group	Avg. Area (in^2)	Avg. Max Compressive Load (lbf)	Avg. Ultimate Compressive Strength (Ksi)	Avg. X-Head Modulus (0.007 in/in – (0.009 in/in)
Baseline	0.4873	18634	38.25	3.80
Standard Deviation	0.00	1180.83	2.55	651.7
Coefficient of Variation (%)	0.36	6.34	6.68	17.13

5.6 ASTM 7137 TEST METHOD: TEST RESULTS AND SPECIMEN FAILURE MODES

To determine the percent loss of compressive strength caused by the 24.25″ drop-weight impacts of ASTM D7136, the ultimate compressive strengths of the once-impacted test specimens 1-CAI-1– 1-CAI-5 were determined. The resulting compression summary sheet for the 24.25″ drop-height impacted composite specimens is listed in figure 44.

Material	AGP370+8552/Epon862/D230
Panel No.	Panel-1
Operator ID	JDR
Instron Test Method	Compressive Residual Strength (ASTM D7137)
Job Number	CNG
PI Work Request	CNG-JS-13-060
Laboratory Name	Composites Manufacturing & Testing
Banner No.	KM9051
Test Temp	RT Dry
Test Speed (in/Min)	.05
Last test date	Tuesday, September 17, 2013
Testing Notes	Specimen 1 used 60 in/lbs torque, all others used 100 in/lbs torque

	Specimen Label	Area (in^2)	Extension at Max Comp. Load (in)	Max Comp. load (lbf)	Ult. Compressive Strength (ksi)	Modulus (0.001 in/in – 0.003 in/in) (ksi)	Testing Notes
~~X1~~	~~1 CAI-1~~	~~0.5648~~	~~0.056~~	~~16413~~	~~29.064~~	~~2026.389~~	No buckling observed. Vertical alignment slide came loose during testing. Excluded from results.
2	I-CAI-2	0.5618	0.063	19598	34.883	4496.584	A,B/M/T
3	I-CAI-3	0.5692	0.057	18289	32.131	4525.110	A/D/M
4	I-CAI-4	0.5599	0.070	20186	36.054	3071.073	A,B/M/T
5	I-CAI-5	0.5747	0.074	21106	36.723	4182.980	A/D/M
Mean		0.5664	0.066	19795	34.948	4068.937	
Standard Deviation		0.01	0.01	1180.12	2.03	683.06	
Coefficient of Variation (%)		1.21	11.27	5.96	5.80	16.79	

Figure 44. ASTM D7137 test data summary for the 24.25″ drop-height impacted composite specimens

Material	AGP370+8552/Epon862/D230
Panel No.	Panel-1
Operator ID	JDR
Instron Test Method	Compressive Residual Strength (ASTM D7137)
Job Number	CNG
PI Work Request	CNG-JS-13-060
Laboratory Name	Composites Manufacturing & Testing
Banner No.	KM9051
Test Temp	RT Dry
Test Speed (in/Min)	.05
Last test date	Tuesday, September 17, 2013
Testing Notes	Specimen 1 used 60 in/lbs torque, all others used 100 in/lbs torque

	Specimen Label	Area (in^2)	Extension at Max Comp. Load (in)	Max Comp. load (lbf)	Ult. Compressive Strength (ksi)	Modulus (0.001 in/in – 0.003 in/in) (ksi)	Testing Notes
~~X1~~	~~1 CAI-1~~	~~0.5648~~	~~0.056~~	~~16413~~	~~29.064~~	~~2026.389~~	No buckling observed. Vertical alignment slide came loose during testing. Excluded from results.
2	I-CAI-2	0.5618	0.063	19598	34.883	4496.584	A,B/M/T
3	I-CAI-3	0.5692	0.057	18289	32.131	4525.110	A/D/M
4	I-CAI-4	0.5599	0.070	20186	36.054	3071.073	A,B/M/T
5	I-CAI-5	0.5747	0.074	21106	36.723	4182.980	A/D/M
Mean		0.5664	0.066	19795	34.948	4068.937	
Standard Deviation		0.01	0.01	1180.12	2.03	683.06	
Coefficient of Variation (%)		1.21	11.27	5.96	5.80	16.79	

Figure 44. ASTM D7137 test data summary for the 24.25″ drop-height impacted composite specimens (continued)

Material	AGP370+8552/Epon862/D230
Panel No.	Panel-1
Operator ID	JDR
Instron Test Method	Compressive Residual Strength (ASTM D7137)
Job Number	CNG
PI Work Request	CNG-JS-13-060
Laboratory Name	Composites Manufacturing & Testing
Banner No.	KM9051
Test Temp	RT Dry
Test Speed (in/Min)	.05
Last test date	Tuesday, September 17, 2013
Testing Notes	Specimen 1 used 60 in/lbs torque, all others used 100 in/lbs torque

	Specimen Label	Area (in^2)	Extension at Max Comp. Load (in)	Max Comp. load (lbf)	Ult. Compressive Strength (ksi)	Modulus (0.001 in/in – 0.003 in/in) (ksi)	Testing Notes
~~X1~~	~~1 CAI-1~~	~~0.5648~~	~~0.056~~	~~16413~~	~~29.064~~	~~2026.389~~	No buckling observed. Vertical alignment slide came loose during testing. Excluded from results.
2	I-CAI-2	0.5618	0.063	19598	34.883	4496.584	A,B/M/T
3	I-CAI-3	0.5692	0.057	18289	32.131	4525.110	A/D/M
4	I-CAI-4	0.5599	0.070	20186	36.054	3071.073	A,B/M/T
5	I-CAI-5	0.5747	0.074	21106	36.723	4182.980	A/D/M
Mean		0.5664	0.066	19795	34.948	4068.937	
Standard Deviation		0.01	0.01	1180.12	2.03	683.06	
Coefficient of Variation (%)		1.21	11.27	5.96	5.80	16.79	

Figure 44. ASTM D7137 test data summary for the 24.25″ drop-height impacted composite specimens (continued)

The letters in the last column of figure 44 tie to the manner in which the test specimens failed during the compression test of ASTM D7137. These failure mode codes are defined in figure 45 (copied from ASTM D7137).

First Character		Second Character		Third Character	
Failure	Code	Failure Area	Code	Failure Location	Code
Angled	A	At end/edge	A	Bottom	B
Brooming	B	At/through damage	D	Left	L
End-crushing	C	Gage, away from damage	G	Middle	M
Delamination growth to edge at final failure, lengthwise	D	Multiple areas	M	Right	R
Through-thickness	H	Various	E	Top	T
Panel instability	I	Unknown	U	Various	V
Kink bands	K			Unknown	U
Lateral L					
Multimode	M (xyz)				
Delamination growth to edge prior to final failure, restrained by edge	R				
Long, Splitting	S				
Delamination growth to edge at final failure, widthwise	W				
Explosive	X				
Other O					

Figure 45. Three-place failure modes

According to ASTM D7137, all failure types are acceptable with the exception of codes C (end-crushing) and R (delamination grows prior to final failure and additional force-carrying capability results from edge restraint). Test specimen 1-CAI-1 slipped out of the holder during the test and, therefore, did not undergo failure. Based on the codes in figure 46, impacted test specimens 1-CAI-2 and 1-CAI-4 had angled/brooming type failures in multiple areas at the top and test specimens 1-CAI-3 and 1-CAI-5 had angled-type failures through the damage in the middle. The two types of compression failures as well as the impact-induced cracks in the epoxy-coated underside surfaces are shown in figure 46 for test specimens 1-CAI-2–1-CAI-5.

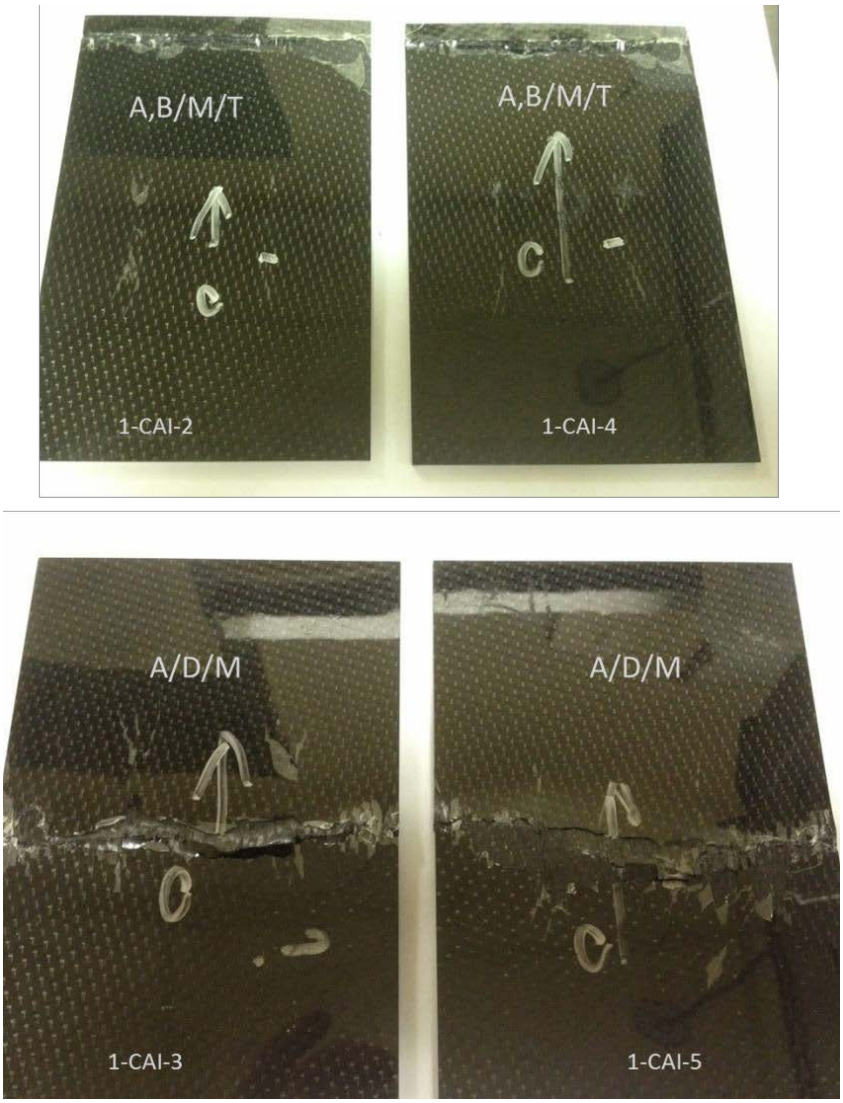

Figure 46. Photographs of ASTM D7137 test specimens 1-CAI-2–1-CAI-5, illustrating the two different failure modes

To determine the percentage of loss of compressive strength caused by the single and double impacts using drop heights ranging from 21″–27″, the ultimate compressive strengths of the twice-impacted test specimens CAI-2-1–CAI-2-5 and the once-impacted specimens BK092013-4-4–BK092013-4-6 were determined. The resulting compression summary sheets for the 21″, 24.25″, and 27″ drop-height impacted composite specimens are listed in figure 47.

Job Number	CNG
PI Work Request	CNG-JS-14-004
Laboratory Name	Composites Manufacturing & Testing
Operator ID	JDR
Instron Test Method	Compressive Residual Strength (ASTM D7137)
Lab Temp. (°F)	70
Lab Humidity (%)	34
Test Temp	RT Dry
Test Speed (in/min)	.05
Material	8-ply AGP370
Panel No.	8-ply AGP370
Test Date	January 28, 2014
Impact Conditions	21 in. Drop Height

	Specimen Label	Area (in^2)	Extension @ Max Comp. Load (in)	Max Comp. Load (lbf)	Ult. Compressive Strength (ksi)	Modulus (0.005 in/in - 0.007 in/in) (ksi)	Testing Notes
1	BK092013-4-4	0.4840	0.075	17383	35.918	4542.741	Fracture at top
2	2-CAI-2	0.5660	0.065	17651	31.187	4212.019	Fracture through midpoint

Test Date	February 14, 2014
Impact Conditions	24 in. Drop Height

	Specimen Label	Area (in^2)	Extension @ Max Comp. Load (in)	Max Comp. Load (lbf)	Ult. Compressive Strength (ksi)	Modulus (0.005 in/in - 0.007 in/in) (ksi)	Testing Notes
1	2-CAI-4	0.5650	0.072	17330	30.672	4172.126	Fracture through midpoint
2	2-CAI-5	0.5742	0.074	20083	34.978	4437.599	Fracture through midpoint
3	BK092013-4-6	0.4828	0.071	18282	37.869	4917.106	Fracture through midpoint

Test Date	January 31, 2014
Impact Conditions	27 in. Drop Height

	Specimen Label	Area (in^2)	Extension @ Max Comp. Load (in)	Max Comp. Load (lbf)	Ult. Compressive Strength (ksi)	Modulus (0.004 in/in - 0.005 in/in) (ksi)	Testing Notes
1	2-CAI-1	0.5660	0.056	16773	29.635	4383.499	Fracture through midpoint
2	2-CAI-3	0.5583	0.057	16487	29.531	4408.590	Fracture through midpoint
3	BK092013-4-5	0.4864	0.081	19013	39.093	4559.534	Fracture through midpoint
Mean		0.5369	0.065	17424	32.753	4450.541	
Standard Deviation		0.04	0.01	1383.51	5.49	95.22	
C.o.V %		8.18	21.97	7.94	16.76	2.14	

Figure 47. ASTM D7137 test data summary for the 21″, 24.25″, and 27″ drop-height impacted composite specimens

Except for once-impacted (21″ drop height) specimen BK092013-4-4, which broke at the top (similar to 1-CAI-2 and 1-CAI-4 in figure 47), and twice-impacted (24″ drop heights) 2-CAI-5, which broke well below the damage, all the test specimens broke in the middle through the damage. Except for once-impacted (27″ drop height) specimen BK092013-4-5, all of the specimens broke horizontally across the surface, similar to 1-CAI-3 in figure 46. The

epoxy-coated underside surfaces of test specimens 2-CAI-5 and BK092013-4-5, which broke differently than the other impacted test specimens, are shown in figure 48.

Figure 48. Photographs of ASTM D7137 test specimens 2-CAI-5 and BK092013-4-5 illustrating the different failure modes

5.7 COMPARISON OF C-SCAN IMAGES WITH CAI TEST RESULTS

5.7.1 Single Drops from 24.25″

The first set of test specimens (1-CAI-1–1-CAI-5) was used to determine if the ASTM D7136 test method could be used to create internal damage/underside surface cracks without producing visible damage to the impacted surface. The ASTM D7137 test method was then used to determine whether the internal damage had a significant effect on the compressive strength of the impacted test specimen. Prior to the ASTM D7137 compression failure testing, each baseline and impacted test specimen was analyzed for internal damage using ultrasonic C-scan analyses. For each panel, four C-scan images were produced:

- Back surface signal (view from impacted surface) amplitude/TOF
- Reflector plate signal (view from underside surface) amplitude/TOF

To ensure there were no pre-existing delaminations/voids inside the manufactured test specimens, all of them were analyzed prior to the ASTM D7136 impact test. Except for an occasional air bubble (shown in figure 49), all of the test specimens were produced without internal imperfections.

ASTM 7136
Not Performed –Baseline Panels

ASTM 7137
Ultimate Compressive Strength = > 38.2 ksi
(Average of Three panels, All Broke at Top)

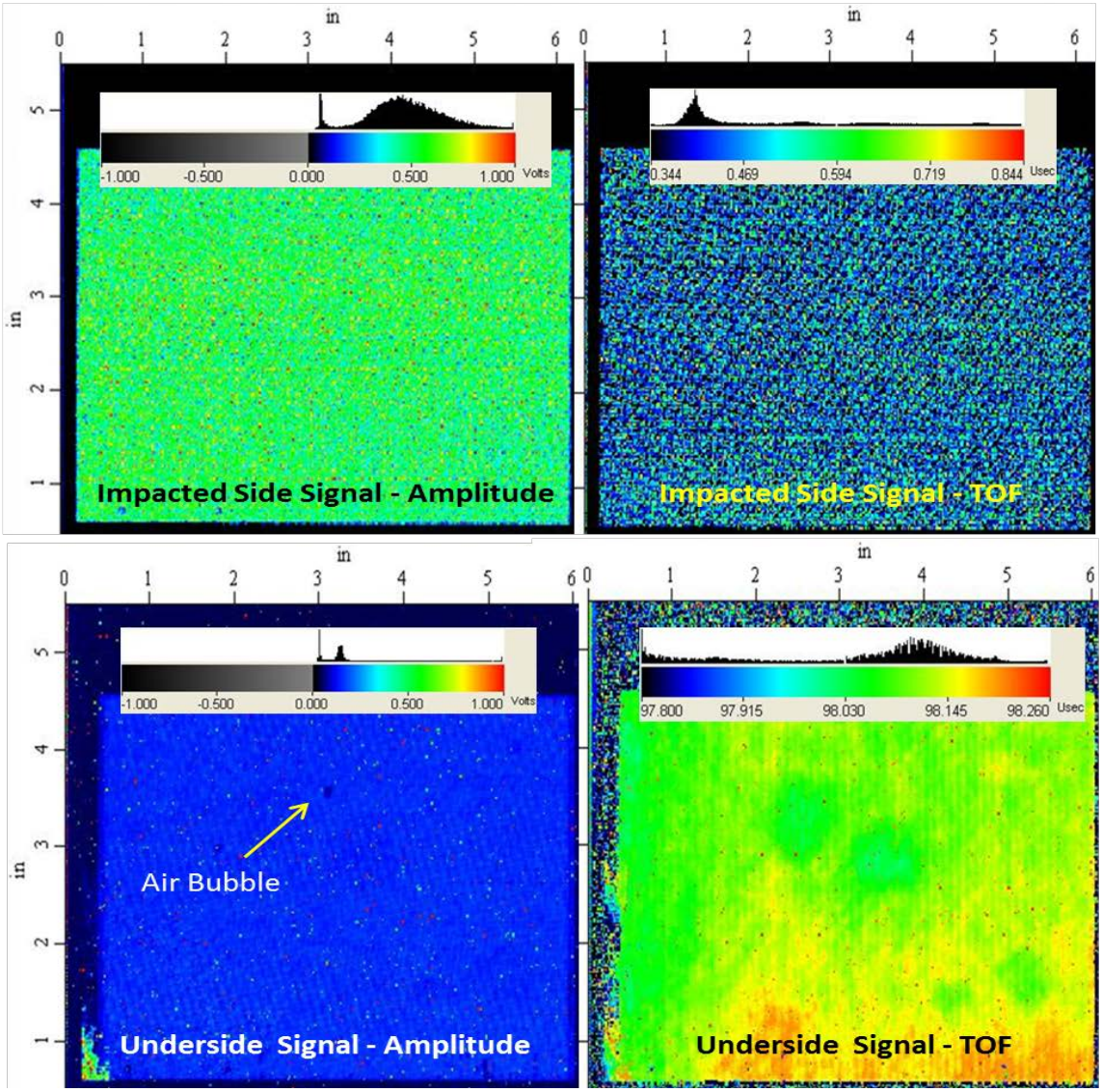

Figure 49. C-scans (amplitude and TOF) and ASTMD7137 test data for a baseline test specimen with epoxy-coated underside before impact

As shown in figure 49, the ultimate compressive strengths of the baseline test specimens were equal to or greater than 38.2 kilopounds per square inch (ksi). Because the test specimens broke at the top before the middle, it is proposed that the ultimate strength at the middle of the test specimens is equal to or greater than that determined for the top of the test specimens. To determine if the ultimate compressive strengths of the impacted test specimens decreased as the internal damage characterized by the ultrasonic C-scan analyses increased, the C-scan (amplitude and TOF) images and ASTM D7136/D7137 (CAI) test data of the impacted test specimens 1-CAI-2 through 1-CAI-5 are arranged by decreasing ultimate compressive strengths in figures 50 and 51.

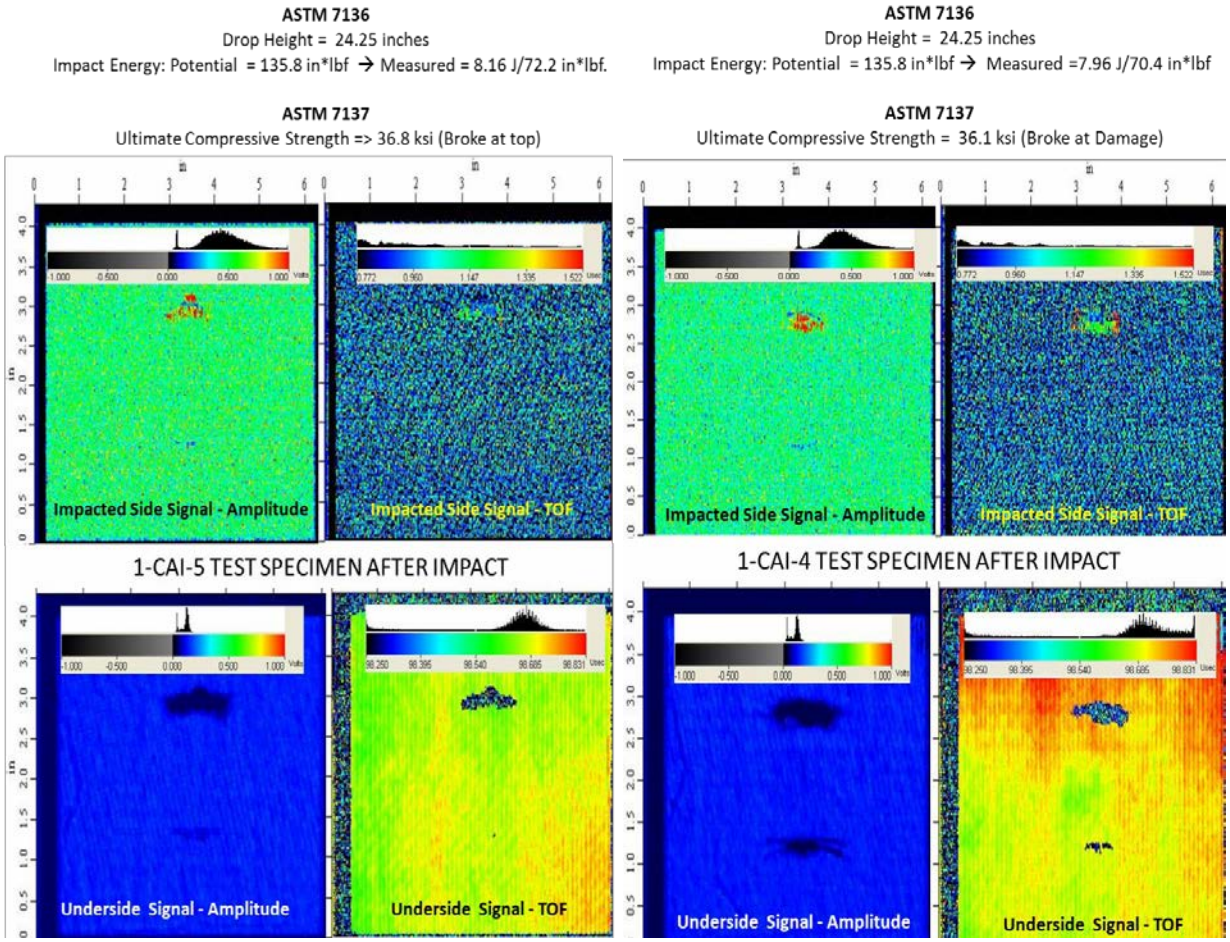

Figure 50. C-scans (amplitude and TOF) and CAI test data for impacted test specimens 1-CAI-5 and 1-CAI-4 with epoxy-coated underside surfaces

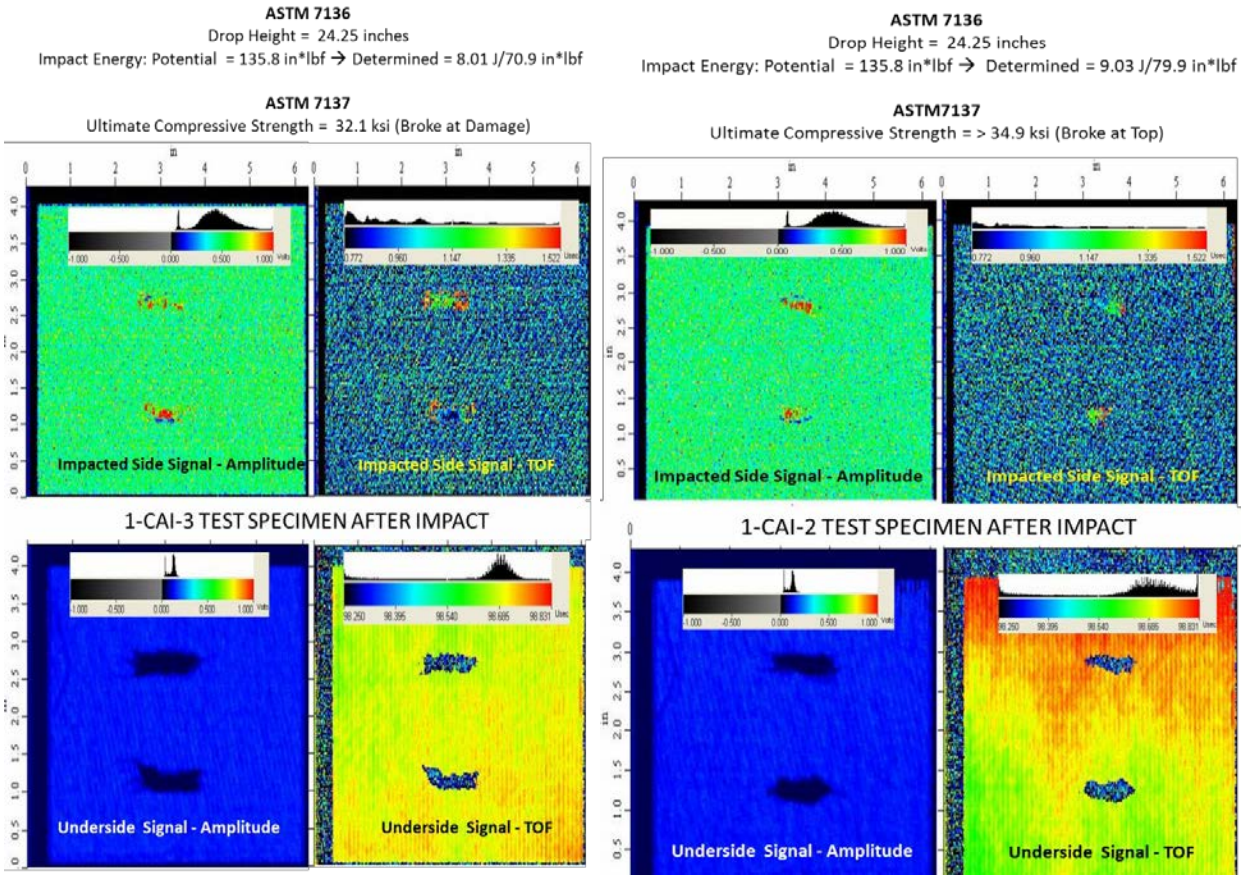

Figure 51. C-scans (amplitude and TOF) and CAI test data for impacted test specimens 1-CAI-2 and 1-CAI-3 with epoxy-coated underside surfaces

Even though the drop height was constant (24.25″) and the measured impact energies were consistent, the ultrasonic C-scan images in figures 50 and 51 indicate that the levels of internal damage suffered by the different test specimens were quite different. Impacted test specimens 1-CAI-5 and 1-CAI-4 contain one distinct area of damage, and 1-CAI-2 and 1-CAI-3 contain two distinct areas of damage. In addition, the main area of damage in 1-CAI-5 has minimal depth (impacted side TOF image has no red apparent) compared to the main area(s) of damage in the other test specimens.

As shown in figures 50 and 51, there is an inverse relationship between the size/number/depth of the damaged areas detected by the ultrasonic C-scan images and the ultimate strength of the test specimen. Based on the 38.2 ksi ultimate strength of the baseline samples, impacted test specimens 1-CAI-4 and 1-CAI-5, with one main area of damage, suffered a 4%–5% loss of ultimate compressive strength, and 1-CAI-2 and 1-CAI-3, with two areas of damage, suffered 9% and 16% losses, respectively.

Therefore, ASTM D7136 was able to produce internal damage (see figures 50 and 51) in the composite test specimens, which resulted in corresponding underside surface cracks (see figure 46) and a significant loss of compressive strength without producing visible damage in the impacted surfaces (the two impact dents in figure 39 had a depth of approximately

20 microns [1 mil]; BVD dent depth is approximately 500 microns [20 mil]).

5.7.2 Single Drops From 21″–27″

A second set of test specimens, BK092013-4-4 and BK092013-4-6 (BK092013-4-1–BK092013-4-3 were used as baseline test specimens), were ASTM D7136 test-impacted from drop-heights of 21″–27″ to produce different levels of internal damage/loss of compressive strength. The drop-height range was selected to produce internal damage (and cracks in the epoxy-coated underside surface) without producing visible damage to the impacted surfaces. Each impacted test specimen was first analyzed for internal damage using the ultrasonic C-scan (amplitude and TOF) analysis techniques, then tested for ultimate compressive strength by ASTM D7137.

As listed in figure 49, the ultimate compressive strengths of the baseline test specimens were equal to or greater than 38.2 ksi. To compare the ultimate compressive strengths of the impacted test specimens with different drop heights, the C-scan (amplitude and TOF) images of the impacted test specimens BK092013-4-4 through BK092013-4-6, with the CAI (ASTM D7136/D7137) data included, are arranged by increasing drop heights in figures 52 and 53.

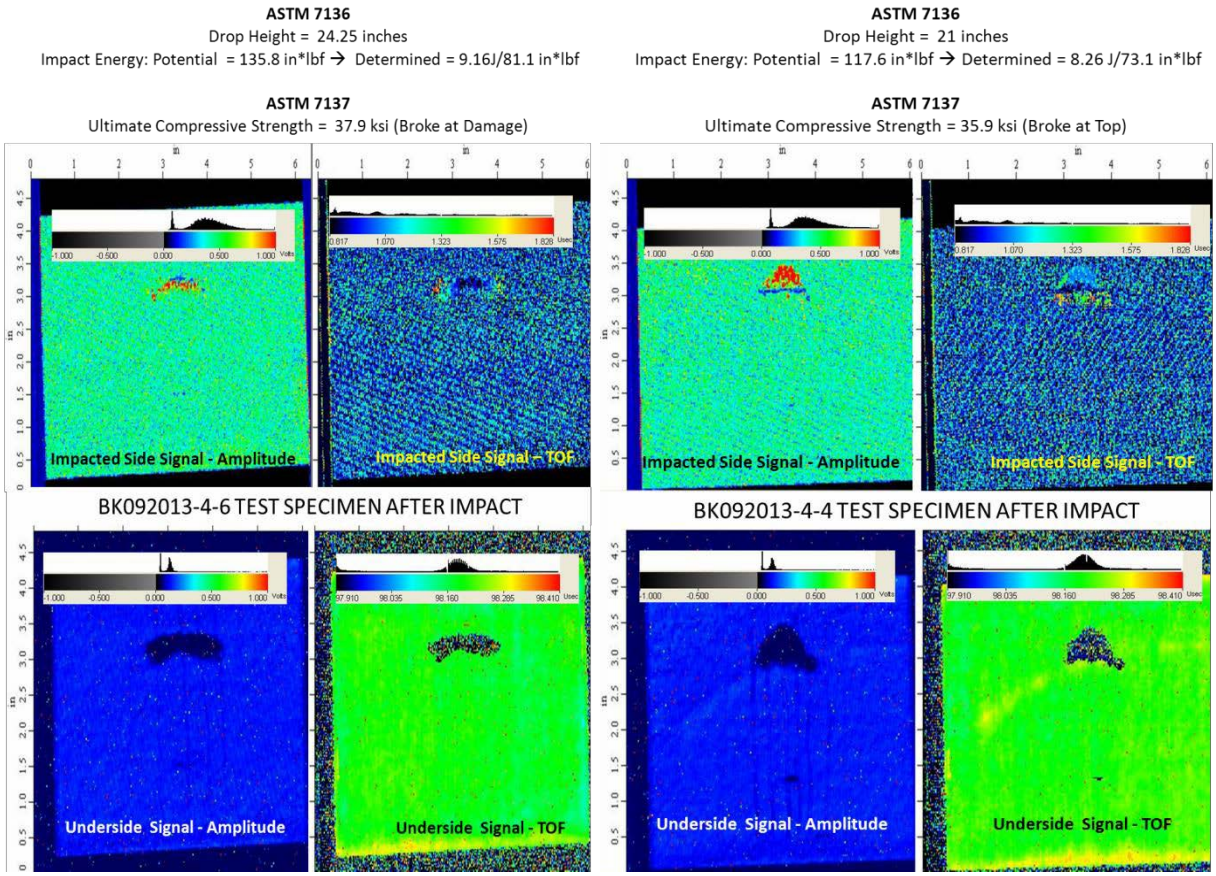

Figure 52. C-scans (amplitude and TOF) and CAI test data for impacted test specimens 92013-4-4 and 92013-4-6 with epoxy-coated underside

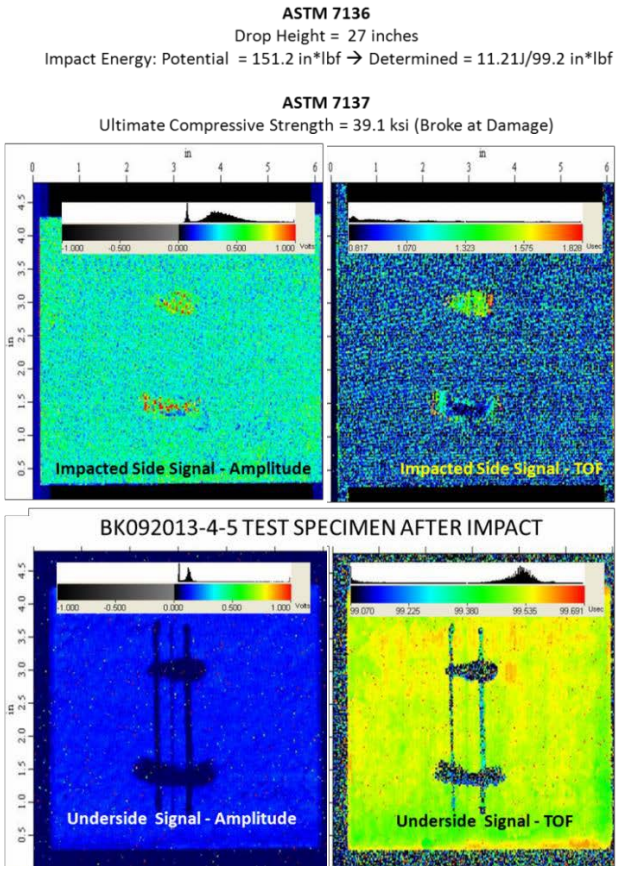

Figure 53. C-scans (amplitude and TOF) and CAI test data for impacted test specimen 92013-4-5 with epoxy-coated underside (epoxy lines)

Even though the drop height was increased from 21″ to 24.25″ in figure 52, the ultrasonic C-scan images of the internal damage suffered by the two test specimens are similar, with each specimen containing one distinct area of damage of similar depth. The C-scans in figure 52 are very similar to those for the 24.25″ impacted test specimen, 1-CAI-5 in figure 50, with the one area of damage. When the drop height was increased from 24.25″ to 27″, the internal damage detected by the C-scans increased, as shown in figure 53, and are very similar to those for the 24.25″ impacted test specimens, 1-CAI-2 and 1-CAI-3, with the two areas of damage in figure 51.

Even though the levels of internal damage shown in figures 52 and 53 are similar to those shown in figures 50 and 51, there was no apparent relationship between the size/number/depth of the damaged areas detected by the ultrasonic C-scan images and the measured ultimate strengths of the test specimens. Though one area of damage test specimens, BK092013-4-4 and BK092013-4-6, as well as 1-CAI-4 and 1-CAI-5, suffered small (<7%) losses of ultimate compressive strength, the higher drop height/two areas of damage for BK092013-4-5 in figure 53 did not suffer any loss of ultimate compressive strength. One explanation for the higher than expected compressive strength measured for BK092013-4-5 is the unusual break pattern shown in figure 48 (horizontal/vertical/horizontal) that may have resulted in additional force-carrying capability (code R in figure 45).

5.7.3 Double Drops from 21″–27″

Because the laboratory dropped-weight impacts were performed multiple times without producing visible damage to the impacted surface, a third set of test specimens (2-CAI-1–2-CAI-5) were impacted twice from different drop heights to increase the internal damage/underside surface cracks without producing visible damage to the impacted surface. After each ASTM D7136 test impact, the test specimen was analyzed for internal damage using the ultrasonic C-scan (amplitude and TOF) analysis techniques. After the second impact/C-scan analysis sequence was completed, the ultimate compressive strength of the twice-impacted test specimen was determined using ASTM D7137.

As listed in figure 49, the ultimate compressive strengths of the baseline test specimens were equal to or greater than 38.2 ksi. To allow the levels of internal damage produced by the first and second impacts to be compared more easily, the underside C-scan amplitude images and the impacted side C-scan TOF images produced by the first and second impacts were placed side-by-side for each test specimen. The C-scans and CAI data for test specimens, 2-CAI-1–2-CAI-5, were arranged by decreasing ultimate compressive strengths, as shown in figures 54–56.

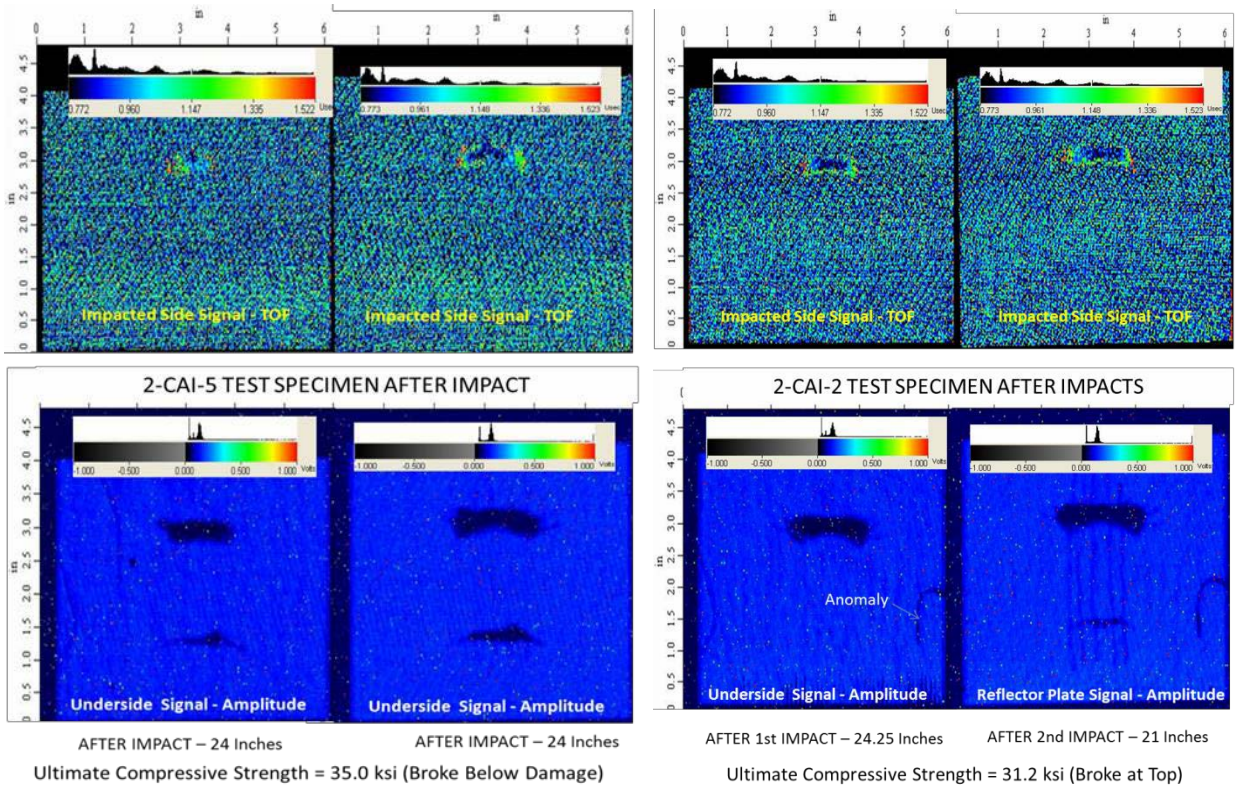

Figure 54. C-scans (amplitude and TOF) and CAI test data for twice-impacted test specimens 2-CAI-5 and 2-CAI-2 with epoxy-coated underside

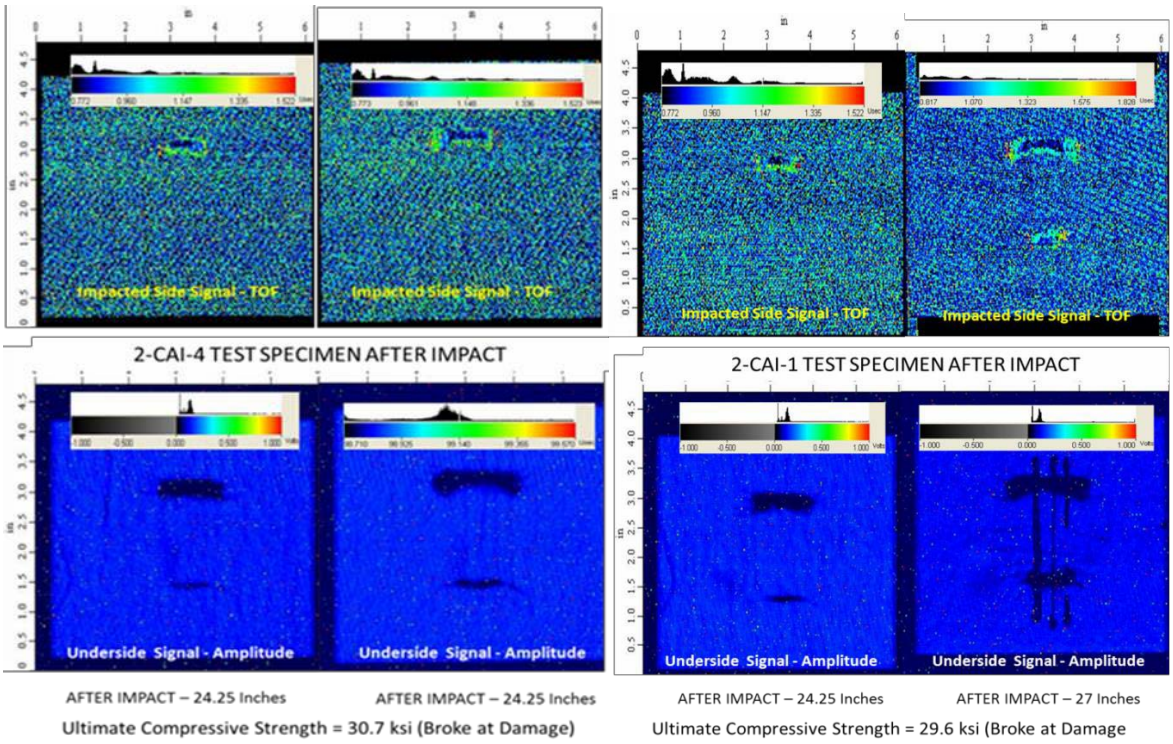

Figure 55. C-scans (amplitude and TOF) and CAI test data for twice-impacted test specimens 2-CAI-4 and 2-CAI-1 with epoxy-coated underside

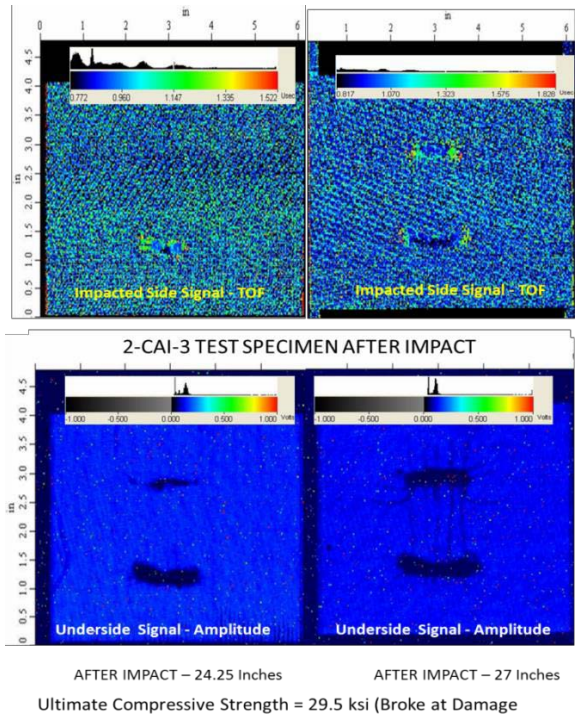

Figure 56. C-scans (amplitude and TOF) and CAI test data for twice-impacted test specimen 2-CAI-3 with epoxy-coated underside

As shown in figures 54–56, the amplitude and TOF C-scan images after the first impact (drop height: 24.25″) are very similar to test specimens 2-CAI-1–2-CAI-5 (i.e., the amplitude [underside] and TOF [impacted side] images both contain one major area of internal damage). The amplitude and TOF C-scan images contain an increase in the initial internal damage for all test specimens after the second impacts, with drop heights of 21″ and 24.25″ (i.e., initial area of damage increases in size/depth with the second impact), respectively. For the second impacts performed with the 27″ drop height, a second area of damage was produced in addition to the initial area of damage increasing in size and depth.

Regardless of the drop height of the second impact, the ultimate compressive strengths determined for the twice-impacted test specimens, 2-CAI-1–2-CAI-5 (see figures 54–56), were well below those of the once-impacted test specimens, 1-CAI-2–1-CAI-5 (see figures 49 and 50). Based on the 38.2 ksi ultimate compressive strength of the baseline samples, once-impacted test specimens 1-CAI-4 and 1-CAI-5 and twice-impacted specimens 2-CAI-2 and 2-CAI-4 (both sets of impacted test specimens with one main area of damage) suffered 4%–5% and 18%–20% losses of ultimate compressive strength, respectively. The once-impacted test specimens 1-CAI-2 and 1-CAI-3 and the twice-impacted specimens 2-CAI-1 and 2-CAI-3 (both sets of impacted specimens with two areas of damage) suffered 9%–16% and 22%–23% losses, respectively. Twice-impacted test specimen 2-CAI-5, which had one area of damage and broke well below the damaged area (see figure 48), had an 8% loss of ultimate compressive strength.

Consequently, these results indicate that the second ASTM D7136 impacts increased the internal

damage and decreased the ASTM D7137 ultimate compressive strengths of all of the test specimens without producing visible damage in the impacted surfaces.

5.8 COMPARISON OF CONDUCTIVE LINE CRACKS AND CAI TEST RESULTS

During the laboratory dropped-weight impact tests, the underside surface cracks increased the resistances of the conductive lines formed with silver epoxy (spatula used to spread line across surface in figure 31) and drawn with silver acrylate (original and fast dry circuit writer pens used to draw lines in figure 35) from below 40Ω to more than 6MΩ. The increased conductive line resistances exceeded by orders of magnitude the 10K Ω resistance required to make 125 KHz SMART Crack sensors permanently readable, as shown in table 6 (i.e., a readable sensor indicates the presence of a surface crack and, consequently, significant internal damage).

To determine if similar conductive line resistance increases would be obtained with the ASTM D7136 impact test specimens, silver epoxy adhesive and silver acrylate conductive lines were drawn on the epoxy-coated underside surfaces of the test specimens. The crack detection capabilities of the silver epoxy and acrylate conductive lines were evaluated for two different scenarios: detection of crack due to single impact (once-impacted test specimens BK092013-4-4–BK092013-4-6) and detection of surface crack propagation due to additional impacts (twice-impacted test specimens 2-CAI-1–2-CAI-5).

In contrast to the smeared lines in figure 31, the silver epoxy adhesive was loaded into the barrel of a Nordson EFD Optimum System (Model: Performus III) and dispensed through a 1.6-mm tip using air pressure (manual dispenser also available) onto the underside surfaces of the ASTM D7136 test specimens. The applied silver epoxy adhesive lines were used as dispensed (circular bead with a 1.6-mm cross-section) or were smoothed/reduced to a height less than 0.3 mm prior to curing overnight at room temperature. The smooth silver epoxy line was produced by placing tape on each side of the epoxy bead and drawing down the epoxy with a razor blade. When the tape was removed, the height of the resulting epoxy line was in the range of 0.05–0.22 mm (controlled by the thickness of the tape [2–9 mil]). Examples of the epoxy lines are shown on test specimen BK092013-4-4 in figure 48: “as dispensed” and “smoothed (0.1 mm height).” Conductive lines were not drawn with the silver epoxy ink because of the elevated curing temperatures required and the additional application concerns associated with solvent release as the ink cured.

To evaluate their single-impact crack detection capabilities, silver acrylate lines were drawn onto ASTM D7136 test specimens BK092013-4-4 (21″ drop height) and BK092013-4-6 (24″ drop height) and the silver epoxy lines were drawn (as dispensed and smoothed line) onto the ASTM D7136 test specimen BK092013-4-5 (27″ drop height). The silver epoxy lines are visible in the underside C-scan amplitude image in figure 53: two lines extend across the areas of detected internal damage and the two cracks on the underside surface of BK092013-4-5. The silver acrylate lines (original circuit writer) drawn onto the underside surface of the once-impacted test specimen BK092013-4-6 cross a single crack (corresponding with the area of damage detected by the C-scan images in figure 52), as shown on the right side of figure 57.

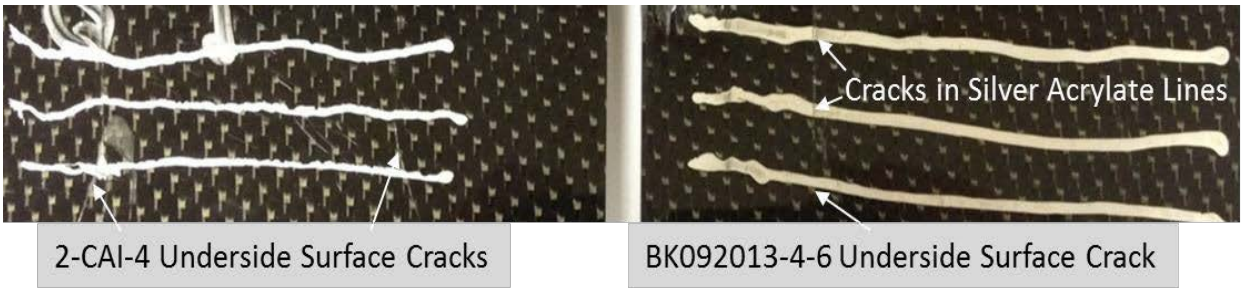

Figure 57. Photographs of ASTM D7136 test specimens 2-CAI-4 and BK092013-4-6 with silver acrylate lines

Regardless of the drop height (21″–27″) or the conductive line composition (silver epoxy vs. silver acrylate) used for the impact tests, the surface crack produced by the initial impact caused the resistance of the affected line to increase from less than 20Ω to more than 6MΩ (an attached SMART sensor would become permanently readable, indicating the presence of internal damage).

Though the laboratory dropped-weight tests used multiple impacts to produce cracks in the underside surface and conductive lines, the resistances of the lines were checked after each impact to detect original crack formation, not propagation of existing cracks. To evaluate the surface crack propagation detection capabilities of the silver conductive lines, the ASTM D7136 test specimens 2-CAI-1–2-CAI-5 were impacted using a 24″ drop height prior to application of the silver conductive lines. The C-scan images of the internal damage created by the 24″ drop impacts are shown in figures 54–56 and correspond with the underside cracks of the impacted test specimens. The silver acrylate and epoxy adhesive lines were then drawn across both the middle and ends of the underside cracks. The test specimens were then impacted a second time using 21″–27″ drop heights to increase the internal damage of the test specimens, causing a lengthening/widening of the surface cracks. The second impacts (24″ drop height) to test specimens 2-CAI-5 (see figure 59) and 2-CAI-4 (see figure 57)—which produced additional internal damage/increased surface cracks—did not cause any silver acrylate line resistance increases on 2-CAI-4 and increased the resistance of only one of the lines on 2-CAI-5 (see figure 48). In contrast to the silver acrylate lines, the additional internal damage/surface cracks caused resistance increases in all of the silver epoxy adhesive lines on 2-CAI-1 and 2-CAI-3.

These results indicate that either silver acrylate or epoxy adhesive conductive lines are well suited for detecting the initial formation of underside surface cracks in ASTM D7136 impacted test specimens. Whether it is the higher viscosity (bridges do not fill cracks) during application or lack of flexibility once cured, these initial results indicate that the silver epoxy adhesive lines are better suited than the silver acrylate lines for monitoring underside crack propagation caused by additional impacts/increased internal damage.

5.9 SUMMARY

The ASTM D7136/D7137 (CAI) tests performed in Task 5 demonstrated that aerospace composite test specimens (eight plies of AGP370-5HS with 8552 epoxy resin) could suffer

significant internal damage and loss of compression strength without visible impacted surface damage. The significant internal damage was produced using a 5.6-lb projectile with a flat end dropped from 21″–27″, achieving impact velocities of 98–116 in/sec (5.6–6.6 Mi per hour) and measured impact energies of 7.9–11.2 J. As opposed to the impacted surface (below BVD marks), the underside surface contained 1–2 cracks originating from the internal damage.

The internal damage was fully characterized by ultrasonic C-scans (amplitude and TOF) and high magnification photography of sample cross-sections. The loss of compressive strength measured with ASTM D7137 was loosely proportional to the level of internal damage determined by the analytical techniques for the first impacts. The loss of compressive strength became much more significant with the second impacts. Conductive lines of silver epoxy adhesive (epoxy ink was not tested because of the heated cure requirement) applied to the nonconductive (epoxy coating) underside surfaces successfully detected (resistances increased from less than 100Ω to more than 100KΩ) both the initiation as well as the propagation of the surface cracks originating from the internal damage. Silver acrylate inks (water-based and solvent-based) drawn on the nonconductive underside reliably detected only the initiation of the surface cracks.

Even though the test specimens were held stationary during the impact tests, 50 and 100 g ball-spring accelerometers attached to the specimen underside surfaces by double-stick tape were activated by the impacts that caused internal damage (accelerometers activated by impact shock waves).

The research performed in Tasks 4 and 5 indicate that both SMART Crack and impact sensors could be used by maintenance personnel to identify composite structures that had experienced significant impact/presence of resulting internal damage even though the exterior surfaces had no visible damage. If silver epoxy adhesive conductive lines are employed in the crack sensors, the research indicates the sensors could be used to detect surface crack propagation and crack initiation. When the SMART sensors incorporate a 125 KHz RFID tag, the impact-activated tag can be read directly through the composite skin—allowing initial (surface crack)/additional (crack propagation) damage detection to occur from outside the aircraft.

6. TASK 6: EVALUATION OF SMART SENSORS: FATIGUE TESTING

6.1 INTRODUCTION

In addition to the detection of interior surface cracks resulting from impacts in Tasks 4 and 5, research was also performed to evaluate the capabilities of the silver epoxy and acrylate lines to detect surface changes resulting from different fatigue failure modes. The fatigue failure test used in this project was similar to ASTM D3749 “Standard Test Method for Tension—Tension Fatigue of Polymer Matrix Composite Materials.” Two different sets of ASTM test specimens with drilled centered holes were fatigued to create interior/surface delaminations. The first set of fatigue test specimens were produced in the manner described in ASTM D5766/D5766M “Open-Hole Tensile Strength of Polymer Matrix Composite Laminates” and were tested with the drilled hole empty (open). The second set of test specimens were produced as described in ASTM D6742-12 (“Filled-Hole Tension and Compression Testing of Polymer Matrix Composite Laminates”), and bolts were inserted into the drilled holes (filled) and tightened with different

levels of torque prior to testing.

6.2 TENSION-TENSION FATIGUE FAILURE TEST SETUP

As an initial evaluation of the fatigue failure test setup, four fatigue test specimens previously fabricated by UDRI for the National Aeronautics and Space Administration (NASA) Intelligent Engine Program [5] were used. The test specimens were made using a T700SC 12K non-crimp fabric with a real weight of 750 grams per square meter and Cycom 5208 epoxy resin. Each test specimen was constructed with attached grips, a 0.25″ hole drilled at the center point, an insulating epoxy coating, and a nanoink (CNF/epoxy) conductive line connected to two copper tabs to make resistance readings, as shown in figure 58.

Figure 58. Fatigue test specimens with drilled hole (0.25″) and conductive lines (nanoink and silver acrylate)

For this project, two sets of silver conductive lines (attached to copper tabs with silver epoxy adhesive for resistance measurements) were drawn on the epoxy-coated surface so that one conductive line partially circumvented the drilled hole and the other conductive line ran along the outer edge of the test specimen, as shown in figure 58. If cracks originated from the hole during the fatigue test (expected mechanism), the resistance of the line circumventing the hole would increase first.

The test frame used to fatigue the test specimens was a MTS 22 kilopound-force (kip) frame with a 3.3 kip servo-hydraulic actuator, a calibrated Linear Variable Differential Transformer, and a 5 kip load cell. The test machine was controlled with an MTS 458 servo-hydraulic controller. A precision multimeter was used to periodically measure the resistances of the conductive lines. Hydraulic grips of 22 kip capacity were used to support the test specimen, as shown in figure 59. The obtained test data are listed in table 8.

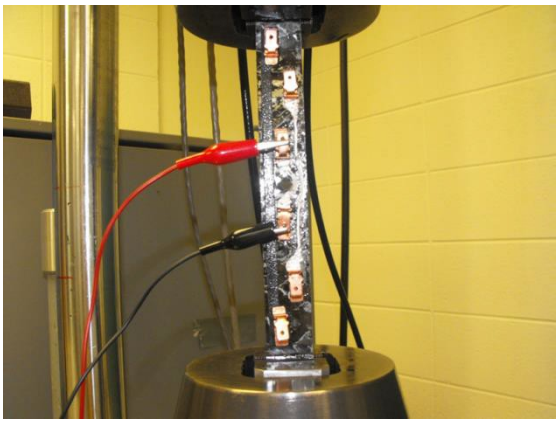
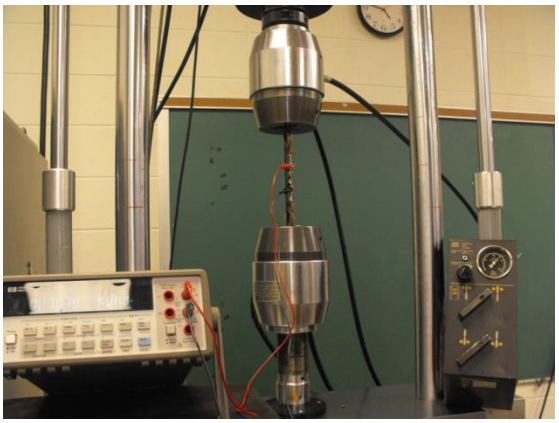

Figure 59. Tension-tension failure test rig and supported test specimen with a conductive line connected to the resistance meter

Table 8. Tension-tension fatigue test data

Composite Micro-Crack Fatigue							
Specimen I.D.	Date	Resistance (ohms) Location 1 Hole	Resistance (ohms) Location 2	Cycles	Frequency Hz	Loading (lbs.)	
						Min	Max
STL 282-1	15-Nov-13	7,200	580,000	0	5	117	1,170
STL 282-1	15-Nov-13	7,200	580,000	5447	5	117	1,170
STL 282-1	15-Nov-13	Open/Failed	Open/Failed	5447	5	117	1,170
STL 282-2	15-Nov-13	1.365	1.212	0	5	57.4	574
STL 282-2	15-Nov-13	1.500	1.548	20,000	5	57.4	574
STL 282-2	15-Nov-13	1.608	1.616	40,000	5	57.4	574
STL 282-2	15-Nov-13	1.700	1.632	60,000	5	57.4	574
STL 282-2	15-Nov-13	1.589	1.74	80,000	5	57.4	574
STL 282-2	15-Nov-13	1.590	2.266	100,000	5	57.4	574
STL 282-2	18-Nov-13	1.531	1.374	120,000	5	57.4	574
STL 282-2	18-Nov-13	28.9	1,100,000	140,000	5	117	1,170
STL 282-2	18-Nov-13	21.73	Open	160,000	5	117	1,170
STL 282-2	18-Nov-13	21.73	Open	180,000	5	117	1,170
STL 282-2	18-Nov-13	Open/Failed	Open/Failed	194,930	5	117	1,170
S1L282-4	19-Nov-13	40,269	7.596	0	5	57.4	574
5TL282-4	19-Nov-13	39,424	7.287	20,000	5	57.4	574
STL282-4	19-Nov-13	39,304	7.209	40,000	5	57.4	574
STL282-4	20-Nov-13	Open/Failed	Open/Failed	40,297	5	57.4	574

Initial tension-tension testing (test specimen STL 282-3) using loads of 117 lb and 1170 lb at a cycle rate of 5 Hz caused the test specimen to fail in approximately 100,000 cycles. Two conductive lines were then drawn on the epoxy-coated surface of a second test specimen (STL 282-1 in table 8) with silver acrylate ink (circuit writer fast dry; higher resistances because of poor coverage on the rough surface). The data show that the resistances (no load) of the silver acrylate lines did not increase until the specimen broke at the hole/surrounding surface at 5447 cycles. Test specimen STL 282-4 with silver acrylate lines (original circuit writer) drawn on its surface was cycled between reduced loads of 57.4 lb and 574 lb in an effort to obtain more cycles prior to failure. Though the test specimen did not fail until 40,297 cycles, the resistances

of the silver acrylate lines were essentially unchanged just prior to failure. Consequently, the conductive silver acrylic ink lines have minimal predictive capabilities with respect to fatigue failure.

Because the silver acrylic ink lines appeared poorly suited for detecting fatigue, two silver epoxy conductive lines were applied to the epoxy-coated surface of a fourth test specimen (STL 282-2) using the two different techniques (described in detail in section 5.8) for the impact test specimens in figure 48. The silver epoxy adhesive was dispensed (Nordson EFD Optimum System Performus III, 1.6 mm tip, air pressure) so that one bead partially circumvented the drilled hole and the other bead ran along the outer edge of the test specimen (locations similar to acrylic lines in figure 58). The applied silver epoxy adhesive bead along the edge of the test specimen line was used as dispensed (circular bead with a 1.6 mm cross-section), and the bead partially circumventing the drilled hole was smoothed/reduced to a height less than 0.3 mm (using a notched razor blade). Copper tabs were applied to the ends of the silver epoxy beads for making resistance measurements. The conductive silver epoxy lines on the failed test specimen are shown in figure 60.

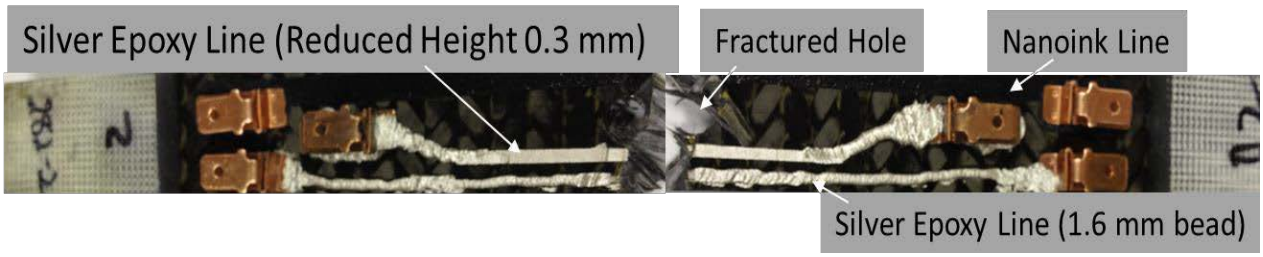

Figure 60. Failed fatigue test specimen with silver epoxy adhesive conductive lines and copper tabs

After the test specimen with the two silver epoxy adhesive conductive lines was cycled between loads of 57.4 lb and 574 lb for 120,000 cycles, the test specimen was intact and the resistances of the conductive lines remained below 2Ω (see table 8). When 20,000 additional cycles were performed with increased loads of 117 lb and 1170 lb, the resistance (no load) of the epoxy line (bead) along the edge increased dramatically (>1MΩ), but the smoothed line circumventing the hole increased only slightly in resistance (1.5Ω up to 20–30Ω). Prior to specimen failure at 194,930 cycles, the conductive line along the edge became electrically open (>6MΩ) and the line circumventing the hole remained below 30Ω—representing the concept that the silver epoxy lines were rugged under normal loads but underwent a permanent resistance change (no load) at loads capable of causing fatigue failure.

For all four fatigue samples, the resistances of the nanoink lines remained constant up to failure regardless of the cyclic loads or number of cycles (i.e., in agreement with Task 2, the nanoink lines are very durable and would require an RFID system with logging capability for detecting surface cracks that form only under load [figure 13]).

For the two fatigue samples tested with the silver acrylate conductive lines, the conductive lines failed (opened) simultaneously with the specimen failure, indicating that the capability of the acrylic conductive lines to detect surface cracks/deformation prior to specimen failure is poor

(i.e., the fatigue life of the silver acrylate conductive line was equal to/greater than the fatigue life of the monitored composite material).

For the fatigue sample tested with silver epoxy adhesive conductive lines, the cycled conductive lines were stable at the lower loads but started to degrade rapidly with the increased loads, quickly leading to specimen failure (i.e., silver epoxy lines are durable and have the potential for detecting imminent test specimen failure).

6.3 TENSION-TENSION FATIGUE FAILURE TEST: OPEN-HOLE

To determine if the excessive load/imminent failure prediction capabilities of the silver epoxy lines in table 8 and figure 61 were reproducible and dependent on the conductive line application method (bead vs. smoothed) and location (edge vs. drilled hole), another set of open-hole test specimens (ASTM D5766/D5766M) were fabricated using a unitape roll of BMS 8-276N Toray Epoxy Prepreg T800SC-24000-10E P235W-19 (Date of Manufacture 7/16/08). One surface of each test specimen was coated with a room-temperature setting, nonconductive epoxy. After curing, each cured epoxy-coated specimen was drilled (0.25″ hole) and one continuous silver epoxy line (dispensed bead, smoothed bead, or smeared with spatula) was applied so that it covered both edges and partially circumvented the drilled hole, as shown in figure 61.

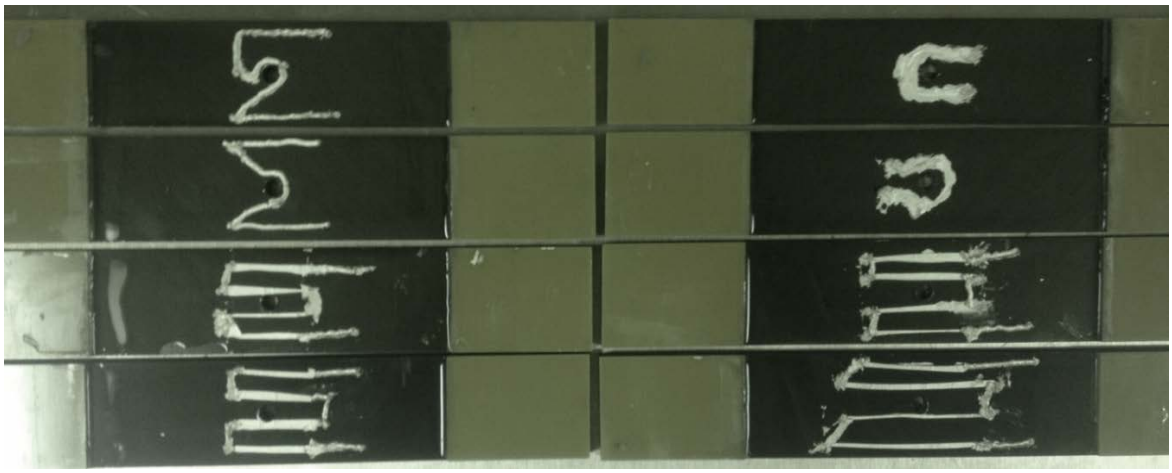

Figure 61. Open-hole tension—tension test specimens with different types of silver epoxy adhesive conductive lines

The failure loads of two test specimens were determined to be 20,729 lb and 21,845 lb using ASTM D5766/D5766M “Open-Hole Tensile Strength of Polymer Matrix Composite Laminates.”

For the first open-hole fatigue test specimen, the conductive silver epoxy line was applied as a bead and 12,000 lb and 1,200 lb loads (60% and 6%, respectively, of expected failure load) were used to initialize the tension-tension fatigue test. The tension-tension loads were increased every 100,000 cycles up to 80% (17,000 lb and 7,000 lb) of the expected failure load. The minimum/maximum loads, the maximum load displacement (ΔS), and the measured resistance (no load) for each set of cycles are listed in table 9 for the tension-tension fatigue failure test of specimen OHF-5.

Table 9. Tension-tension fatigue test data for open-hole test specimen OHF-5 with a silver epoxy bead conductive line

Load (lbs)			ΔS		Resistance in ohms	
Minimum	Maximum	Date	Inches	Cycles	No Load	
1,200	12,000	2-Jul-14	0.048	5,000	0.9	
				10,000	0.9	
				15,000	0.8	
				20,000	0.8	
				30,000	0.8	
				50,000	0.9	
		3-Jul-14		70,000	0.8	
				90,000	0.8	
				100,000	0.8	
1,500	15,000		0.06	110,000	0.8	
		7-Jul-14	0.057	130,000	0.8	
				150,000	0.9	
				170,000	0.8	
				190,000	0.9	
				200,000	0.9	
1,700	17,000		0.066	210,000	0.9	
		8-Jul-14		230,000	0.9	
Outer leg of trace fell off composite				250,000	Open (>6 M Ω)	
				270,000	0.5	(Remaining Trace)
				290,000	0.5	

Though the specimen was undergoing 50–60 mil displacement at the maximum load of each cycle, the test data in table 9 demonstrate that both the test specimen and conductive line remained intact for 200,000 cycles at tension-tension loads up to 70% of the expected maximum load. After 50,000 additional cycles at 80% of the failure load, the portion of the epoxy line along the one edge fell off (circuit open). Though there were a few cracks/delaminations visible in the epoxy coating (see figure 62), the remaining conductive line remained intact (resistance below 1Ω) up to 300,000 total cycles.

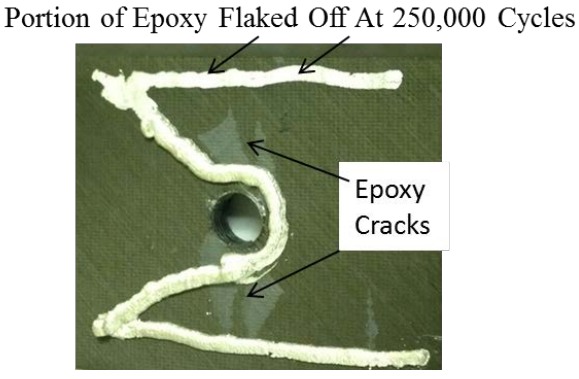

Figure 62. Fatigued open-hole test specimen OHF-5 with cracked epoxy coating and silver epoxy bead

For the second open-hole fatigue failure test specimen, the conductive silver epoxy line was applied as a bead then smoothed with a razor blade. Again, 12,000 lb and 1,200 lb loads (60% and 6% of expected failure load, respectively) were used to initialize the tension-tension fatigue test. The tension-tension loads were increased every 100,000 cycles up to 90% (19,000 lb) of the expected failure load. The minimum/maximum loads, the specimen displacement (ΔS) at the maximum load, and the measured resistances (no load and at minimum load) for each set of cycles are listed in table 10 for the tension-tension fatigue failure test of specimen OHF-10.

Table 10. Tension-tension fatigue test data for open-hole test specimen OHF-10 with a smoothed silver epoxy conductive line

Load (lbs)			ΔS		Resistance in ohms		
Minimum	Maximum	Date	Inches	Cycles	No Load	Minimum Load	
1,200	12,000	9-Jul-14	0.049	20,000	2.7	3.3	
				40,000	3.6	4.6	
				60,000	3.7	5.2	
Epoxy showing hairline cracks				80,000	3.6	5.4	
		10-Jul-14		100,000	3.6	6.2	
1,500	15,000	11-Jul-14	0.062	120,000	3.6	9.3	
				140,000	3.6	14	
		14-Jul-14		160,000	3.5	16.3	
				180,000	3.5	500	
				200,000	3.2	776	
1,700	17,000	15-Jul-14	0.071	220,000	3.6	Open	(Ag crack – left side of hole edge)
				C-scan Taken			
		23-Jul-14	0.0745	240,000	3.4	Open	
				260,000	3.5	Open	
		24-Jul-14		280,000	3.5	Open	
				300,000	3.6	Open	
1,900	19,000		0.0744	320,000	3.5	Open	
		28-Jul-14	340,000	Thicker area along edge - broke off			
				360,000	3.8	Open	
				380,000	3.6	Open	

Though the specimen was undergoing 50–60 mil displacements at the maximum load of each cycle, the test data in table 10 demonstrate that both the test specimen and conductive line remained intact for 200,000 cycles at tension-tension loads up to 70% (15,000 lb) of the expected failure load. However, there were several cracks/delaminations in the epoxy coating (see figure 63).

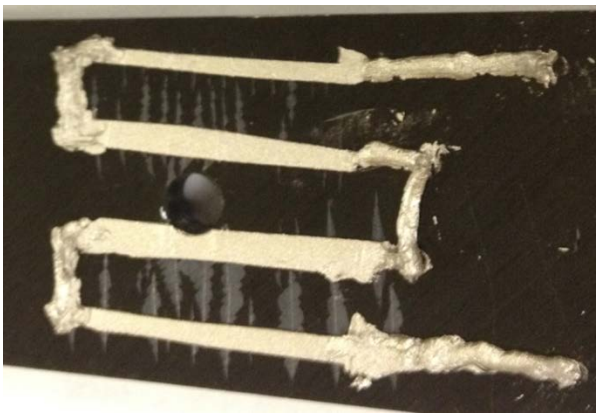

Figure 63. Fatigued open-hole test specimen OHF-10 with cracked epoxy coating and smoothed conductive lines

Though the test specimen experienced a total of 400,000 cycles at tension-tension loads up to 90% of the expected failure load, the test specimen remained intact and the smoothed silver epoxy line also appeared to be intact. However, when the resistance of the conductive line was measured at the minimum load, the resistance increased rapidly/opened when the test specimen was cycled at 80% of the expected failure load. Though the minimally loaded conductive line remained electrically open during the cycles at 80% and 90% of the failure load, the resistance of the unloaded conductive line remained below 5Ω for the entire test (i.e., the crack in the line at the minimum load was closing when the load was removed).

For the third open-hole fatigue failure test specimen, the conductive silver epoxy line was smeared onto the epoxy-coated surface using a spatula. In addition to the epoxy-coated side, a transparent polyester tape with an acrylic adhesive (3M 853, 2.2 mil thickness, -60°–300°F adhesive) was applied over the hole on the other side of the test specimen and a line of silver epoxy was applied to the polyester surface with a spatula. Again, 12,000 lb and 1,200 lb loads (60% and 6%, respectively, of the failure load) were used to initialize the tension-tension fatigue test. The tension-tension loads were increased every 100,000 cycles up to 80% (19,000 lb and 9,000 lb) of the expected failure load. The minimum/maximum loads, the specimen displacement (ΔS) at the maximum load, and the measured resistances for the two silver epoxy lines on the epoxy and tape-covered surfaces (without a load and at minimum load) for each set of cycles are listed in table 11 for the tension-tension fatigue failure test of specimen OHF-11.

Table 11. Tension-tension fatigue test data for open-hole test specimen OHF-11 with smeared silver epoxy conductive lines

Load (lbs)			ΔS		Resistance in Ohms			
					Front (Epoxy)		Back (Tape)	
Minimum	Maximum	Date	Inches	Cycles	No Load		No Load	Mean Load
1,200	12,000	15-Jul-14	0.049	20,000	23	40	1.3	633
		16-Jul-14		40,000	30	70	1.7	54
				60,000	38	105	1.7	440
Epoxy showing hairline cracks			0.5	80,000	46	101	1.4	2560
				100,000	52	143	1.4	3059
1,500	15,000	17-Jul-14	0.062	120,000	64	160	1.6	Open
			0.063	140,000	75	238	1.7	Open
				160,000	73	247	1.7	Open
				180,000	84	1,368	1.7	Open
				200,000	91	755	1.7	Open
1,700	17,000	21-Jul-14	0.071	220,000	141	345	1.8	Open
				240,000	134	820	Edge Flaked off	Open
			0.0715	260,000	142	242	Remaining Trace	
				280,000	157	Open	2.4	56K
				C-scan	Ag crack upper right near hole		2.1	100K
		25-Aug-14	0.655	300,000	1,177	Open	1.5	Open
1,900	19,000	27-Aug-14	0.0735	320,000	1,400	Open	2.6	Open
		22-Sep-14	0.0875	340,000	1,240	57K	3.4	Open
			0.0865	360,000	16K	54K	2.1	Open
			0.0955	380,000	43K	Open	4.6	Open
			0.0852	400,000	39K	Open	4.5	Open

The loaded/unloaded resistances of the uneven lines applied with the spatula on the epoxy-coated surface slowly increased with fatigue cycling regardless of the applied load cycle. Though the unloaded line resistance increased with cycling and cracks/delaminations were present in the epoxy coating, the unloaded resistance was still under 200Ω at 80% of the expected failure load. The loaded line opened electrically after 280,000 total cycles (80,000 cycles at 80% of the failure load). In contrast to the epoxy surface lines, the minimally loaded epoxy lines on the polyester tape opened electrically at 120,000 cycles (70% failure load). The unloaded resistance of the line on the tape was unchanged (<2Ω) until 240,000 cycles (40,000 cycles at 80% failure load), at which time a portion of the line fell off. Similar to figure 63, the silver line fell off along the edge of the taped test specimen and not at the drilled hole, as shown in figure 64.

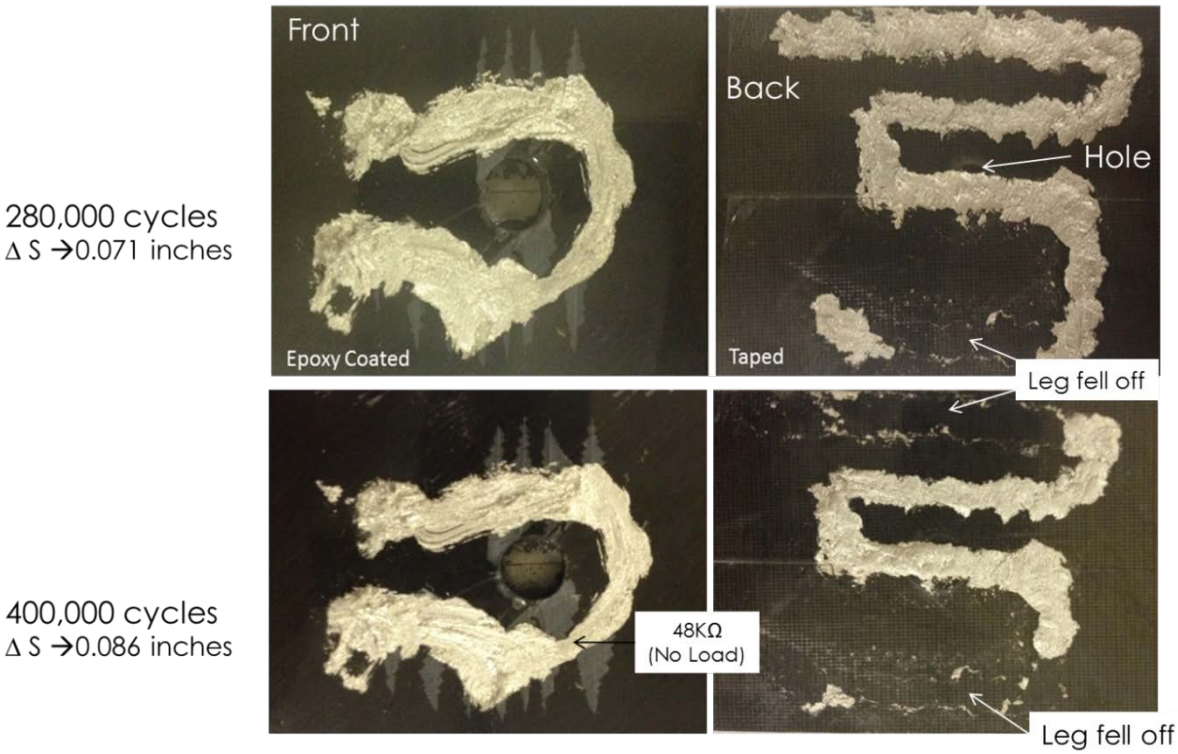

Figure 64. Fatigued open-hole test specimen OHF-11 smeared silver epoxy lines on cracked epoxy coating and polyester tape

To determine if the unloaded resistance measurements would continue to increase for the silver epoxy line on the epoxy-coated surface at higher loads, the applied load cycle was increased to 90% of the failure load for the OHF-11 test specimen. The unloaded resistances of the silver epoxy line immediately increased tenfold. The unloaded resistances increased further to more than 40KΩ as the displacement exceeded 90 mil with continued cycling at 90% load (>10KΩ, sufficient to activate SMART Crack sensor). The loaded resistances were primarily open during the extended cycling (under load, a crack became apparent near the drilled hole as shown in figure 64). In contrast to the epoxy surface line (on center of the test specimen), additional portions of the taped surface conductive line fell off along the edges of the test specimen. The taped surface conductive line in the center of the specimen/on hole remained intact with the continued cycling (unloaded resistance below 5Ω).

6.4 TENSION-TENSION FATIGUE FAILURE TEST: FILLED HOLE

In addition to the open-hole fatigue test specimens, a second set of test specimens was produced, as described in ASTM D6742-12 “Filled-Hole Tension and Compression Testing of Polymer Matrix Composite Laminates.” The test specimens were fabricated using plies of AGP370-5HS and 8552 epoxy resin. One surface of each test specimen was coated with a room-temperature setting, nonconductive epoxy. The cured epoxy-coated specimens were drilled (0.25″ hole) and one continuous silver epoxy line (dispensed bead, smoothed bead, or smeared with spatula) was applied so that it covered both edges and partially circumvented the drilled hole of each test specimen, as shown in figure 65.

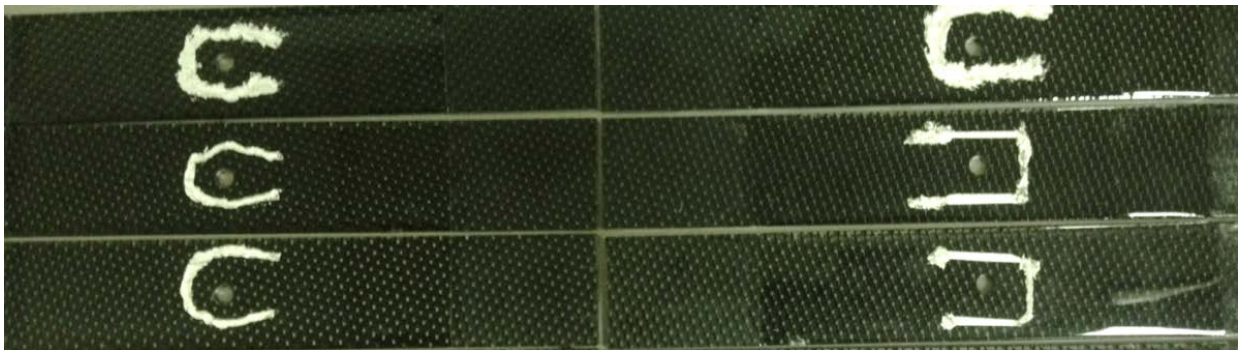

Figure 65. Filled hole tension-tension test specimens with different types of silver epoxy adhesive conductive lines

Bolts were inserted into the drilled holes and tightened with different levels of torque prior to ASTM D6472 failure load testing to determine the effects of bolt torque on the strength of the test specimens. The failure load of a test specimen with a finger-tightened bolt was determined to be 10,573 lb, and a test specimen with an over-torqued bolt (18 ft lb, bolt-stripped at 20 ft lb) was reduced to 8,239 lb.

For the first filled-hole fatigue test specimen, the conductive silver epoxy line was applied as a bead, the bolt was torqued to 17 ft lb, and load cycles of 5000 lb and 500 lb loads (50% and 5%, respectively, of the failure load for test specimens with finger-tight bolts) were used to initialize the tension-tension fatigue test. The tension- tension loads were increased every 100,000 cycles up to 75% (7800 lb and 780 lb) of the expected failure load. The minimum/maximum loads, the specimen displacement (ΔS) at the maximum load, and the measured resistance (no load and minimal load) for each set of cycles are listed in table 12 for the tension-tension fatigue failure test of specimen FHF-5.

Table 12. Tension-tension fatigue test data for filled-hole test specimen FHF-5 with silver epoxy bead conductive lines

Load (lbs)			ΔS		Resistance in Ohms	
Minimum	Maximum	Date	Inches	Cycles	No Load	Minimum Load
500	5,000	25-Jul-14	0.026	5,000	0.9	0.9
				10,000	0.9	0.9
				20,000	0.8	0.8
		30-Jul-14	0.027	40,000	1.4	1.4
				60,000	0.9	0.9
		31-Jul-14		80,000	0.8	0.8
				100,000	0.8	0.8
600	6,000		0.03	120,000	1.5	1.5
				140,000	0.8	0.8
			0.03	160,000	0.8	0.8
		14-Aug-14		180,000	0.9	0.9
				200,000	0.8	2.2
700	7,000		0.0345	220,000	0.9	6.1
				240,000	0.9	1.6
Crack in epoxy			0.35	260,000	0.9	13.2
		18-Aug-14		280,000	0.9	5
				300,000	1	2.3
740	7,400		0.0365	320,000	1.1	2.8
		19-Aug-14		340,000	1.7	12
				360,000	1.3	14
			0.036	380,000	1.5	9.8
				400,000	1.4	30
780	7,800	20-Aug-14	0.038	420,000	401,706 cycles – specimen broke in half	

The test data in table 12 demonstrate that both the test specimen and conductive line remained intact for 400,000 cycles at tension-tension loads up to 70% of the expected maximum load. After 2000 additional cycles at 75% of the failure load, the specimen failed, as shown in figure 66.

Figure 66. Filled-hole test specimen FHF-5 with silver epoxy bead conductive line after fatigue failure

As opposed to the open-hole test specimens, only one minor crack was visible in the epoxy coating and the resistance of the conductive line (loaded and unloaded) changed only slightly (resistance below 30Ω) prior to the test specimen failure (i.e., the silver epoxy line did not indicate failure was imminent).

6.5 DAMAGE CHARACTERIZATION OF TENSION-TENSION FATIGUE FAILURE TEST SPECIMENS

Because the silver epoxy lines underwent large changes in resistance/appearance along the edges of the fatigued open-hole test specimens, the fatigued test specimens were analyzed for surface and internal damage. Open-hole test specimens (before, during, and after the fatigue test) were cross-sectioned, polished, and examined under high magnification; analyzed with x-ray CAT, and characterized using ultrasonic C-scan amplitude and TOF analyses. The representative cross-sections of the fatigued open-hole test specimens in figure 67 show that the top and bottom layers of the fatigued specimens had begun to delaminate/separate.

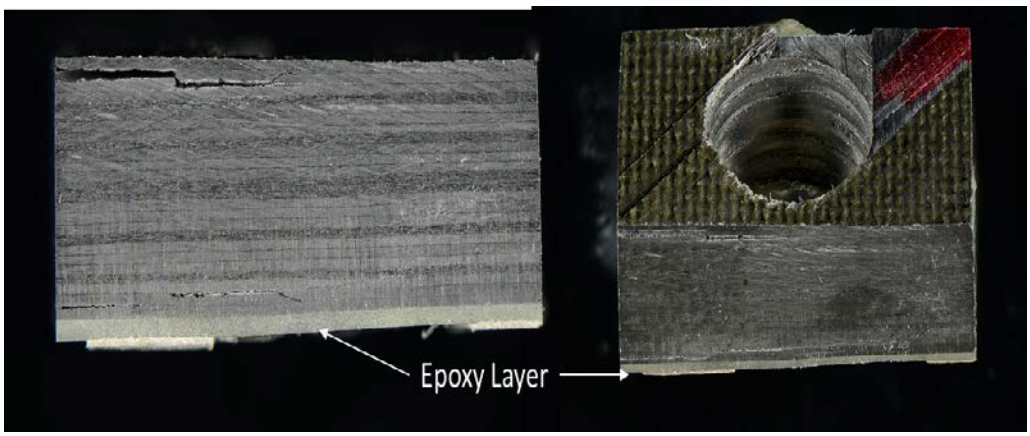

Figure 67. Cross-sectioned composite pieces with upper and lower (epoxy-coated) layers separating after tension-tension fatigue test

A high magnification cross-section of after fatigue test specimen OHF-10 determined that the fatigued composite test specimen had undergone both outer-layer separation and internal damage after 400,000 tension-tension cycles with loads up to 90% of the expected failure load, as shown in figure 68.

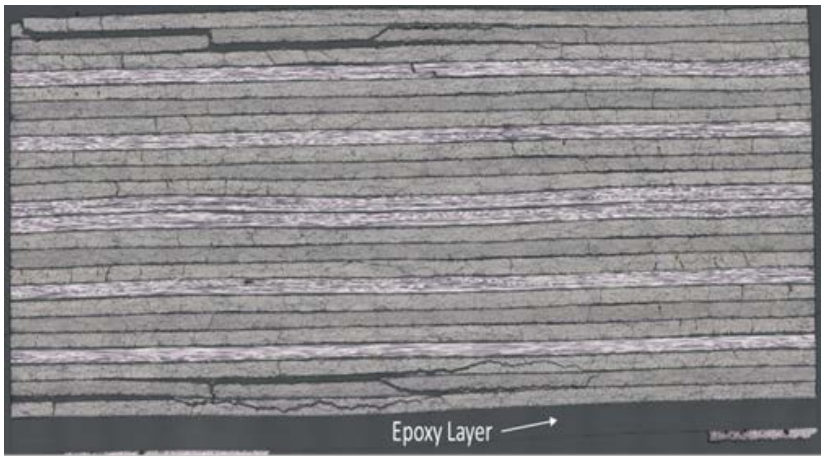

Figure 68. Cross-sectioned composite piece from OHF-10 with widespread internal damage after tension-tension fatigue test

The x-ray CAT side view of OHF-5 showed a large amount of internal damage along with the separation of the upper layer (silver lines on epoxy coating) of the composite after 290,000 total tension-tension cycles (80,000 cycles at 80% of the failure load), as shown in figure 69.

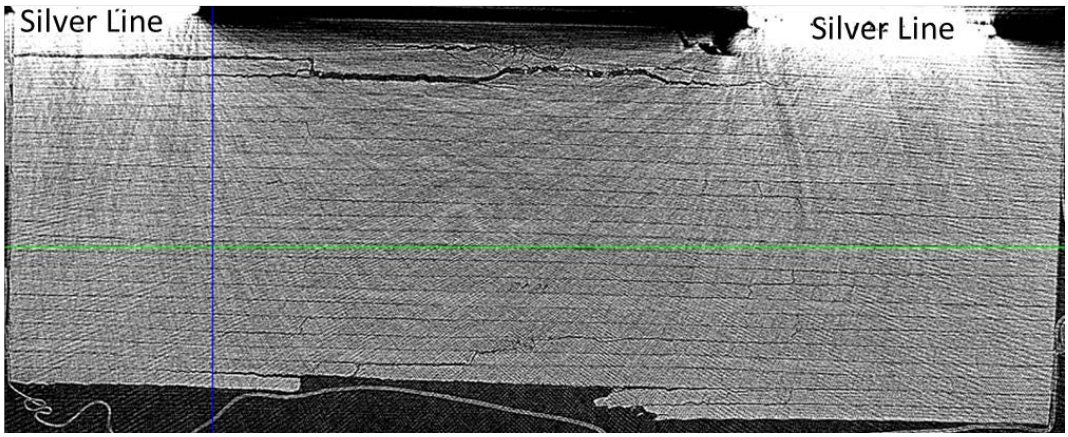

Figure 69. X-ray CAT side view of composite piece from OHF-5 with widespread damage after tension-tension fatigue test

The C-scan amplitude images (before, during, and after fatigue) indicated that composite test specimen OHF-11 had undergone internal damage with the greatest damage/delaminations (areas of bright red) occurring along the edges of the test specimen (in agreement with loss of silver conductive lines along test specimen edges in figures 62, 63, and 64), as shown in figure 70.

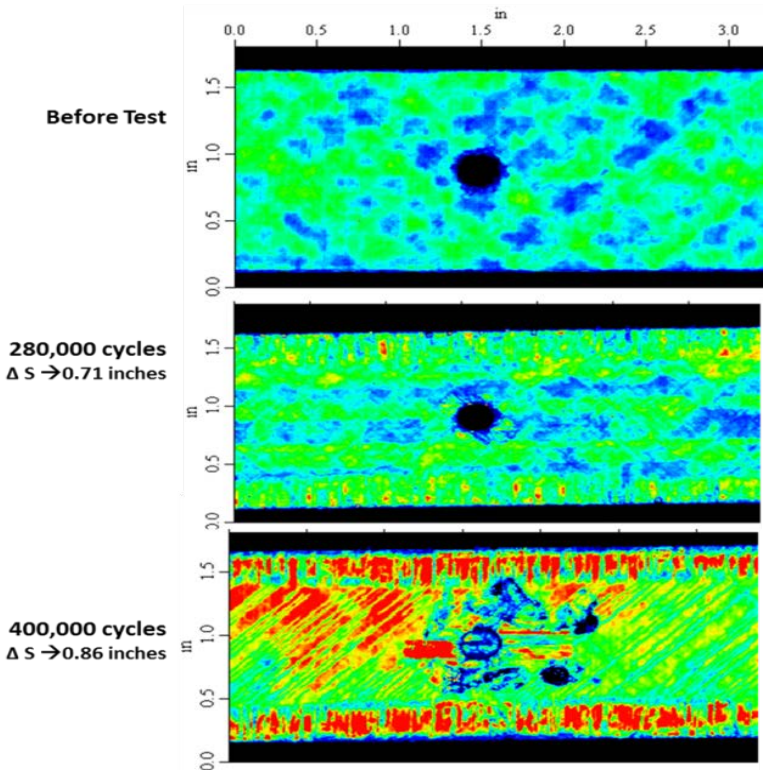

Figure 70. Ultrasonic C-scan amplitude images of OHF-11 test specimen before, during (280,000 cycles), and after tension-tension fatigue test

Because the over-torqued bolt reduced the failure load of the test specimen in table 12 and figure 66, a second test specimen with an over-torqued bolt (prior to epoxy coating) was also examined for internal damage using x-ray CAT analyses as well as ultrasonic C-scan amplitude and TOF analyses. The x-ray CAT images (section includes part of over-torqued [16 ft lb] hole) in figure 71 show that no internal or surface damage was detected, only a small delamination on a cut edge was detected (away from the over-torqued hole).

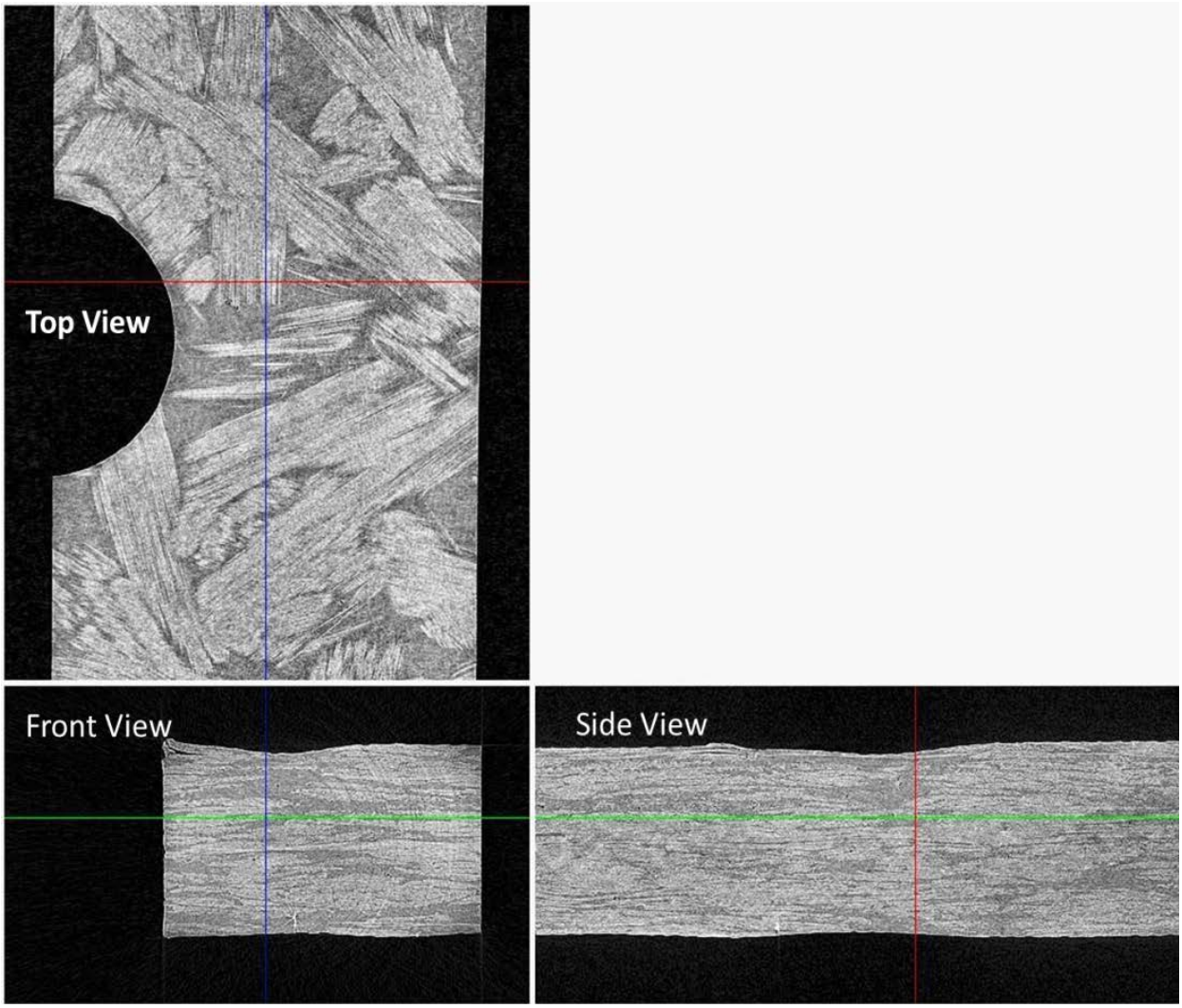

Figure 71. X-ray CAT analysis of non-epoxy-coated composite piece with over-torqued hole

A second composite test specimen was prepared with two drilled holes so that the damage produced by two different levels of bolt over-torque (12 ft lb and 17 ft lb [bolt-stripped]) could be analyzed. As shown by the C-scan amplitude and TOF images in figure 72, no internal damage was detected near either over-torqued hole.

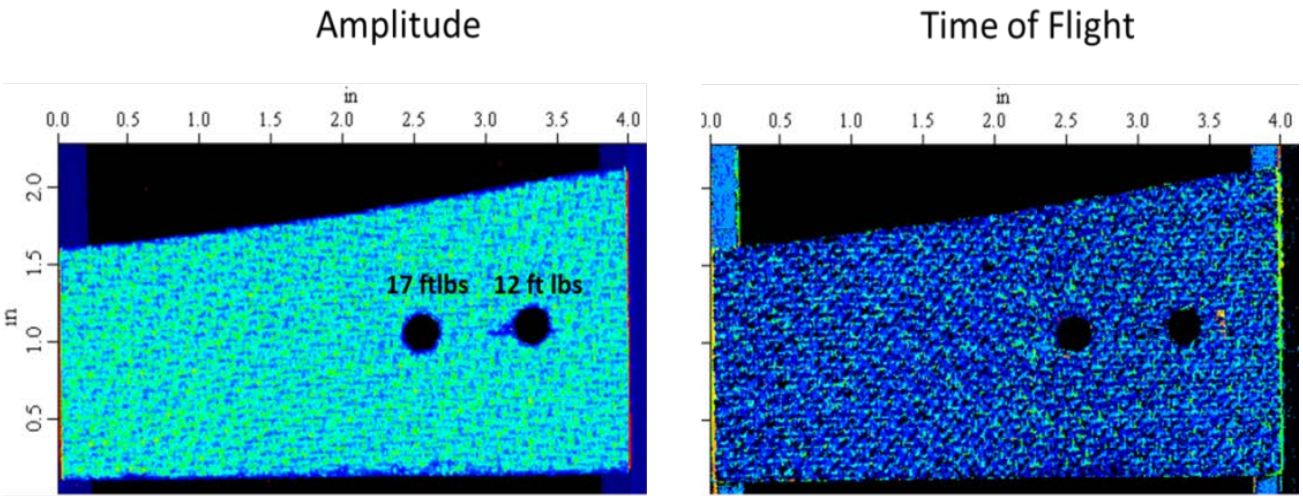

Figure 72. Ultrasonic C-scan amplitude and TOF images of non-epoxy-coated composite with two over-torqued holes

Finally, C-scan amplitude and TOF analyses were performed on test specimen FHF-5 after completion of the filled-hole tension-tension fatigue test shown in table 12 and figure 66. The over-torqued bolt (17 ft lb) was removed from the broken test specimen prior to analysis. The C-scan amplitude and TOF images of the failed test specimen indicated that neither the over-torqued bolt nor the tension-tension fatigue test produced any internal damage. The C-scans detected only damage in the epoxy coating made by the over-torqued bolt and internal damage where the test specimen broke, as shown in figure 73.

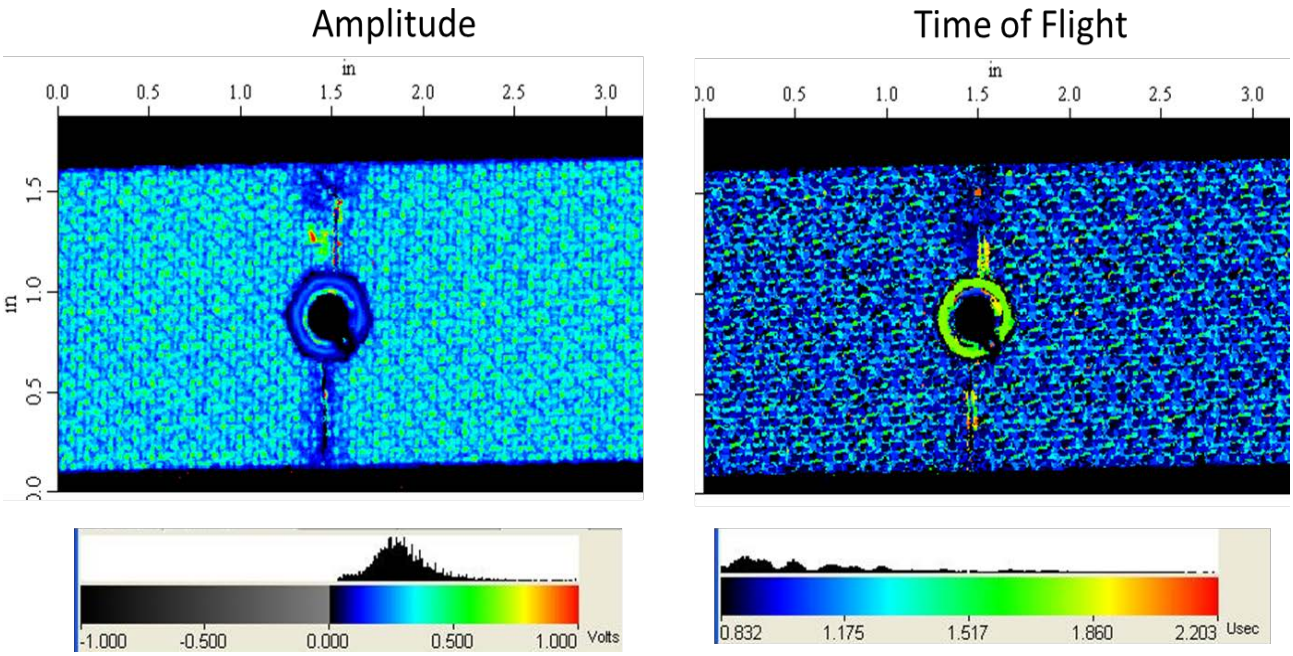

Figure 73. Ultrasonic C-scan amplitude and TOF images of test specimen FHF-5 after failure

6.6 SUMMARY

The research performed in Task 6 shows that the silver epoxy lines have the potential to detect the composite surface deformations caused by fatigue mechanisms. For all the open-hole fatigue tests, the resistances of the silver epoxy lines underwent significant changes (line flaked off, opened under minimum load, etc.) when the applied load reached 80% of the expected failure load (cycles exceeded 200,000). Though none of the open-hole test specimens failed, x-ray CAT scans, magnified cross-sections, and C-scan analyses determined that the test specimens had undergone extensive internal damage at 80% of the failure load, as evidenced by the visible surface delaminations along the edges of the test specimens. It is believed that the surface delaminations were responsible for the permanent (no load) changes in the electrical/physical properties of the silver epoxy lines along the edges of the test specimens. The surface delaminations were best detected when the silver epoxy lines were applied as a 1.6 mm bead (in agreement with the initial test setup results in table 8 or smeared on with a spatula).

In contrast to the open-hole fatigue test, the filled-hole fatigue tests did not create internal/surface delaminations prior to test specimen failure. Over-torqued bolts (up to 17 ft lb, bolt-stripped) did not cause any detectable physical damage to the test specimens (in agreement with NASA reports [6]). Consequently, the silver epoxy lines did not undergo any physical/electrical changes due to over-torqued bolts or prior to the failure of the filled-hole fatigue test specimen.

Initial research indicated that a clear, thin (2.2 mil) polyester tape with an acrylic adhesive (-40°–300° F) could be used in place of the room-temperature curing epoxy layer to isolate the

silver epoxy conductive lines from the conductive composite surface. For the open hole fatigue test specimens, the damage detection capabilities of the silver epoxy lines applied on the tape layer were enhanced in comparison to the lines applied on the epoxy layer. From a maintenance standpoint, the tape improves the ease of use because it does not require curing prior to the application of the silver epoxy lines. The tape insulation forms the basis of a Peel-N-Stick damage sensor (Task 9); specifically, the RFID, connections, and silver conductive line are provided preassembled on a piece of double- or single-sided tape that is peeled from its liner and applied to the composite surface to be monitored for surface cracks due to impacts or fatigue.

Therefore, the research performed in Task 6 indicates that SMART Crack sensors have the potential to be used by maintenance personnel to identify composite components with surfaces changed by internal damage caused by fatigue. When the SMART sensors incorporate a 125 KHz RFID tag, the damage-activated tag can be read directly through the composite skin, allowing the initiation/progression of fatigue damage to be monitored from outside the aircraft.

7. TASK 7: EVALUATION OF SMART SENSORS: BOND FAILURE TESTING

7.1 INTRODUCTION

In addition to the detection of composite damage due to impacts and fatigue, research was also conducted to evaluate the capabilities of the silver epoxy lines to detect surface changes resulting from different bond failure modes. Two different sets of ASTM test specimens were loaded to create interior bond failures/surface changes. The first set of bond failure test specimens were produced and loaded in the manner described in ASTM D5961/D5961M–13, “Standard Test Method for Bearing Response of Polymer Matrix Composite Laminates.” The bolts inserted into the drilled holes were tightened with different levels of torque prior to testing. The second set of bond failure test specimens were produced in the manner described in ASTM D1002 “Standard Test Method for Apparent Shear Strength of Single-Lap-Joint Adhesively Bonded Metal Specimens by Tension Loading.” The test specimens were fatigued using the same fatigue failure test used in Task 6, ASTM D3749 “Standard Test Method for Tension—Tension Fatigue of Polymer Matrix Composite Materials.”

7.2 BEARING FAILURE TEST

To determine if the excessive load/imminent failure prediction capability of the silver epoxy lines could be used to monitor the composite hole enlargement that occurs during ASTM D5961, a set of test specimens were fabricated using a unitape roll of BMS 8-276N Toray Epoxy Prepreg T800SC-24000-10E P235W-19 (Date of Manufacture = 7/16/08). One surface of each test specimen was coated with a room temperature setting, nonconductive epoxy. The cured epoxy coated specimens were drilled (0.25″ hole) and one continuous silver epoxy line (dispensed bead, smoothed bead, or smeared with spatula) was applied to cover the side/end edges and to partially circumvent the drilled hole of each test specimen, as shown in figure 74.

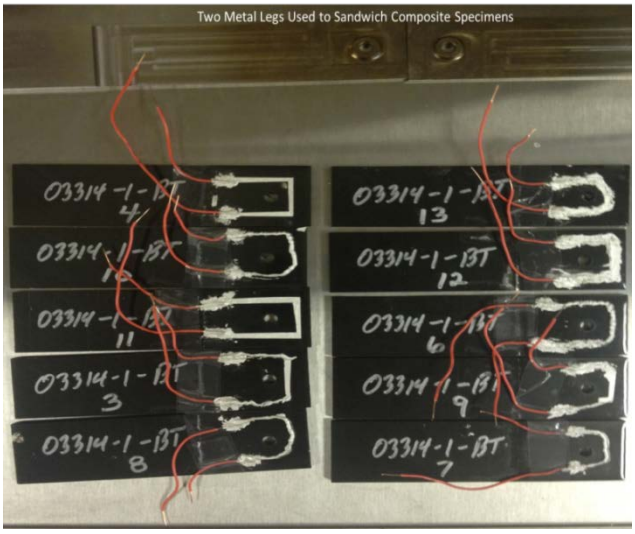

Figure 74. Bearing test metal legs and test specimens with different types of silver epoxy adhesive conductive lines and attached insulated wires

Because the drilled end of each composite specimen was sandwiched then bolted between the ends of the two metal legs shown at the top of figure 74, insulated copper wires were added to the silver epoxy conductive lines so that line resistance measurements could be performed without having to disassemble the bolted sandwich (metal leg/test specimen/metal leg).

To produce representative extended holes, two test specimens (BT-1 and BT-2) were sandwiched/bolted between the two metal legs in figure 74 using 16 in lb of torque (normal tightness) and subjected to the load parameters specified in ASTM D5961. The hole extension (measured in inches) vs. load (measured in lb) plot for specimen BT-1 in figure 75 shows that the hole slowly extends 0.05″ as the load is increased to 6,900 lb then extends rapidly to 0.23″ (hole enlargement) as the applied load is increased (measured load level).

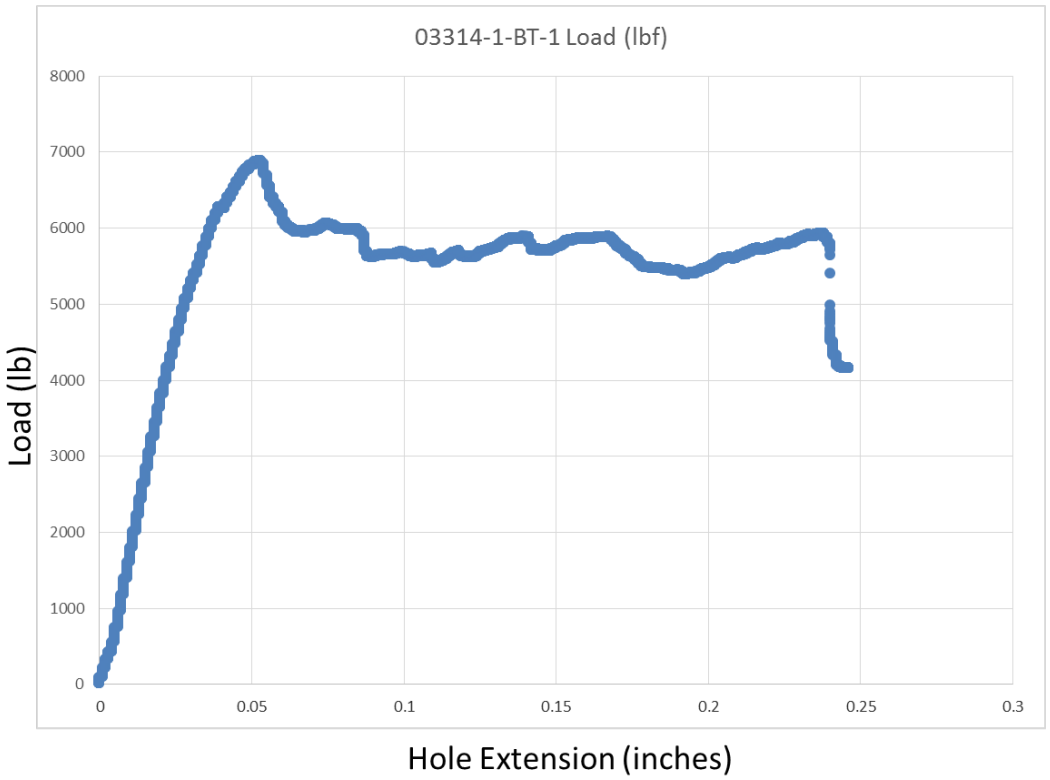

Figure 75. ASTM D5961 bearing test hole extension vs. load plot

The front (epoxy coating/labeled 03314-1-BT 1) surface of BT-1 and the back surface of BT-2 (no coating/writing) surrounding the extended holes of the two failed bearing test specimens are shown in figure 76.

Figure 76. The front (BT-1) and back surfaces of ASTM D5961 test specimens

As shown in figure 76, the ~0.25″ hole extension deforms the epoxy coating on the front side while causing extensive surface damage/delamination on the back side of the test specimens. Based on the test data/results in figures 75 and 76, three bearing test specimens were assembled then loaded using ASTM D5961. To produce realistic hole deformations for evaluating the hole enlargement detection capabilities of silver epoxy lines, test specimen failure was defined as a hole extension of 0.1″.

The front sides of the failed test specimens with the dispensed bead (BT-8), smoothed bead (BT-11), and smeared (BT-13) silver epoxy lines on the epoxy coatings are shown in figure 77.

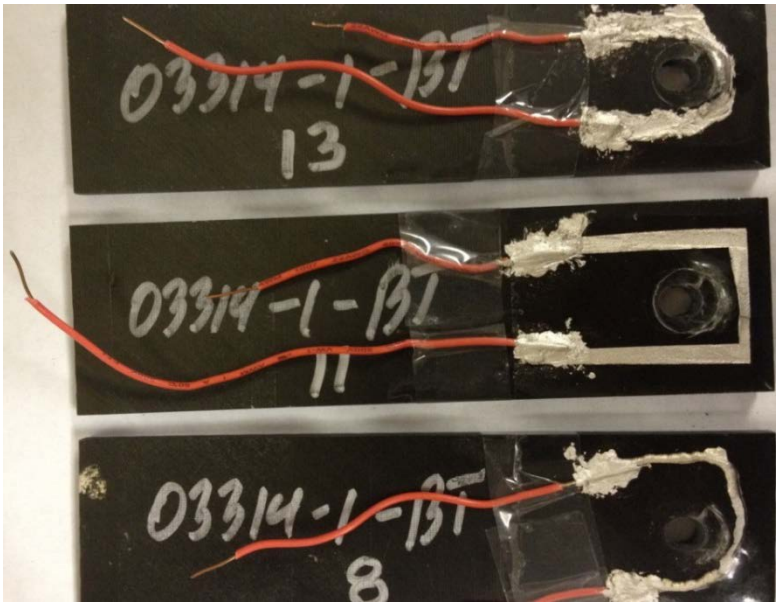

Figure 77. The front surfaces of ASTM D5961 failed test specimens with different types of silver epoxy lines

Though the different epoxy coatings/silver epoxy lines are deformed by the hole extensions in figure 77, the resistances of the lines measured during and after the bearing tests remained below 10Ω. The minimum changes in the measured resistances indicated that the conductive silver epoxy lines separated from the composite surface by a nonconductive epoxy layer were not capable of detecting the hole elongations.

Because the surface delaminations on the back sides of the test specimens were not hindered by the epoxy coating, as is the case in figure 77, a piece of 3M 853 tape was applied to the back side of one test specimen and a straight silver epoxy line was applied to the tape surface. As seen in the lower right-hand corner of figure 78, the conductive line flaked off the tape during the hole elongation/surface delaminations.

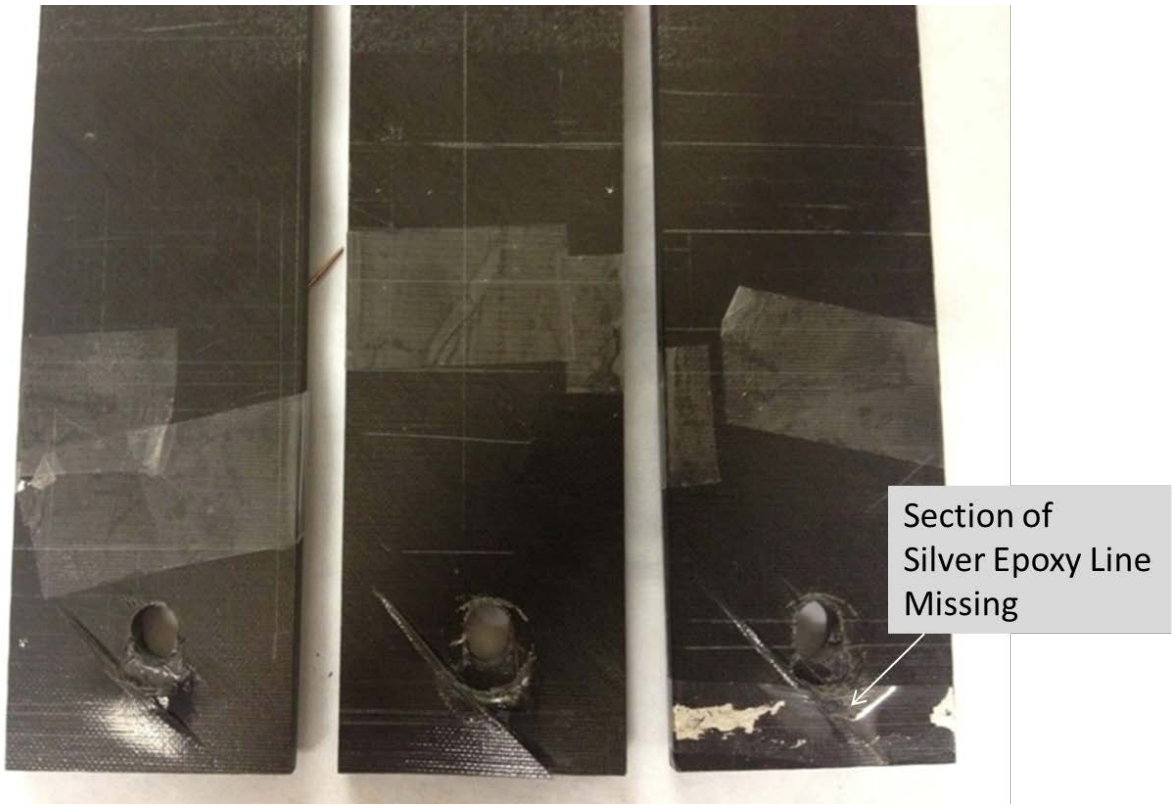

Figure 78. The back surfaces of ASTM D5961 failed test specimens

7.3 LAP SHEAR BOND TEST

In addition to the bearing test specimens, a second set of test specimens was produced, as described in ASTM D1002, "Standard Test Method for Apparent Shear Strength of Single-Lap-Joint Adhesively Bonded Metal Specimens by Tension Loading." The lap shear test specimens were fabricated using a unitape roll of BMS 8-276N Toray Epoxy Prepreg T800SC-24000-10E P235W-19 (Date of Manufacture, 7/16/08). Because the front surfaces of the lap shear specimens overlapped, producing a step between the two surfaces, the even edges of the lap shears were used for bond failure detection. One continuous edge of the lap shear specimen was coated with a room-temperature setting, nonconductive epoxy, and the opposite edge was covered with 3M 853 tape. Different silver conductive lines were then applied to the epoxy (see figure 79) and tape-coated edges.

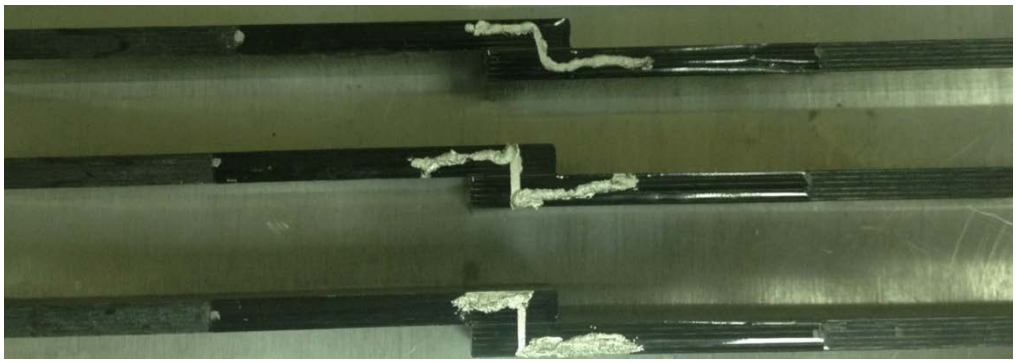

Figure 79. Lap shear test specimens with different types of silver epoxy adhesive conductive lines on epoxy-coated edges

The ASTM D1002 failure load of a prepared lap shear was 2300 lb.

The test specimens in figure 79 were fatigued using ASTM D3749 “Standard Test Method for Tension—Tension Fatigue of Polymer Matrix Composite Materials” (the same one used in Task 6). Load cycles of 1400 lb and 140 lb (60% and 6%, respectively, of expected failure load) were used to initialize the tension-tension fatigue tests. After 25,000–40,000 cycles, the tension-tension loads were increased to 70% (1600 lb and 160 lb). For each lap shear tested, the test specimen broke within 2000 cycles at 70%. The minimum/maximum loads, specimen displacement (ΔS) at the maximum load, and measured resistance (no load and minimal load) for each set of cycles are listed in table 13 for a representative tension-tension fatigue failure test of the lap shears.

Table 13. Representative tension-tension fatigue test data for lap shear test specimen

Load (lbs)			ΔS		Resistance in ohms	
Minimum	Maximum	Date	Inches	Cycles	No Load	Minimum Load
140	1,400	15-Sep-14	0.031	5,000	1	1
			0.0305	10,000	1.1	1.2
			0.0315	15,000	1.4	1.5
			0.0295	20,000	0.9	1.4
		18-Sep-14	0.0315	25,000	0.9	1.1
		27-Sep-14	0.035	30,000	0.7	0.8
160	1,600			35,000	Broke	
			31,790 cycles broke			

In each case, the lap shear failure occurred in the adhesive bond. A representative adhesive bond failure is shown in figure 80.

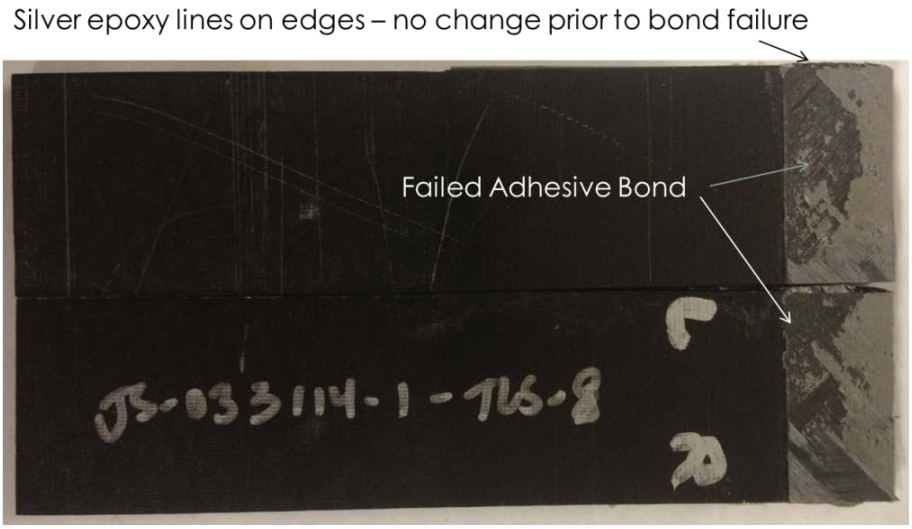

Figure 80. Representative ASTM D3749 fatigue test lap shear failure

Regardless of the silver epoxy line type (bead, smoothed, or smeared), insulating surface (epoxy or tape) or amount of load during the resistance measurement, the fatigued lap shears broke prior to any line resistance increases (i.e., the lines and, consequently, the SMART sensor would not have predictive capability for adhesive bond failure).

7.4 SUMMARY

The research performed in Task 7 showed that the silver epoxy lines have the potential for detecting the surface delamination damage caused by the hole extension of a composite panel bolted to a metal panel. The capability of the silver conductive line to detect the hole extension is greatly improved by using a thin (2 mil) polyester, acrylic adhesive tape to isolate the line from the conductive composite surface instead of a room-temperature curing epoxy coating.

In contrast to the bolted bonds, the silver epoxy lines had minimal to no detection capability for the adhesive bond failure of the lap shear test specimens. Because the epoxy lines on the edges of the lap shears were expected to be extremely sensitive to lap shear movement, the results suggest that the lap shears failed in one complete action rather than the result of long-term degradation.

Therefore, the research performed in Task 7 indicates that SMART Crack sensors could be used by maintenance personnel to identify composite structures with interior surface damage caused by bolted-hole extension but not to detect imminent adhesive bond failure. When the SMART sensors incorporated a 125 KHz RFID tag, the damage-activated tag could be read directly through the composite skin (the lines circumventing the bolted hole extended so that the tag on the composite surface isolated from the metal panel), allowing bolted hole elongation/resulting surface damage detection to occur from outside the aircraft.

8. TASK 8: DEVELOPMENT OF SMART CHEMICAL SENSORS

8.1 INTRODUCTION

To enable a SMART sensor to detect different chemicals inside the aircraft environment, different conductive materials can be used to electrically bypass the IC of an RFID tag. The type of conductive material used in the bypass is selected based on the chemical to be detected. Metallic IC bypasses could be used to detect the presence of corrosive compounds, such as hydrofluoric acid gases from fluorinated insulations/sealants, cleaning liquids, and runway deicer; metal-filled polymers that swell or dissolve in organic fluids could be used to detect the presence of, for example, leaking fuels, lubricants, and hydraulic fluids. To evaluate the chemical sensing potential of SMART sensors, a variety of conductive films and wires were incorporated into the electrical IC bypasses of different types of RFID tags

8.2 MODIFIED HIGH-FREQUENCY RFID TAGS

To evaluate the HF SMART sensors developed on a previous FAA grant [1] for the detection of corrosive liquids, the polycarbonate substrate of the modified HF (13.56 MHz) tags were adhered to the exposed adhesive side of a double-sided acrylic tape (3M 9500PC) and tin metal films were vapor deposited onto the IC bypasses of two modified RFID tags. Silver epoxy was added to the aluminum IC pads prior to the tin vapor deposition to minimize the contact resistance between the deposited film and printed aluminum metal pads. The produced SMART chemical sensors, with the light brown 9500PC tape liner still attached (removed during the experiment to adhere the SMART sensors to the selected composite surface), are shown in figure 81.

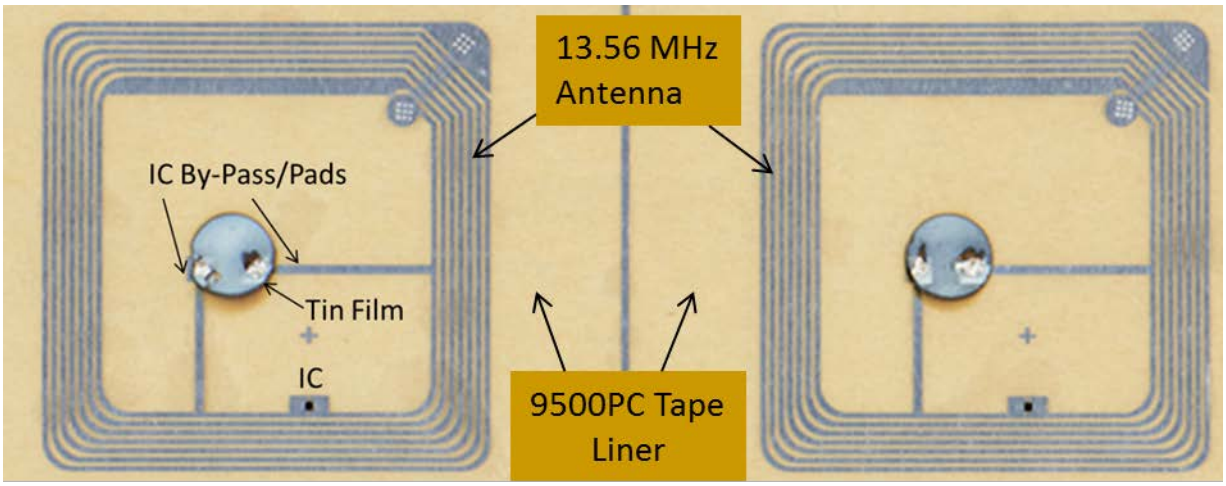

Figure 81. High-frequency RFID tags with vapor deposited tin film

To evaluate the chemical sensitivities of the tin film vapor deposited onto the IC bypass, the tin films of the HF tags were exposed to a corrosive liquid (potassium acetate/chloride solution to simulate runway deicer solution) or gas (vapor above hydrofluoric acid solution). The tin films of the chemically exposed RFID tags were attacked/removed by the corrosive liquid and vapor, exposing the IC bypass pads and nonconductive substrate between the pads, as shown in

figure 82 (i.e., bypass electrically open/IC readable, indicating the presence of a corrosive compound).

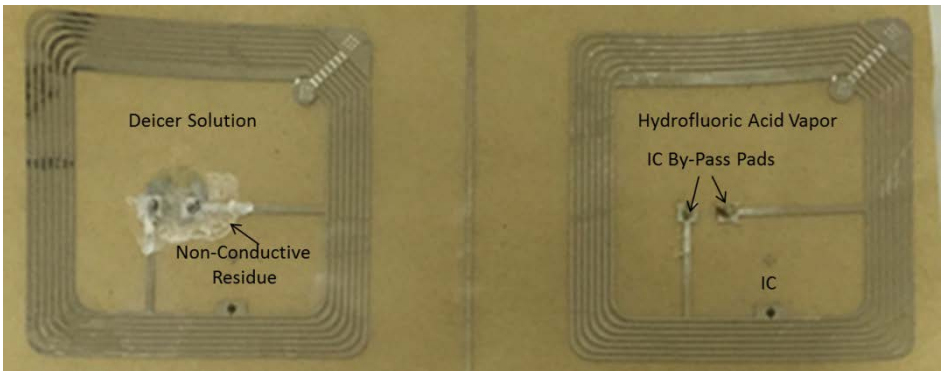

Figure 82. High-frequency RFID tags after exposure to corrosive compounds

In addition to the vapor-deposited HF RFID tags, bare tin wires (diameter = 0.25 mm) were silver epoxied to the IC bypass pads and successfully used as a SMART chemical sensor (i.e., unreacted tags could not be read by the proximate reader, but the stored contents of the IC (tag ID, function, etc.) could be read after extended exposure of the HF RFID tag to hydrofluoric gas.

8.3 LF RFID TAGS

Though the modified HF tags were specially designed to be used in SMART sensors during a previous FAA grant [1], it was demonstrated in Task 3 that the HF tags could not be read through aerospace composite test panels. Therefore, commercial LF tags (125 KHz; figure 14) removed from generic ID badges were modified for use in SMART chemical sensors that could be read through the skin of composite aircraft. The electrical bypasses developed/evaluated for the LF tags had two basic designs: metal film vapor deposited directly onto IC and metal wire silver epoxied to the IC. The IC of the LF RFID tag was connected to the antenna by two thin insulated wires. The soldered electrical pads of the IC and antenna wire ends were bare, making them available for electrical connections (bypass), as shown in figure 83.

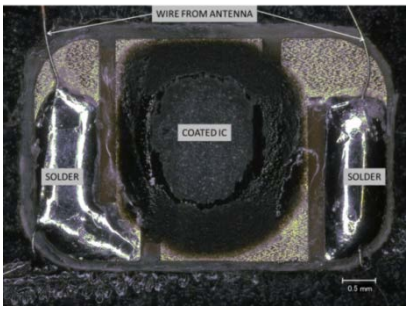

Figure 83. IC and solder points of LF RFID tag

To evaluate the LF SMART sensors for the detection of corrosive compounds, two LF tags were adhered to the exposed adhesive side of double-sided acrylic tape (3M9500PC used to hold the

IC in place, connecting wires, and antenna) and tin metal films were vapor-deposited directly onto the coated IC, solder points, and antenna wire ends (tin film electrically connects two solder points providing IC bypass). The produced SMART chemical sensors with the light brown 9500PC tape liner still attached (removed to adhere the SMART sensors to the selected composite surface) are shown in figure 84.

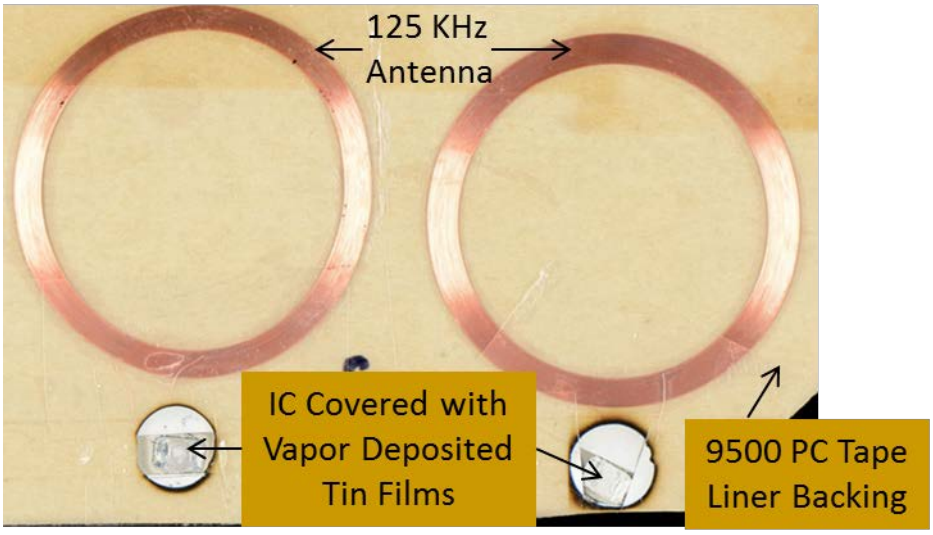

Figure 84. LF RFID tags with vapor deposited tin film

To evaluate the chemical sensitivities of the tin film vapor deposited onto the coated IC/wire ends, the tin films of the LF tags were exposed to a corrosive liquid (potassium acetate/chloride solution to simulate runway deicer solution) or gas (vapor above hydrofluoric acid solution). The tin films of the chemically exposed RFID tags were attacked/removed by the corrosive liquid and vapor, exposing the IC/solder points, as shown in figure 85.

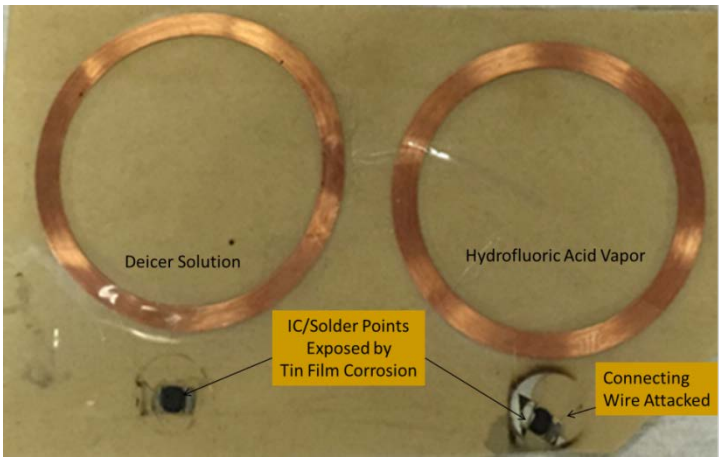

Figure 85. LF RFID tags after exposure to corrosive compounds

Though the tin films in figure 85 were removed by the corrosive liquid and gas, both reacted RFID tags could not be read by a proximate reader. Whether the lack of readability was due to

IC degradation by the tin metal vapor deposition process, chemical attack on the bare wire ends connecting the antenna to the IC, or another issue, these initial tests indicated that the SMART sensor design should isolate the IC/solder points from the potential corrosive environment/reactive portion of the IC bypass.

Consequently, two additional LF SMART chemical sensors were constructed for which the chemical sensing element was removed from the IC and antenna wires. For one chemical sensor, a silver epoxy loop connected to the IC solder points was completed by a tin wire (0.25 mm) to detect corrosive compounds. For the second sensor, a conductive silicone adhesive loop was connected to the IC solder points for detecting leaking organic fluids (line swells, becoming nonconductive to activate tag). In both LF sensors, the double-sided acrylic tape was used to hold in place/support both the RFID tag components and the conductive IC bypass. The LF SMART chemical sensors using the tin wire and the conductive silicone adhesive line performed as expected (i.e., when the tin wire corroded/broke in the presence of a corrosive liquid and the silicone line swelled/became nonconductive in the presence of jet fuel), the information stored in the LF RFID tag IC in figure 86 became readable by a proximate reader.

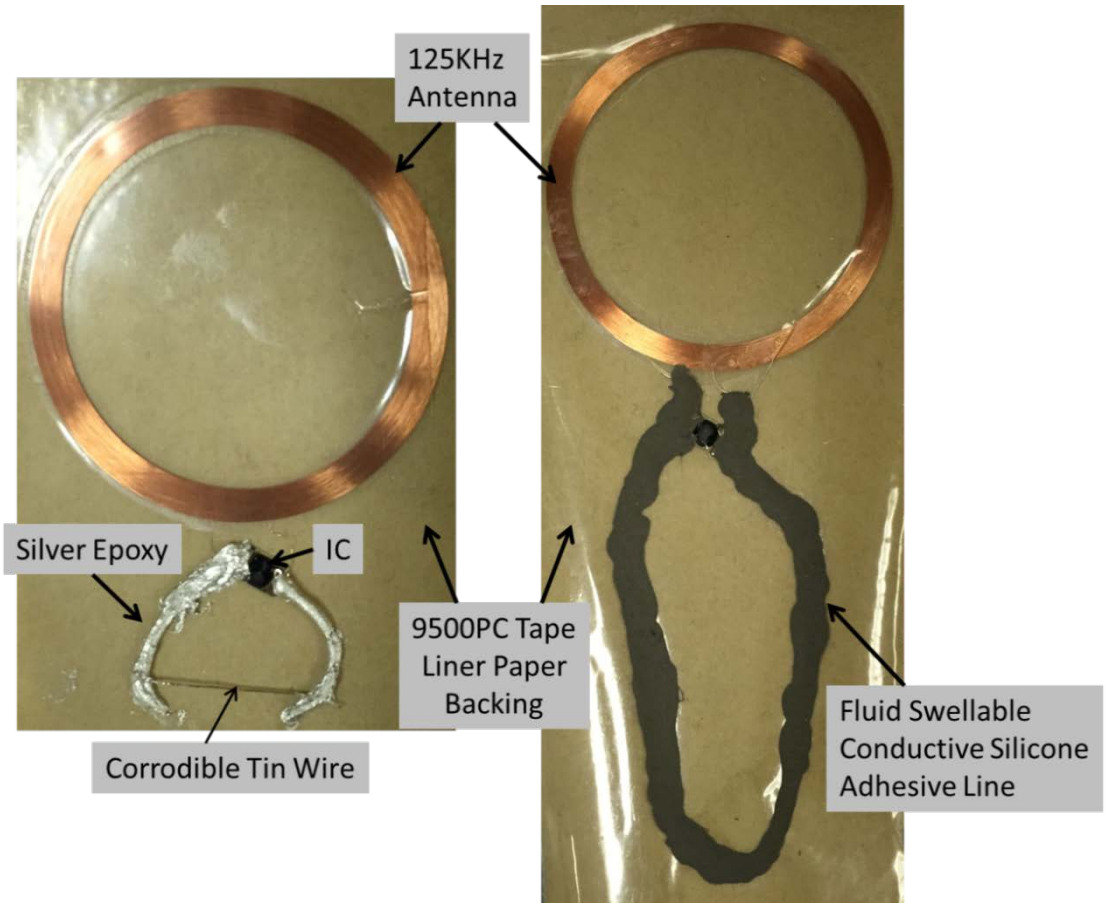

Figure 86. Smart corrosion and organic fluid-sensing chemical sensors

8.4 SUMMARY

The research performed in Task 8 showed that SMART chemical sensors incorporating different conductive materials in the IC bypass can be used to detect the presence of corrosive liquids/gases and organic fluids of interest. The HF and LF SMART sensors used vapor-deposited metal films and bare metallic wires, respectively, in the IC bypass to detect corrosive liquids and gases. The research showed that the LF tags required the corrosion-sensing element (metallic wire) to be removed from the IC for the SMART sensor to perform properly (i.e., activate when the IC bypass separated and/or became nonconductive). Both the HF and LF SMART chemical sensors used conductive silicone adhesive lines to detect the presence of leaking organic fluids. The HF SMART sensor used the polycarbonate substrate of the printed RFID tag to support the conductive IC bypass, and the LF SMART sensor used double-sided acrylic tape to support the IC, antenna, antenna wires, and IC bypass. The HF and LF SMART sensors used double-sided, nonconductive acrylic tape to eliminate the need for the insulating epoxy layer and to adhere the sensors to the selected conductive composite surface.

Therefore, the research performed in Task 8 indicates that different SMART chemical sensors could be used by maintenance personnel to identify the presence of corrosive liquids/vapors and leaking organic fluids. When the SMART sensors incorporate a 125 KHz RFID tag, the tags activated by corrosive liquids/vapors and leaking organic fluids can be read directly through the composite skin, allowing detection to occur from outside the aircraft.

9. TASK 9: DEVELOPMENT OF PEEL-N-STICK SENSORS

9.1 INTRODUCTION

Compared to the epoxy coatings used to insulate the silver epoxy lines of the SMART sensors from the conductive composite surfaces in Tasks 4–7, Peel-N-Stick SMART sensors based on acrylic tape insulating layers would greatly improve the ease of use and shorten the application time of the sensors. Additionally, the results in Tasks 6 and 7 showed that the silver epoxy lines applied to acrylic tapes were more sensitive to fatigue and bolted-hole enlargement than the lines applied to epoxy insulating coatings. Therefore, Peel-N-Stick SMART sensors comprised of LF (125 KHz) RFID tags (read through composite panels) and silver epoxy conductive lines, both adhered to double-sided acrylic tape (3M 9500PC: 5.6 mil), were developed and evaluated as impact sensors. The Peel-N-Stick SMART sensors were developed in two different formats: complete sensor for application to flat surfaces and RFID tag adhered to acrylic tape (silver epoxy lines applied onsite) for curved/connecting surfaces and flat surfaces. To protect the antenna from the potential environment, one-sided acrylic tape (3M 853: 2.2 mil) was applied over the antenna and a portion of the connecting wires. Conductive silicone adhesive was applied to the remaining exposed thin wires to further protect the wires and to ensure the stability and electrical continuity of the wires/IC connections. The complete Peel-N-Stick sensor, with liner and after application to a flat composite test specimen (liner peeled off at angle to keep epoxy trace and IC connection flat), is shown in figure 87.

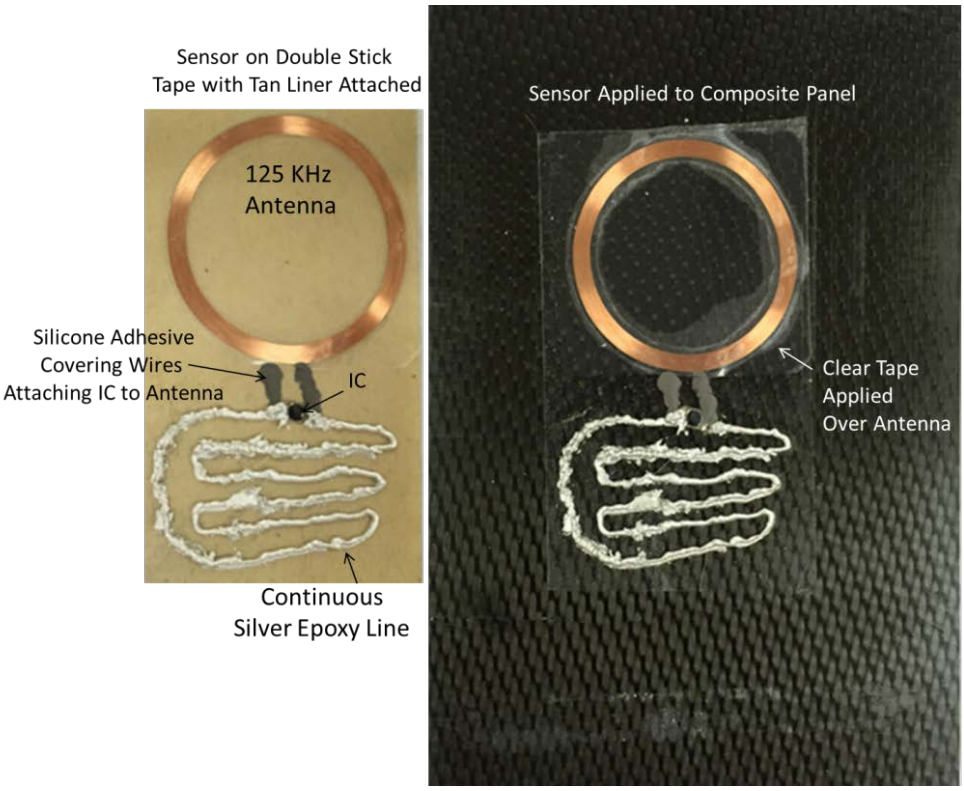

Figure 87. Complete Peel-N-Stick SMART sensor

In contrast to the complete sensor in figure 94, the SMART sensor for curved/connecting surfaces was designed as an RFID tag adhered to double-stick tape (without the silver epoxy lines). The RFID/tape combination is applied to the composite surface so that the RFID tag is adhered to a fairly even surface and the accompanying tape surface is then smoothed/adhered over the curved/connecting surfaces of interest. Once the tape makes continuous contact with the composite surface(s), the silver epoxy lines are applied using a hand-held caulking gun with a tip attached, similar to that shown in figure 88.

Figure 88. Handheld caulking gun containing silver epoxy

An RFID tag/tape combination was applied to a test specimen containing a stringer tapered region (flange) bonded to the skin. The combination was applied so that the RFID tag and IC connections were adhered to the flat surface of the stringer flange, and the accompanying tape portion was smoothed (i.e., allowing no air bubbles to be present, ensuring intimate contact) onto the uneven flange/skin bond. The handheld caulking gun in figure 88 was then used to run a silver epoxy bead (1.6 mm cross-section) from one solder point of the IC across the flange/two uneven bond lines/skin surfaces and then to the other solder point of the IC side completing the IC bypass, as shown in figure 89.

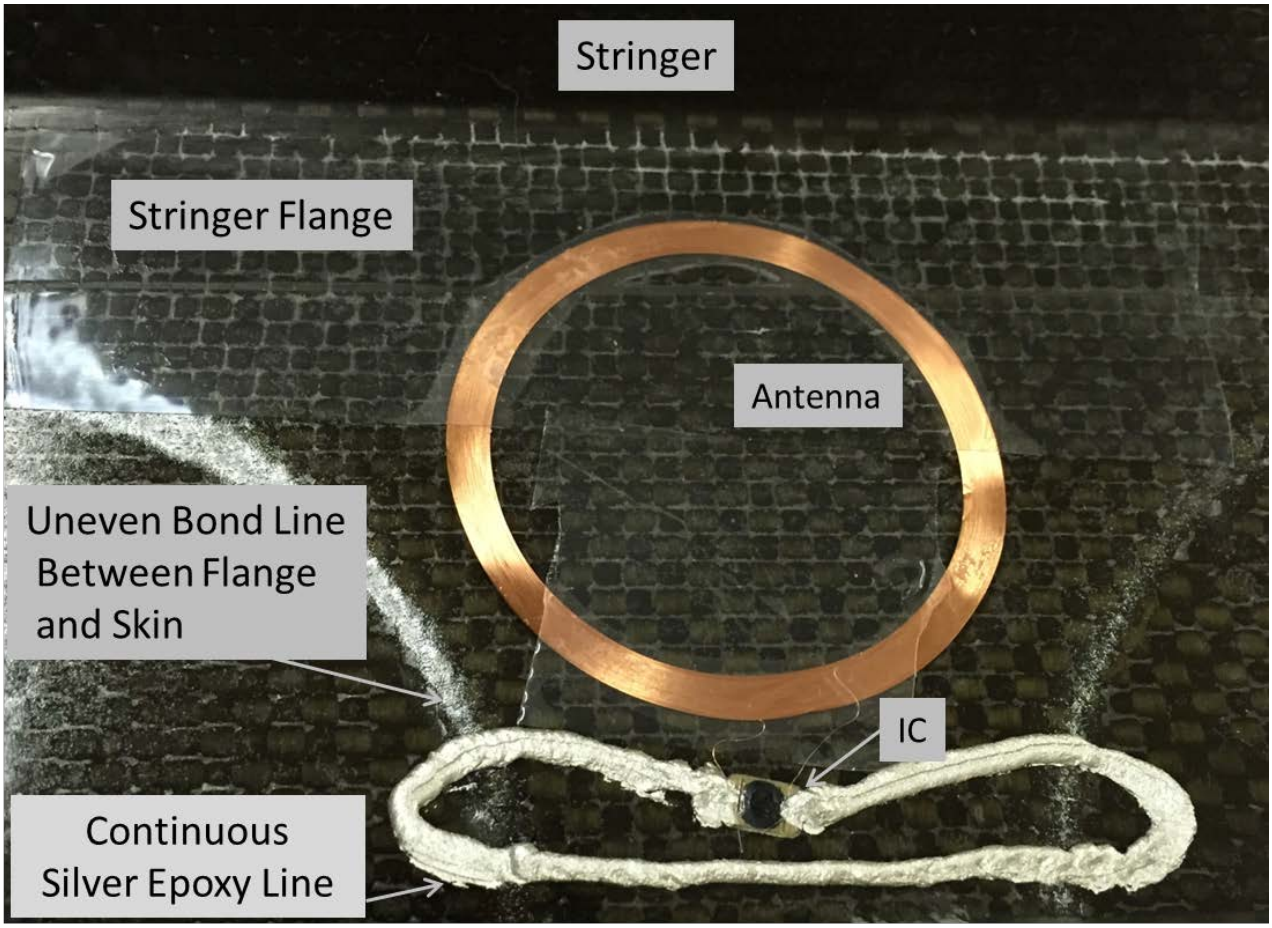

Figure 89. Peel-N-Stick smart sensor smoothed onto composite test specimen with uneven stringer flange/skin bond

Because the silver epoxy is highly conductive prior to curing, the silver epoxy line continuity/IC connection can be confirmed as the line is applied by monitoring the readability of the RFID tag (i.e., the RFID tag will become unreadable when the silver epoxy line/IC connections are complete). After the silver epoxy has fully cured, the readability of the RFID tag can then be checked again to ensure the hardened line/IC connections are still continuous. If the RFID tag becomes readable at any point during the silver epoxy curing process, the caulking gun can be used to apply additional silver epoxy to any gaps to complete the silver line/IC circuit, making the RFID tag unreadable again.

9.2 ASTM D7136 IMPACT TESTING OF PEEL-N-STICK SMART SENSORS

Though the fatigue and bonding tests in Tasks 6 and 7 demonstrated that the silver epoxy lines on acrylic tapes detected surface cracks and deformations resulting from fatigue and hole enlargement equal to/better than silver lines on epoxy coatings, the capabilities of the silver epoxy lines on acrylic tapes for detecting surface cracks resulting from impacts had not been evaluated. Therefore, Peel-N-Stick SMART sensors were adhered to 4″ x 6″ test specimens cut from rigid composite panels (0.15″ thick), produced from eight plies of AGP370-5HS with 8552 epoxy resin. The composite panels were impacted using ASTM D7136 "Standard Test Method for Measuring the Damage Resistance of a Fiber Reinforced Polymer Matrix Composite to a Drop-Weight Event" (setup in figure 38). The ASTM D7136 impacts were performed with a 5.6 lb projectile with a 1.75″ flat end dropped from 27″ to produce significant internal damage without causing visible damage to the impacted surface. The resulting impact summary sheet with the recorded and calculated test data is shown in table 14.

Table 14. ASTM D7136 test data summary for 27″ drop-height impacts

Specimen I.D.	Avg. Width (in.)	Avg. Length (in.)	Avg. Thick. (in.)	Drop Mass (lbs.)	Drop Height (in.)	Potential Impact Energy (in. *lbf)	Impact Velocity (in./sec.)	Max Load Recorded (lbf)	Measured Impact Energy (J)	Measured Impact Energy (in. *lbf)
BK331-5-1	4.000	6.000	0.1240	5.6	27	151.2	137.2	1716	15.47	136.9
BK331-5-3	4.000	6.000	0.1235	5.6	27	151.2	137.9	1808	15.62	138.2
BK331-5-5	4.000	6.000	0.1243	5.6	27	151.2	138.2	1735	15.68	138.8
BK331-5-6	4.000	6.000	0.1240	5.6	27	151.2	138.7	1730	15.81	139.9
BK331-Practice-1	4.000	6.000	0.1233	5.6	27	151.2	138.2	1584	15.69	138.9
BK331-Practice-2	4.000	6.000	0.1237	5.6	27	151.2	138.6	1632	15.78	139.7
Average:							138.1	1701	15.68	138.7
Standard Dev.							0.54	80.15	0.12	1.08
C.o.V.%							.039%	4.71%	0.78%	0.78%

After each ASTM D7136 test was completed, the impacted surface of each test specimen was inspected for damage. Even with the 27″ drop heights (highest heights used in Task 5), the impacted surface of each specimen had less damage than BVD marks (i.e., they could only be seen close up at an angle, similar to marks in figure 39). The initially impacted test specimen (BK331-Practice-1) was tested with numerous silver epoxy lines applied to the polyester substrate of one-sided acrylic tape (3M 853) on the underside surface. The crack produced in the underside surface by the multiple impacts caused an apparent wrinkle in the smoothed tape surface, as shown in figure 90 (the white box on underside surface represents the unsupported area of the test specimen).

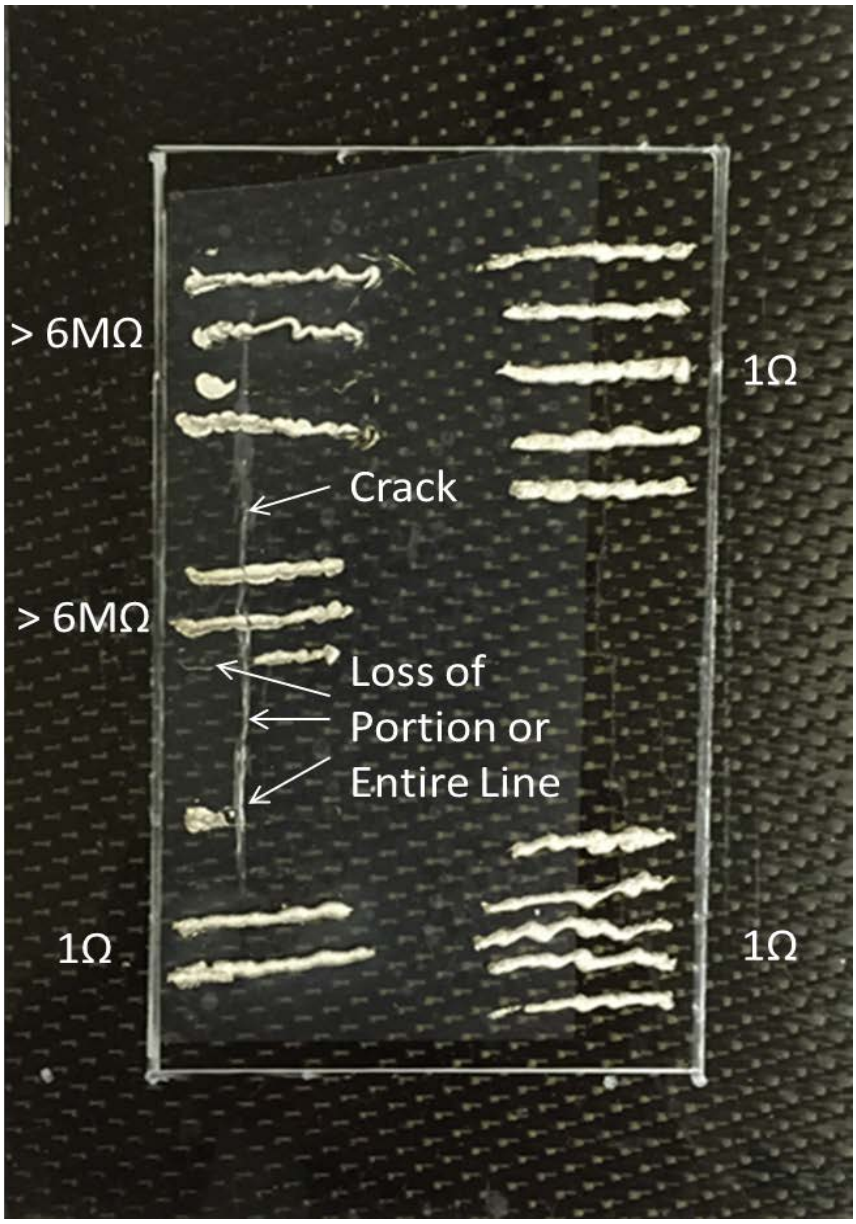

Figure 90. Underside of impacted BK331-practice-1 test specimen

The numerous silver epoxy lines in figure 90 demonstrate that the lines not in contact with the tape wrinkle resulting from the surface crack remained intact (resistance below 1Ω), and the lines that were in direct contact with the wrinkle opened (resistance >6MΩ) or fell off the tape surface.

Test specimens BK331-5-1, BK331-5-3, BK331-5-5, and BK331-5-6, with different Peel-N-Stick SMART sensors, were then single-impacted using the 27″ drop heights, as listed in table 14. For each specimen, the impacted surface had less than BVD marks (i.e., they could only be seen close up at an angle, similar to marks in figure 39) and the RFID tag could be read through the composite test specimen (i.e., the underside crack(s) caused break(s) in the silver

epoxy line attached to the IC). Representative ASTM D7136 impacted test specimens with Peel-N-Stick sensors using double-sided (silver epoxy lines in contact with adhesive) and single-sided (silver epoxy lines on a polyester substrate) tapes are shown in figure 91.

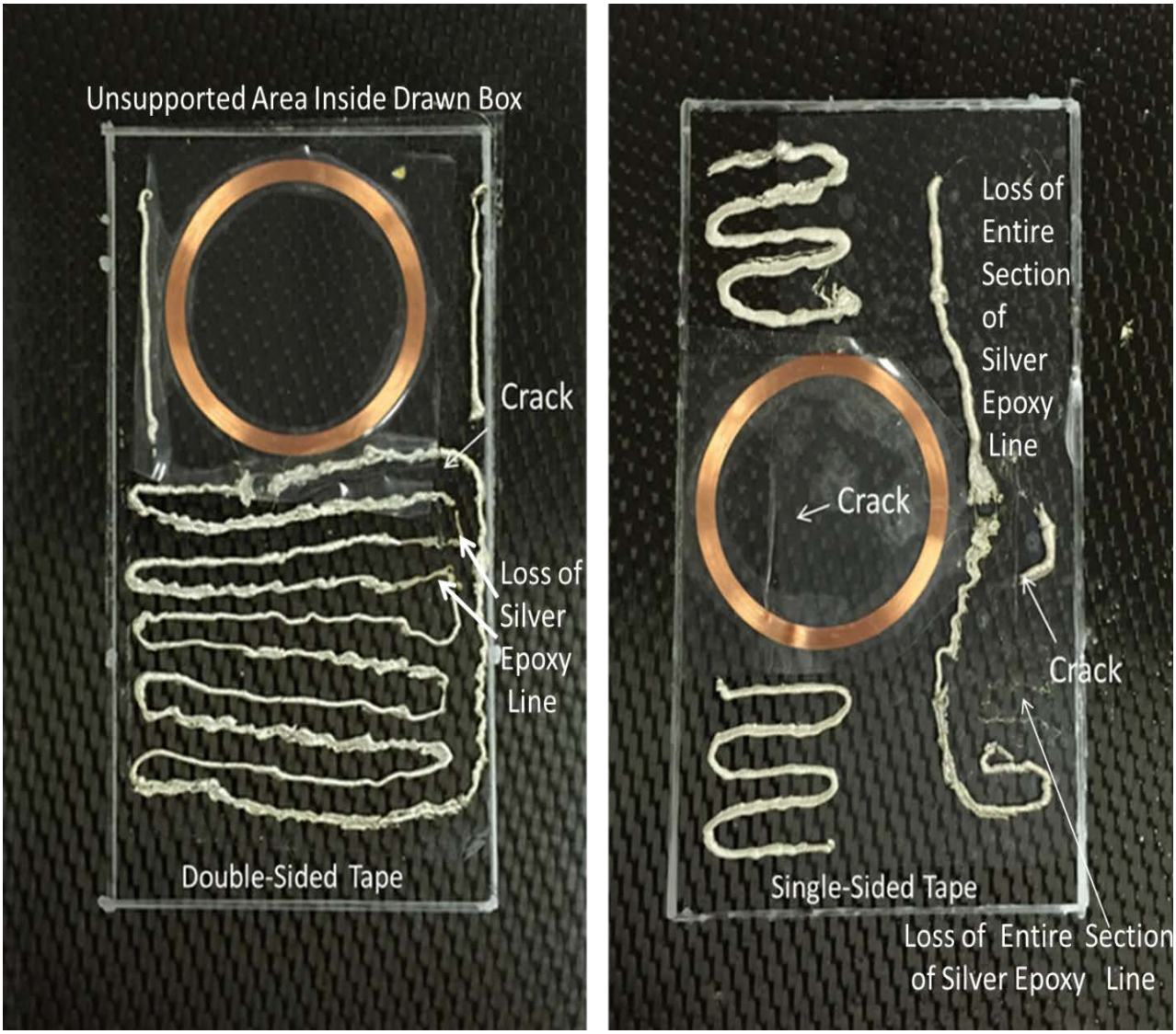

Figure 91. Impacted Peel-N-Stick smart sensors using different acrylic tapes

Like figure 90, the majority of the silver epoxy line on the polyester substrate of the single-sided tape in figure 91 came off in one piece because of the tape wrinkle (surface crack) on the right side of the test specimen. The left tape wrinkle/surface crack under the antenna had no effect on the performance of the RFID tag (readable through composite after impact) or the resistances of the additional silver epoxy lines drawn above and below the antenna.

In contrast to the single-sided tape sensor, only the sections of the silver epoxy lines that came into direct contact with the tape wrinkle/crack were affected for the double-sided tape sensor in figure 91 (i.e., the acrylic adhesive increased the adherence of the silver epoxy line to the tape

surface). Though the amount of silver epoxy lines removed by the tape wrinkles/surface cracks varied depending on the type of tape used, all the Peel-N-Stick SMART sensors detected the underside surface cracks (the RFID tag was activated when the IC bypass silver epoxy lines were broken/removed). Regardless of the tape, the silver epoxy lines away from the surface cracks remained intact after the single ASTM D7136 impacts.

9.3 SUMMARY

Compared to epoxy coatings, the Peel-N-Stick SMART sensor concept based on acrylic tape insulating layers greatly improves the ease of use and shortens the application time of the sensors. The Peel-N-Stick SMART sensors can be applied to composite surfaces as a complete sensor for flat surfaces or as an RFID tag adhered to acrylic tape (silver epoxy lines applied on site) for curved/connecting surfaces.

The research performed in Task 9 showed that the Peel-N-Stick SMART sensors using silver epoxy lines applied to single- and double-sided acrylic tape could be used to detect the presence of underside surface cracks caused by different levels of impact damage. These results also indicated that the impact sensitivity increased or the stability decreased for silver epoxy lines applied on the thin single-sided tape in comparison to those on the thicker double-sided tape. Consequently, the impact sensitivity and stability of the Peel-N-Stick SMART sensors can be tailored based on the application (i.e., the sensitivity increased by reducing the thickness of the tape [follow surface morphology more closely, transmit impact shock wave more efficiently] and stability was reduced by applying the polyester substrate of single-sided tape [the entire cracked silver epoxy line flakes off] compared to the adhesive layer of double-sided tape [which holds the cracked line in place]).

The results in Tasks 6 and 7 indicated that SMART sensors of the Peel-N-Stick type could also be used to detect surface cracks/delaminations resulting from fatigue and bolted-hole enlargement and that the silver epoxy line damage sensitivities are improved by acrylic tape substrates in comparison to epoxy coatings. In addition, Task 8 described SMART chemical sensors adhered by double-sided tape that are Peel-N-Stick by design.

Therefore, the research performed in Tasks 6–9 indicates that activated Peel-N-Stick SMART sensors could be used by maintenance personnel to identify the presence of surface cracks/bond failures resulting from unreported impacts (exterior damage less than BVD), fatigue, enlarged holes, and the presence of corrosive/organic compounds. When the SMART sensors incorporate a 125 KHz RFID tag, the activated tags can be read directly through the composite skin from outside the aircraft.

10. TASK 10: EVALUATION OF SMART CRACK SENSORS FOR HYBRIDS

10.1 INTRODUCTION

To better evaluate the readability and damage-detection capabilities of the Peel-N-Stick SMART sensors for a composite aircraft, a curved aircraft composite test panel (3′ x 2′) with bonded stringers, and an inner layer of metallic mesh for lightning-strike protection were obtained from

Boeing Integrated Defense Systems, Inc. The obtained panel was marked for cutting into impact and fatigue test specimens, as shown in figure 92.

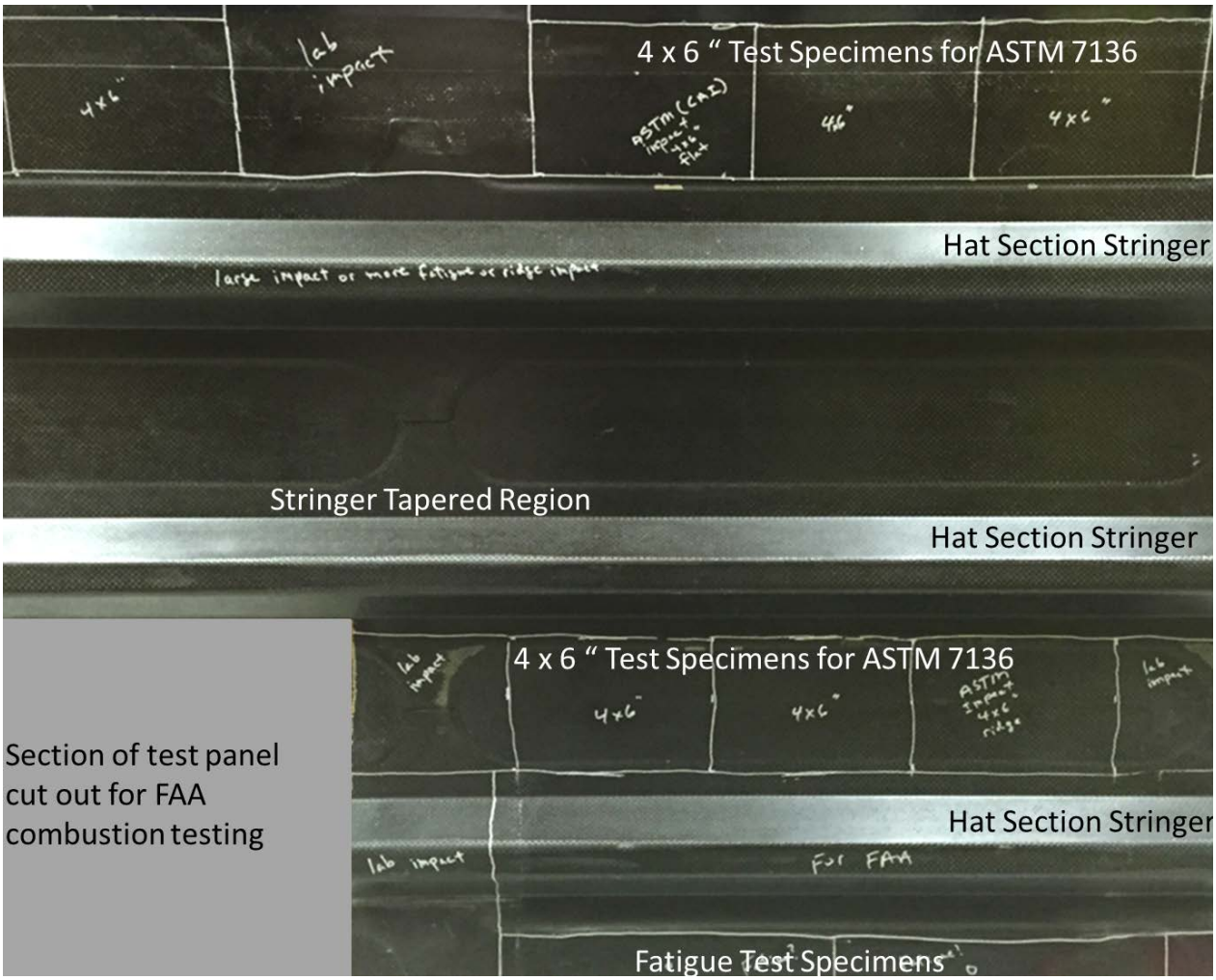

Figure 92. Hybrid composite aircraft test panel containing metallic mesh

Though test specimens were cut from the test panel for ASTM D7136 impact testing, the uneven, curved nature of the produced test specimens eliminated the follow-up CAI ASTM D7137 testing used in Task 5 to assess the effects of the impact damage on the integrity of the test specimen. The curved, uneven nature of the fatigue test specimens also inhibited the planned ASTM D3749 fatigue testing.

10.2 SMART SENSOR READABILITY THROUGH METALLIC MESH

Prior to being cut into the designated smaller test specimens, the test composite panel in figure 92 was first used to evaluate the capabilities of the SMART sensors based on the 125KHz RFID tag to be read through metallic mesh. Though 125 KHz RFID tags were demonstrated to be readable through thick (0.25″–1″) composite materials in previous tasks, the 125 KHz frequency will not penetrate a solid film of metal (metal reflects radio frequency signals). However, the

metal layers incorporated into aircraft composite skins for lightning strikes are present as a mesh providing small air gaps for the 125 KHz signal to penetrate.

To study the potential readability of interior surface SMART sensors from outside the aircraft, 125 KHz RFID tags were adhered to test panel surfaces with the different geometries shown in figure 92 (stringer, tapered region, skin [flat surface cut out for ASTM D7136 specimens] etc.). A small, handheld reader was held within 1″ of the opposite side and scanned across the test panel. The 125 KHz tags adhered to the skin, and tapered regions (flanges) and angled sides of the stringers were all detected by the handheld reader through the metallic mesh of the test panel. The 125 KHz tags adhered to the flat, top surfaces of the stringers were not read (2″ read distance exceeded the capabilities of the handheld reader). These results indicate that physical damage to a silver epoxy line applied to any interior surface would be detected (i.e., the RFID tag becomes readable) from outside a composite aircraft with metallic mesh lightning protection as long as the RFID antenna is positioned on the skin, flange, or side of a stringer.

10.3 LABORATORY IMPACT TESTING OF TEST SPECIMEN WITH METALLIC MESH

To evaluate the effects of multiple impacts on the stabilities of the silver epoxy lines, tape, and RFID antenna/IC connections of a Peel-N-Stick SMART Crack sensor applied to an uneven surface, an RFID tag/tape (double-sided acrylic tape, 3M 9500PC) combination was adhered to a test specimen cut from the test panel (as shown in figure 92) containing a stringer flange bonded to the skin. The RFID tag/tape combination was applied to the test specimen so that the RFID tag and IC connections were adhered to the flat surface of the skin (for readability when activated). The accompanying tape portion was smoothed of air bubbles (to ensure intimate contact) onto the skin, flange, and uneven flange/skin bond, similar to that in figure 89. Because the locations of the impact-produced surface cracks/bond failure were unknown, the handheld caulking gun (as shown in figure 88) was used to run a silver epoxy bead (1.6 mm cross-section) from one solder point of the IC across the skin and flange surfaces and along/across the skin/flange bond to the other solder point of the IC side. Multiple laboratory impacts were then performed with a 10-lb weight dropped from approximately 12″. Because of the uneven nature of the test specimen, and to increase the specimen impact damage, the test specimen was supported only on the ends.

After multiple impacts, the test specimen had undergone significant damage (underside crack extended through to impact surface, etc.) and the Peel-N-Stick SMART Crack sensor could be read through the composite test specimen (RFID antenna/IC connections performed properly after multiple impacts/severe damage). On examination of the underside surfaces, it could be seen that the tape had a wrinkle up to the RFID antenna (i.e., a skin crack). Also, the silver epoxy line had fallen off (exceeding adhesion of double-sided tape) and the tape had ripped along the flange/skin bond (the bond separation was expected [7]), as shown in figure 93.

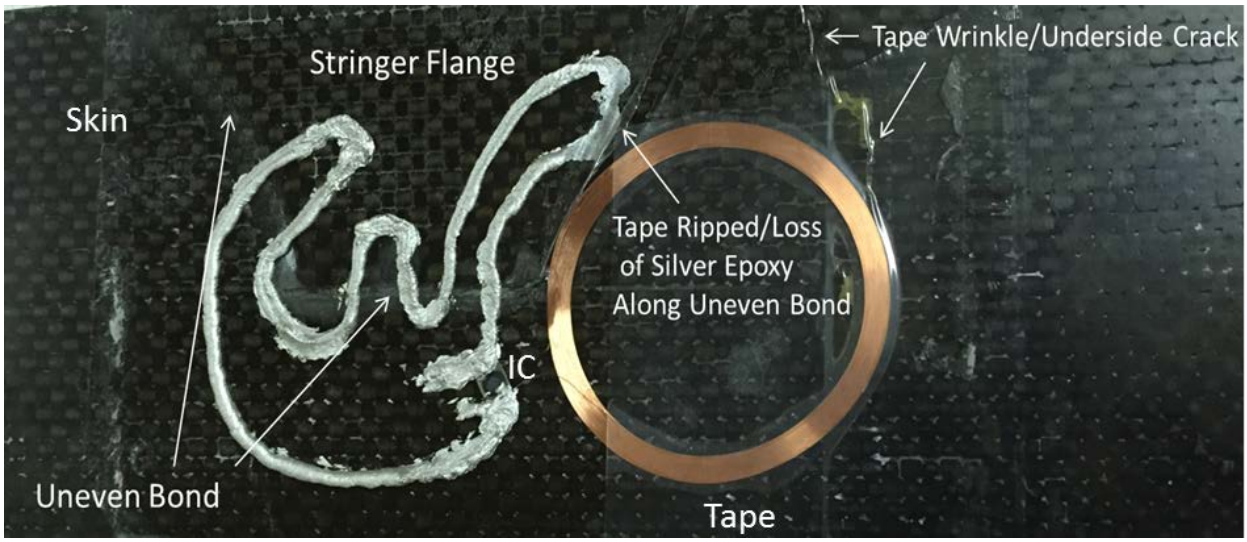

Figure 93. Multiple-impacted test specimen with Peel-N-Stick smart sensor

10.4 C-SCAN ANALYSES OF LAB-IMPACTED TEST SPECIMEN

To confirm the damage detected by the silver epoxy line correlated with the location of the internal damage produced by the multiple impacts, the test specimen in figure 93 was analyzed using ultrasonic C-scan amplitude and TOF techniques (reflector plate signal). The C-scan amplitude and TOF images of the test specimen before (pre-existing voids) and after the multiple impacts are shown in figure 94.

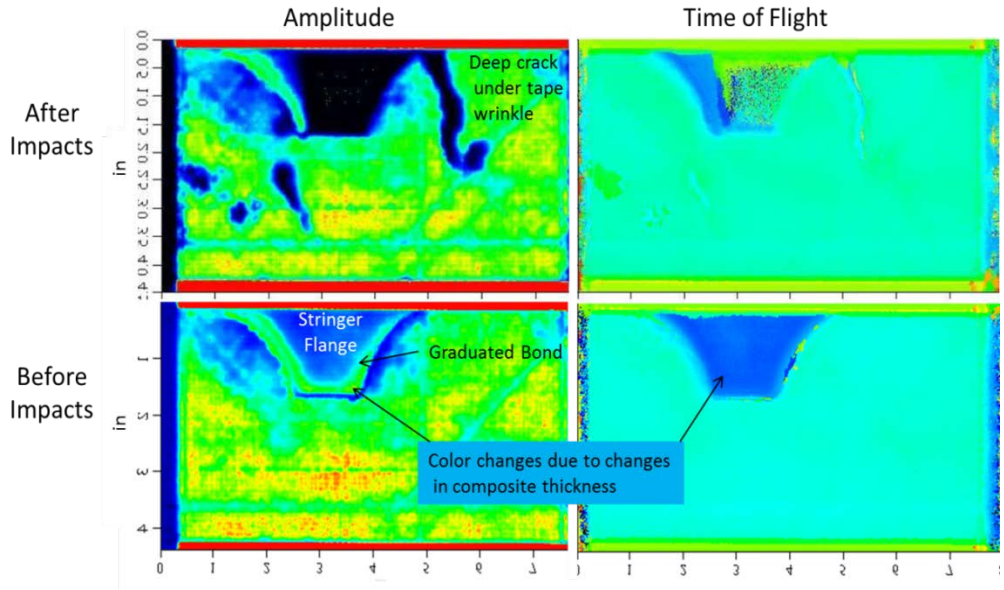

Figure 94. Amplitude and TOF C-scans of test specimen with Peel-N-Stick impact sensor before and after multiple dropped-weight impacts

The C-scan amplitude images (color scale: green [minimal damage], dark blue/black [delamination]) and TOF images (color scale: blue [minimal damage], yellow/red [delamination]) shown in figure 94 (flipped to align images with figure 93) are in full agreement with the breaks in the silver epoxy line/tape tear (i.e., C-scan images show that the side of the stringer flange nearest to the deep crack has delaminated/bond failed). The small, scattered delaminations detected to the left of the stringer flange in the C-scan images of the multiple-impacted test specimen caused wrinkles in the tape but were not below the silver epoxy line.

10.5 ASTM D7136 IMPACT TESTING OF TEST SPECIMENS WITH METALLIC MESH

To study the effects of the metallic mesh on skin impact damage (delamination) and corresponding SMART sensor damage detection capabilities, Peel-N-Stick SMART Crack sensors (3M 9500PC, double-stick tape) were applied to the different 4″ x 6″ specimens cut from the test panel in figure 92. Essentially, flat test panel skin locations were selected for the test specimens in an attempt to match the flat sample holder surfaces of ASTM D7136 “Standard Test Method for Measuring the Damage Resistance of a Fiber Reinforced Polymer Matrix Composite to a Drop-Weight Event” (setup in figure 38). The two basic test specimens obtained from the test panel with the Peel-N-Stick SMART sensors attached are represented in figure 95.

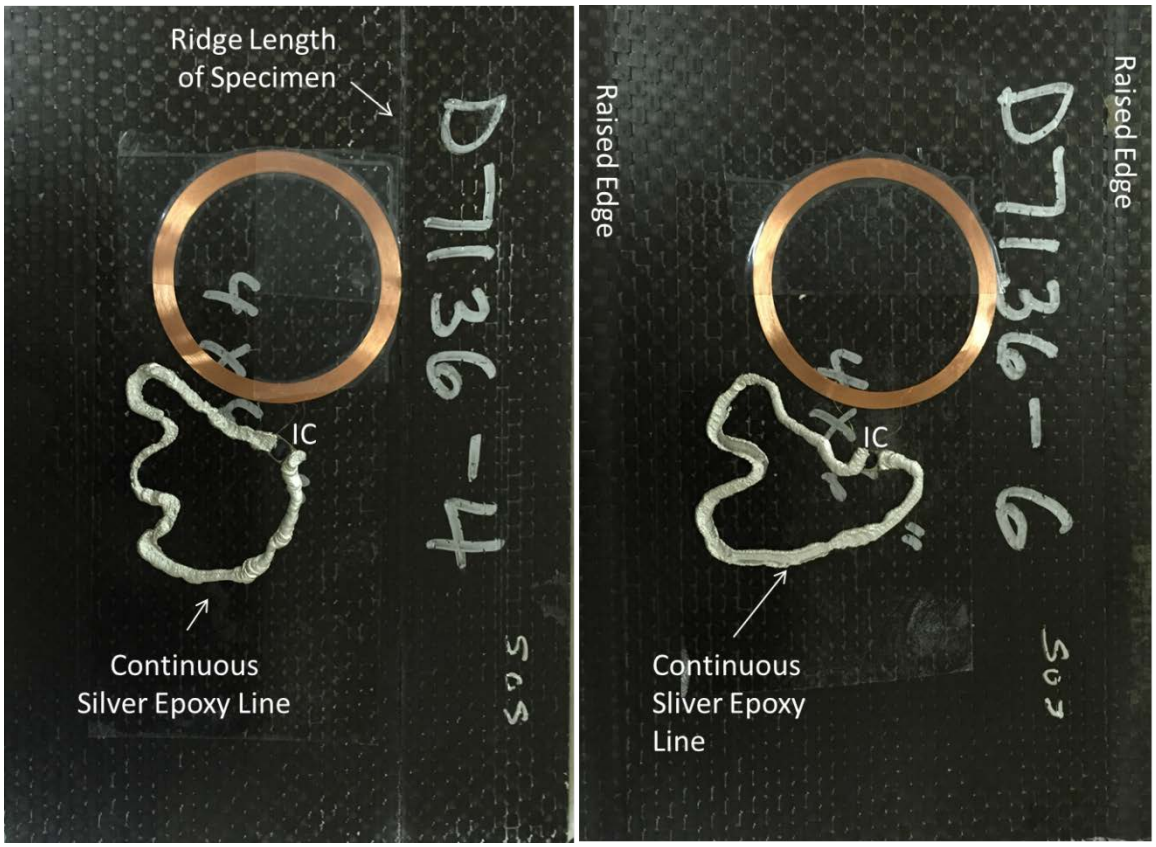

Figure 95. Representative ASTM D7136 test specimens with metallic mesh and Peel-N-Stick smart sensors

The test specimen D7136-4 on the left side in figure 95 had a small ridge running down its length. Test specimens D7136-1–D7136-4, obtained from the top of the test panel in figure 92, all contained the full-length ridge. Test specimen D7136-6 on the right side in figure 95 was essentially flat but had raised edges. Test specimens D7136-5–D7136-7, obtained from the skin between the two stringers in the lower portion of the test panel in figure 92, had raised edges. Because the test specimens were not totally flat, the CAI measurements (ASTM 7137) could not be made on the impacted specimens.

The ASTM D7136 impacts of the specimens with sensors attached were performed with a 5.6-lb projectile (1.75″ flat end) dropped from 24.25″ to produce internal damage, producing less than BVD damage (i.e., damage cannot be seen from more than 5′ in normal lighting) to the impacted surface. The resulting impact summary sheet, with the recorded and calculated test data, is listed in table 15.

Table 15. ASTM D7136 test data summary for 24.25″ drop-height impacts

Specimen I.D.	Avg. Width (in.)	Avg. Length (in.)	Avg. Thick. (in.)	Drop Mass (lbs.)	Drop Height (in.)	Potential Impact Energy (in. *lbf)	Impact Velocity (in./sec.)	Max Load Recorded (lbf)	Measured Impact Energy (J)	Measured Impact Energy (in. *lbf)
D7136-1	4.000	6.000	0.0775	5.6	24.25	135.8	127.9	1505	13.43	118.9
D7136-2	4.000	6.000	0.0800	5.6	24.25	135.8	128.1	1510	13.47	119.2
D7136-3	4.000	6.000	0.0800	5.6	24.25	135.8	128.0	1515	13.46	119.1
D7136-4	4.000	6.000	0.0795	5.6	24.25	135.8	126.9	1505	13.23	117.1
D7136-5	4.000	6.000	0.0795	5.6	24.25	135.8	126.6	1520	13.17	116.6
D7136-6	4.000	6.000	0.0800	5.6	24.25	135.8	127.0	1525	13.24	117.2
D7136-7	4.000	6.000	0.0795	5.6	24.25	135.8	127.4	1554	13.32	117.9
Average:							127.4	1519	13.33	118.0
Standard Dev.							0.60	17.03	0.12	1.09
C.o.V.%							0.47%	1.12%	0.92%	0.92%

After the single impacts from 24.25″, every Peel-N-Stick SMART sensor shown in table 15 that was adhered to a test specimen activated and could be read through the composite test specimen (RFID antenna/IC connections performing properly after impact, read through metallic mesh). The activation of the SMART sensors (indicating impact-induced internal damage/underside surface crack(s)) occurred with below BVD damage to the impact surface. The shallow mark in the D7136-4 impacted surface (representative of test specimens D7136-1 through D7136-4) could be seen only close-up under angled lighting, but the impacted surface of D7136-6 (representative of test specimens D7136-5 through D7136-7) had no visible damage, as shown in figure 96.

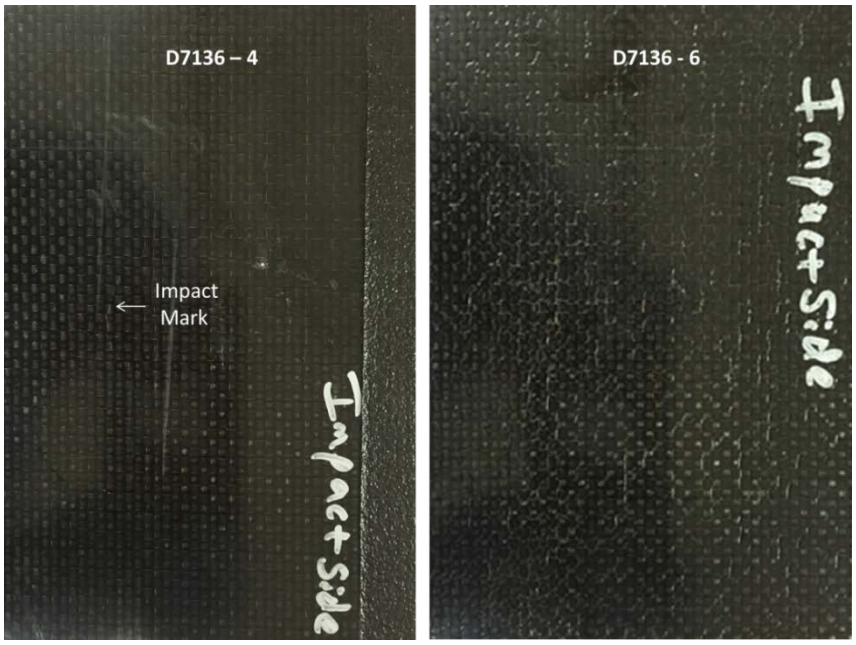

Figure 96. Representative impact surfaces of ASTM D7136 test specimens

On examination of the underside surfaces directly opposite the surface mark (D7136-1–D7136-4) or projectile-impacted area (D7136-5–D7136-7), the tape had a wrinkle or the silver epoxy line had a crack (break in IC bypass activated RFID tag), as shown in figure 97.

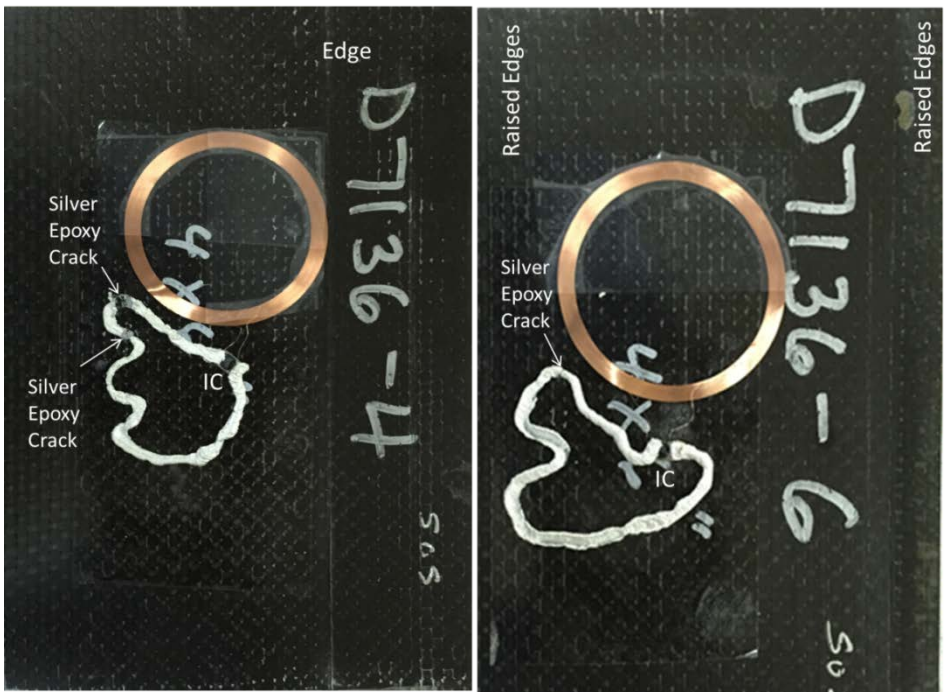

Figure 97. Representative Peel-N-Stick smart sensors on ASTM D7136 test specimens

10.6 C-SCAN ANALYSES OF ASTM 7136-IMPACTED TEST SPECIMENS

To confirm the damage detected by the silver epoxy lines correlated with the internal damage present, test specimens D7136-4 and D7136-6 (silver lines/RFID tag removed) in table 15 were analyzed using ultrasonic C-scan amplitude and TOF techniques (reflector plate signal). The C-scan amplitude and TOF images of the impacted test specimens are shown in figure 98 (images are rotated/aligned in the same direction as the test specimen pictures in figure 97).

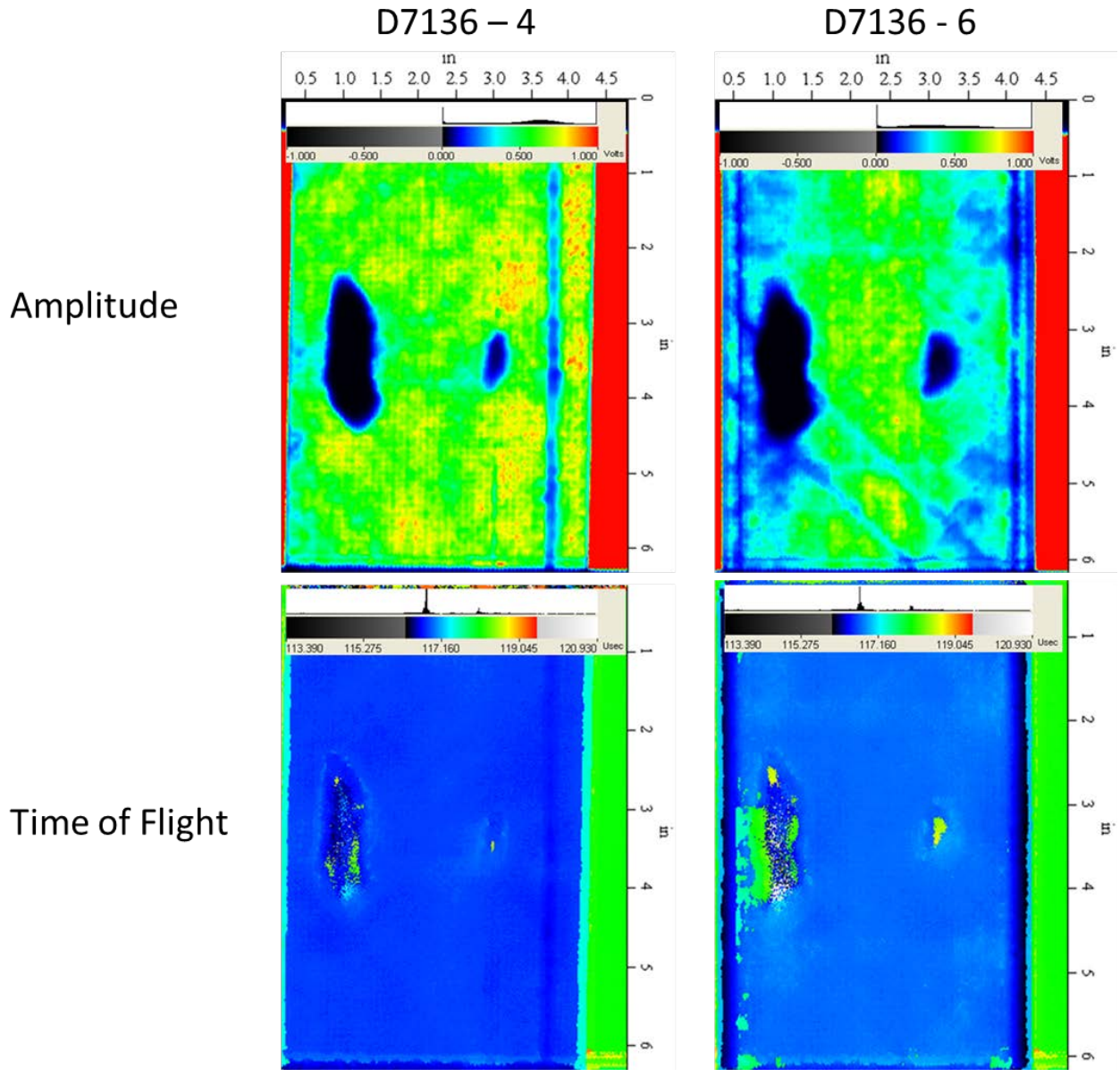

Figure 98. Ultrasonic C-scan amplitude and TOF images of representative test specimens after ASTM D7136 single impacts

The C-scan amplitude images (color scale: green [minimal damage], dark blue/black [delamination]) and TOF images (color scale: blue [minimal damage], yellow/red [delamination]) shown in figure 98 are in full agreement with the breaks in the silver epoxy lines in figure 97 (i.e., the larger delamination detected by the C-scan images for each impacted test specimen coincides with the break in the silver epoxy line). The smaller delaminations detected by the C-scans were outside the areas monitored by the silver epoxy lines. In agreement with the earlier tasks, ASTM D7136 produced internal damage (see figure 98) in the hybrid composite test specimens, resulting in corresponding underside surface cracks (see figure 97) and producing less than BVD damage to the impacted surfaces (see figure 96).

10.7 SUMMARY

The initial results in Task 10 indicate that 125 KHz RFID antenna positioned on the skin, stringer flange, or side of a stringer can be read through a hybrid composite test panel containing a metallic mesh for lightning strikes. The research performed in Task 10 also showed that the Peel-N-Stick SMART sensors using silver epoxy lines applied to double-sided acrylic tape were capable of detecting both stringer flange delamination/bond failure and the presence of skin surface cracks caused by different levels of impact damage. Only the sections of the silver epoxy lines that came into direct contact with the surface damage/deformation were affected for the double-sided tape sensor (i.e., acrylic adhesive ensured the cracked silver epoxy line remained attached to the tape surface). If deemed necessary, the impact sensitivity of the Peel-N-Stick SMART sensors could be increased by using single-side tape (conductive lines applied to polyester substrate) in place of the double-side tape, as shown in Task 9 (see figure 91).

The research performed in Task 10 indicates that activated Peel-N-Stick SMART sensors could be used by maintenance personnel to identify the presence of stringer delaminations/bond failures and skin surface cracks resulting from unreported impacts. These results further indicate that damage to a silver epoxy line applied to any structure can be detected (RFID tag becomes readable) from outside the composite aircraft with lightning protection as long as the RFID antenna is positioned on the skin, stringer flange, or side of a stringer.

11. REFERENCES

1. Kauffman, R., FAA Grant 11-G-011, “Development of Technologies to Improve the Reliability and Intelligence of Aircraft Electrical Wire and Interconnect Systems,” FAA report DOT/FAA/TC-13/20, August 2012.

2. Kauffman, R.E and Wolf, J.D., U.S. Patent No. 8,395,521, “SMART Aerospace Structures,” March 2013.

3. Tandon, G.P. et al., “Enabling Technologies for the Health Management of Composite Structures,” *SAMPE 39th ISTC*, Cincinnati, October 29–November 1, 2007.

4. Rice, B.P., U.S. Patent No. 7,921,727, “Sensing System for Monitoring the Structural Health of Composite Structures,” April 2011.

5. Xie, M., “Intelligent Engine Systems: SMART Case System,” available at http://ntrs.nasa.gov/archive/nasa/casi.ntrs.nasa.gov/20080023404_2008022870.pdf (accessed on 08/31/15).

6. Thomas, F.P., NASA report NASA/TM-2006-214323, “Experimental Observations for Determining the Maximum Torque Values to Apply to Composite Components Mechanically Joined With Fasteners,” Marshall Space Flight Center Director’s Discretionary Fund Final Report, Project No. 03-13, February 2006.

7. Neidigk, S. et al., “A Comparison of Inspection Methods for Assessing Composite Laminate Impact Damage in the Failure Threshold-to-Barely Visible Range,” available at http://www.meetingdata.utcdayton.com/agenda/airworthiness/2014/proceedings/presentations/P7408.pdf (accessed on 08/31/15).